



A Multi-Faceted Statistical Approach for Safety Analysis of Pressurised CO₂ Transmission Pipelines

A thesis submitted to University College London for the degree of Doctor
of Philosophy

by

Jiahuan Yi

Department of Chemical Engineering

University College London

Torrington Place

London WC1E 7JE

December 2023

I, Jiahuan Yi confirm that the work presented in this thesis is my own. Where information has been derived from other sources, I confirm that this has been indicated in the thesis.

List of Publications

1. **Yi, J.**, Mahgerefteh, H. and Porter, R.T.J., 2024. A probabilistic approach to optimal emergency shutdown valve configuration for pressurised CO₂ pipelines. *Journal of Cleaner Production*, 466, p. 142915.
2. **Yi, J.**, Martynov, S. and Mahgerefteh, H., 2023. Puncture failure size probability distribution for CO₂ pipelines. *International Journal of Greenhouse Gas Control*, 125, p.103889.
3. **Yi, J.**, Mahgerefteh, H. and Martynov, S., 2022. Estimating the failure probability of CO₂ pipeline as part of carbon capture and storage chain. *Chemical Engineering Transactions*, 91, pp.115–120.
4. **Yi, J.** and Mahgerefteh, H., 2020, November. An analytically based pressurised pipeline decompression model. In *Proceedings of Hazards 30 Symposium Series*. Institution of Chemical Engineers (IChemE).
5. Yu, J., **Yi, J.** and Mahgerefteh, H., 2022. Optimal emergency shutdown valve configuration for pressurised pipelines. *Process Safety and Environmental Protection*, 159, pp.768–778.

Abstract

Global efforts to reach net zero emissions targets rely heavily on Carbon Capture Utilisation and Storage (CCUS) for decarbonising unabated coal power stations and industrial emissions sources such as refineries, cement and steel making industries. An essential element of the CCUS chain involves the large-scale transportation of the captured CO₂ for permanent geological storage or as a feedstock for utilisation to produce chemicals or fuels. Pressurised pipelines are widely considered as the safest and most economical CO₂ transport option. By 2050, the amount of captured CO₂ is expected to increase significantly reaching ca. 7.6 Gt, requiring a vast network of 200,000 to 550,000 km of CO₂ pipelines. Given that CO₂ is increasingly toxic at concentrations over 7% vol/vol, and the large amounts involved, the failure of CO₂ pipelines poses serious risks of fatalities, environmental damage, and economic losses. As such, ensuring the safe operation of such pipelines is of paramount importance to the public acceptability of CCUS as a viable means for tackling climate change. Central to the above is the reliable quantification of the risks posed by such pipelines in the event of an accidental failure. In essence the above involves three main steps namely, 1) modelling pipeline decompression to predict the outflow characteristics following failure, 2) performing quantitative risk assessment to evaluate the failure consequences, and 3) implementing emergency response planning strategies to mitigate the failure consequences to as low as reasonably practicable.

This thesis presents the development and assessment of rigorous mathematical techniques for conducting such work. These include the development of a computationally efficient pressurised pipeline decompression model, an analytical approach for estimating pipe failure hole size distribution probability and a probabilistic Multi-Objective Optimisation (MOO) technique for optimising inline Emergency Shutdown Valve (ESDV) configuration.

The computationally efficient pressurised pipeline decompression model is developed as a fundamental extension of a previously developed analytically based Vessel Blowdown Model (VBM) for simulating the transient outflow following the accidental failure of high-pressure pipelines. Based on the modification of the standard vessel discharge equations through incorporating additional inflow terms, the extended model addresses the fundamental limitations of VBM in handling un-isolated releases and fluid/wall heat exchanges. The new model is successfully tested against the results obtained using an extensively validated but computationally demanding numerical pipeline decompression model by simulating the failure of a hypothetical pressurised methane pipeline initially at 21 bar and 300 K. The verification tests include various feed flow rates (1 to 7.5 kg/s), pipe lengths (100 to 5,000 m) and puncture to pipe internal diameter ratios (0.2 to 0.8), producing a maximum disagreement of ca. $\pm 7\%$ between the two models' predictions.

The reliability of pipeline failure hole size probability distribution estimation heavily relies upon the availability of sufficiently large pool of historical data. Currently, this is an issue for CO₂ pipelines given their relatively small number in operation. In this part of the thesis, the development of an analytical approach capable of addressing the above issue is presented. The procedure involves fitting statistical probability distributions to the historical failure hole size data using the maximum likelihood estimator, complemented by using bootstrapping method to improve the estimation confidence. The application of the above technique to both pressurised CO₂ and hydrocarbon pipelines indicates that compared to the latter, CO₂ pipelines, with at least 80% of their failures corresponding to punctures smaller than 50 mm, are more likely to experience smaller puncture failures, thus resulting in smaller magnitude but more prolonged releases. This directly impacts the preventive and emergency response planning as well as failure detection techniques required especially in the case of buried CO₂ pipelines where small leaks can remain undetected for long periods.

The final part of this thesis deals with the development and application of a probabilistic MOO technique for selecting the optimal inline ESDV configuration for pressurised CO₂ pipelines by, for the first time, accounting for operational and failure uncertainties as probabilistic variables. Based on a case study for a 300 km, 309.6 mm internal diameter CO₂ pipeline that operates at 129 bar and 307.24 K for a real CCS project, the MOO technique is applied and assessed to ascertain its effectiveness in curbing the risks identified from the case study while minimising ESDV costs. Starting with modelling the uncertainties in the important pipeline characteristics and operating conditions using standard Probability Density Functions (PDFs), a Monte Carlo simulation involving the random sampling from these PDFs is performed to obtain the probability distribution of the risk associated with pipeline failure. Based on the obtained probability distribution, the risks are mapped onto the objective function space to create a probabilistic solution plane for the decision makers to determine the optimal ESDV configuration. The efficacy of the proposed technique is demonstrated using a comparative study where the risk is treated deterministically as the worst-case scenario. The findings reveal that more cost-effective risk mitigation solutions can be attained when the risk is taken probabilistically, highlighting the importance of incorporating operational and failure uncertainties as part of the decision-making process when configuring in-line ESDVs for CO₂ pipelines.

Impact Statement

This thesis proposed an advanced safety analysis approach for pressurised CO₂ transmission pipelines. Three techniques addressing the principal challenges involving the critical facets of the safety analysis process were developed. These include an analytically based pipeline decompression model dealing with the high computational costs usually associated with numerically based models, a robust method to reliably estimate the failure hole size probability distribution with the presence of limited pipeline failure statistics, and a probabilistic multi-objective optimisation technique to optimise the emergency shutdown valve configuration as part of the risk mitigation planning for pressurised pipelines.

As Carbon Capture Utilisation and Storage being extensively deployed globally as a key solution to combat global warming, and with hydrocarbons expected to maintain their significance in ensuring energy security during the global quest to net zero carbon emissions, significant amounts of CO₂ and hydrocarbons will be transported via high-pressure pipeline networks. Given that CO₂ is an asphyxiant at high concentrations and hydrocarbons are highly flammable and explosive, their safe operation is thus of paramount importance. The approach developed can be directly employed to the quantitative failure consequence assessment of the transmission pipelines.

In addition to the above, this proposed approach offers a novel and fundamental insight into the probabilistic assessment of risks associated with pressurised pipeline failures, contrasting with traditional quantitative risk assessments which typically perceive risks deterministically, therefore providing guidelines for more cost-effective emergency planning and mitigation measures for pressurised pipelines.

I do hope we have advanced safety for humanity.

To my parents, and Wanting.

Acknowledgements

I wish to thank the following people and organisations who have contributed so much in many ways to facilitate the completion of this work.

To my supervisor, Prof. Haroun Mahgerefteh for taking the risk and your excellent supervision.

To my friends, Jianhao, Kaiqiao, Haiyue, Fidal and Yao. It has been a pleasure meeting with you all.

To Dr. Sergey Martynov, Dr. Richard Porter and Dr Elena Catalanotti. Thank you for all the motivation, advice and criticism through the course of my time at UCL.

To the Faculty of Engineering, UCL and China Scholarship Council for the financial support.

To the technical and admin. staff of the Department of Chemical Engineering, UCL.

Finally, to Paopao and Tiaotiao for all the joy along the way.

Table of Contents

List of Publications	II
Abstract.....	III
Impact Statement	VI
Acknowledgements.....	VIII
Table of Contents	IX
Nomenclature.....	XIII
Chapter 1: Introduction.....	- 1 -
1.1 Climate Change and Carbon Capture and Storage	- 1 -
1.2 Pressurised Pipeline Safety	- 7 -
1.3 Research Aims and Objectives.....	- 11 -
Chapter 2: Literature Review.....	- 14 -
2.1 Modelling Pressurised Pipeline Decompression.....	- 14 -
2.1.1 Introduction.....	- 14 -
2.1.2 Background Theory	- 14 -
2.1.3 Applications of the HEM Model in Modelling Pipeline Decompression	- 24 -
2.2 Configuring Emergency Shutdown Valves for Pressurised Pipelines ..	- 46 -
2.2.1 Introduction.....	- 46 -

2.2.2 Quantitative Risk Assessment for Pressurised CO ₂ Pipelines	- 46 -
2.2.3 Multi-Objective Optimisation.....	- 64 -
2.2.4 Applications of MOO for Pressurised Pipelines	- 72 -
Chapter 3: An Analytically Based Pressurised Pipeline Decompression Model	- 85 -
3.1 Introduction.....	- 85 -
3.2 Theory	- 87 -
3.2.1 The Discharge Model.....	- 87 -
3.2.2 Physical Properties.....	- 89 -
3.2.3 Initial Conditions	- 92 -
3.2.4 Boundary Conditions	- 94 -
3.2.5 Non-isentropic Effect.....	- 96 -
3.2.6 Algorithm	- 97 -
3.3 Verification.....	- 99 -
3.3.1 Case Study	- 99 -
3.3.2 Simulation of Un-isolated Releases	- 100 -
3.3.3 Simulation of Isolated Releases	- 106 -
3.3.4 Source of Errors	- 110 -
3.4 Computational Runtimes	- 113 -
3.5 Concluding Remarks.....	- 114 -

Chapter 4: An Analytical Approach to Estimate Failure Puncture Size Probability Distribution for Pressurised CO ₂ Pipelines.....	- 116 -
4.1 Introduction.....	- 116 -
4.2 Methodology	- 118 -
4.2.1 Data Review	- 118 -
4.2.2 Statistical Distribution Models	- 120 -
4.2.3 Distribution Fitting.....	- 120 -
4.2.4 Determination of Probability Distribution	- 123 -
4.3 Results and Discussion	- 126 -
4.3.1 Monte Carlo Simulation Results.....	- 126 -
4.3.2 Failure Size Probability Distribution Results	- 130 -
4.4 Concluding Remarks.....	- 140 -
 Chapter 5: A Probabilistic Multi-Objective Optimisation Technique to Optimise the Emergency Shutdown Valve Configuration for Pressurised CO ₂ Pipelines	 - 142 -
5.1 Introduction.....	- 142 -
5.2 Methodology	- 144 -
5.2.1 Parameter Uncertainties	- 144 -
5.2.2 Discharge Modelling.....	- 145 -
5.2.3 Dispersion Modelling.....	- 148 -

5.2.4 Risk Estimation.....	- 149 -
5.2.5 Risk Probability Distribution	- 150 -
5.2.6 Multi-objective Optimisation.....	- 152 -
5.3 Results and Discussion	- 154 -
5.3.1 Case Study	- 154 -
5.3.2 Risk Probability Distribution Results	- 158 -
5.3.3 Multi-objective Optimisation Results	- 161 -
5.3.4 Comparative Study Results.....	- 165 -
5.4 Concluding Remarks.....	- 166 -
Chapter 6: Conclusions and Future Work	- 168 -
6.1 Conclusions.....	- 168 -
6.2 Suggestions for Future Work	- 173 -
6.2.1 Extension of the MVBM to Accounting for Various Upstream Sources	- 173 -
6.2.2 Sample Quality Measurement.....	- 173 -
6.2.3 Modelling of Parameter Uncertainties using Complicated Methods....	-
174 -	
References.....	- 175 -

Nomenclature

A	Area affected by CO ₂ release from pipeline (m ²)
\tilde{A}	Available heat transfer area per unit volume (m ⁻¹)
A_f	Valve opening area (m ²)
A_{ori}	Orifice area (m ²)
A_P	Pipe cross-section area (m ²)
A_p	Puncture area (m ²)
a	Lower limit of continuous uniform distribution
B	Number of bootstrap samples
b	Upper limit of continuous uniform distribution
C	CO ₂ concentration (vol/vol)
C_D	Discharge coefficient
C_d	Valve discharge coefficient
C_P	Isobaric specific heat capacity (J kg ⁻¹ K ⁻¹)
$C_{P,l}$	Isobaric specific heat capacity of the liquid phase (J kg ⁻¹ K ⁻¹)
$C_{P,w}$	Isobaric specific heat capacity of the pipe wall (J kg ⁻¹ K ⁻¹)
c	Speed of sound (m s ⁻¹)
c_{ori}	Speed of sound at the orifice (m s ⁻¹)
D	K-S statistic
D_{ext}	Pipe external diameter (m)
D_{in}	Pipe internal diameter (m)
d	ESDV spacing (m)
E	Specific total energy (J kg ⁻¹)
E_o	Specific total energy of the pipe bulk fluid (J kg ⁻¹)
e	Specific energy (J kg ⁻¹)
e_o	Specific energy of the pipe bulk fluid (J kg ⁻¹)
F	Body force (N)

F_c	Cumulative failure frequency (times year ⁻¹)
F_g	Gravitational force (N)
F_L	Likelihood function
F_w	Fluid/wall friction force (N)
f_a	Aggregated function
f_w	Fanning friction factor
G	Mass discharge rate (kg s ⁻¹)
G_{in}	Mass discharge rate at the inlet (kg s ⁻¹)
G_{ori}	Mass discharge rate at the orifice (kg s ⁻¹)
G_{up}	Mass discharge rate upstream the orifice (kg s ⁻¹)
g	Gravitational acceleration (m s ⁻²)
H	Specific total enthalpy (J kg ⁻¹)
H_{in}	Specific total enthalpy at the inlet (J kg ⁻¹)
H_{ori}	Specific total enthalpy at the orifice (J kg ⁻¹)
H_{up}	Specific total enthalpy upstream the orifice (J kg ⁻¹)
h	Specific enthalpy (J kg ⁻¹)
$h_{l,l}$	Specific latent heat of the liquid phase (J kg ⁻¹)
h_{ori}	Specific enthalpy at the orifice (J kg ⁻¹)
h_{up}	Specific enthalpy upstream the orifice (J kg ⁻¹)
I	Identity matrix
J	Objective function
L	Pipe length (m)
M	Mass (kg)
M_o	Mass of the pipe bulk fluid (kg)
M_{total}	Total inventory loss (kg)
N	ESDV number
Nu	Nusselt number

P	Pressure (bar)
P_c	Critical pressure (bar)
P_d	Probability of death
P_{ext}	Ambient pressure (bar)
P_f	Pipeline failure probability
P_{in}	Pressure at the inlet (bar)
P_{ori}	Fluid pressure at the orifice (bar)
P_p	Puncture perimeter (m)
P_r	Probit value
P_{up}	Pressure upstream the orifice (bar)
P_v	Pressure drop across the valve (bar)
ΔP	Infinitesimal change in pressure (bar)
Pr	Prandtl number
Pr_l	Prandtl number of the liquid phase
\dot{Q}	Fluid/wall heat transfer (J)
Q_v	Volumetric flow rate ($\text{m}^3 \text{s}^{-1}$)
q	Net heat flux into the pipe (W m^{-2})
R	Universal gas constant ($\text{J mol}^{-1} \text{K}^{-1}$)
Re	Reynolds number
R_{in}	Pipe internal radius (m)
r	Annual human fatality (fatalities year^{-1})
r_d	Discount rate
s	Specific entropy (J K^{-1})
s_o	Specific entropy of the pipe bulk fluid (J K^{-1})
s_{ori}	Specific entropy at the orifice (J K^{-1})
s_{up}	Specific entropy upstream the orifice (J K^{-1})
T	Temperature (K)

T_c	Critical temperature (K)
T_f	Fluid temperature (K)
T_{in}	Temperature at the inlet (K)
T_o	Temperature of the pipe bulk fluid (K)
T_{up}	Temperature upstream the orifice (K)
T_w	Pipe wall temperature (K)
t	Time (s)
t_a	Valve activation time (s)
t_c	Valve closure time (s)
U	Overall heat transfer coefficient (W m^{-2})
u	Velocity (m s^{-1})
u_{ori}	Fluid velocity at the orifice (m s^{-1})
u_{up}	Fluid velocity upstream the orifice (m s^{-1})
u_v	Linear closure rate of the valve (cm s^{-1})
V	Specific volume ($\text{m}^3 \text{kg}^{-1}$)
V_m	Molar volume ($\text{m}^3 \text{mol}^{-1}$)
V_o	Pipe volume (m^3)
V_{PN}	Present net value of a single ESDV cost (£)
W_S	Shaft work (J)
x_{up}	Pipe failure location (m)
x_v	Distance traversed by the valve (m)
yr	Average lifetime of the ESDV (years)
Z	Compressibility factor
z	Elevation (m)

Greek Symbols

α	Scale parameter of Weibull distribution
α_s	Level of significance
β	Shape parameter of Weibull distribution
β_x	Fluid/wall friction ($\text{kg m}^{-2} \text{s}^{-2}$)
γ	Ratio of specific heats
ε	Pipe roughness (m)
θ	Probability distribution parameter
$\hat{\theta}$	Maximum likelihood estimator of θ
$\dot{\theta}$	Pipe inclination angle relative to the horizontal plane ($^\circ$)
κ	Isothermal coefficient of volumetric expansion ($\text{m s}^2 \text{kg}^{-1}$)
λ	Overall pipeline failure frequency (times year ⁻¹)
λ_0	Pipeline failure frequency (times km ⁻¹ year ⁻¹)
μ	Mean of lognormal/normal distribution
μ_f	Fluid viscosity ($\text{kg m}^{-1} \text{s}^{-1}$)
μ_g	Viscosity of the vapour phase ($\text{kg m}^{-1} \text{s}^{-1}$)
μ_l	Viscosity of the liquid phase ($\text{kg m}^{-1} \text{s}^{-1}$)
ξ	Isobaric coefficient of volumetric expansion ($\text{m s}^2 \text{kg}^{-1}$)
ρ	Density (kg m^{-3})
ρ_g	Density of the vapour phase (kg m^{-3})
ρ_l	Density of the liquid phase (kg m^{-3})
ρ_o	Density of the pipe bulk fluid (kg m^{-3})
ρ_{ori}	Fluid density at the orifice (kg m^{-3})
ρ_p	Population density (people m ⁻²)
ρ_w	Pipe wall density (kg m^{-3})
σ	Standard deviation of lognormal/normal distribution
σ_l	Surface tension of the liquid phase (N m^{-1})

φ	Isochoric thermodynamic function
ϕ	Fluid Mass-specific properties
ϕ_g	Mass-specific properties of the vapour phase
ϕ_l	Mass-specific properties of the liquid phase
χ	Fluid quality
ω	Acentric factor
ω_v	Percentage of the valve opening area

Abbreviations

CCS	Carbon Capture and Storage
CCUS	Carbon Capture Utilisation and Storage
CDF	Cumulative Distribution Function
CI	Confidence Interval
CNGS	Compound Nested Grid System
DFM	Drift Flux Mixture
ECDF	Empirical Cumulative Distribution Function
EOR	Enhanced Oil Recovery
EoS	Equation of State
EPD	Equivalent Puncture Diameter
ESDV	Emergency Shutdown Valve
FBR	Full Bore Rupture
FDM	Finite Difference Method
FEM	Finite Element Method
F-N	Frequency-Number
GCD	Generalised Coefficient of Determination
HAZID	Hazard Identification
HEM	Homogeneous Equilibrium Mixture
HRM	Homogeneous Relaxation Mixture
IR	Individual Risk
i.d.	internal diameter
MLE	Maximum Likelihood Estimator
MOC	Method of Characteristic
MOO	Multi-Objective Optimisation
MSE	Mean Squared Error
MVBM	Modified Vessel Blowdown Model

ODE	Ordinary Differential Equation
PC	Principal Component
PDE	Partial Differential Equation
PDF	Probability Density Function
PR EoS	Peng-Robinson Equation of State
QRA	Quantitative Risk Assessment
RCV	Remote Control Valve
ROC	Rank Order Centroid
RS	Rank Sum
SGS	Simple Grid System
SIL	Safety Integrity Level
TFM	Two Fluid Mixture
T&S	Transportation & Storage
VBM	Vessel Blowdown Model

Chapter 1: Introduction

1.1 Climate Change and Carbon Capture and Storage

The intensive use of fossil fuels (i.e. oil, gas and coal) has produced excessive CO₂ emissions worldwide, giving rise to global warming and climate change. Driven by an extremely rapid economic recovery since the Covid-19 pandemic, the global CO₂ emissions from the energy sector reached 36.3 gigatonnes (Gt) in 2021, representing the highest annual level in history (IEA, 2022). According to Intergovernmental Panel on Climate Change (IPCC, 2013), signals of climate change are already visible: the amounts of snow and ice in the Northern Hemisphere have diminished; atmosphere and oceans have warmed up, and sea level has risen since 1950. The speed of the observed changes is unprecedented and will continue to grow if not dealt with imminently, leading to irreversible impacts.

One of the key technologies destined to address the issue is Carbon Capture Utilisation and Storage (CCUS), which involves capturing the excessive CO₂ emissions from large emission sources such as fossil fuel power plants and industrial operations such as cement and steel making for the subsequent geological storage or utilisation.

According to International Energy Agency (IEA, 2021), it is estimated that some 100 Gt of CO₂ is expected to be captured and stored between 2025 and 2050. A failure to develop CCUS at large scale would significantly delay the progress on meeting the net zero emission targets and would require \$ 15 trillion of additional investment in other low-carbon technologies (e.g. solar, wind, hydro) to achieve the same level of emissions reduction.

According to the latest figures, there are already 133 commercial CCUS projects in operation or under development (GCCSI, 2022). Table 1.1 summarises the commercial

CCUS facilities in operation as of 2022. Also included are the country-specific project distribution and the respective industry-specific counts for each country. Historically, CCUS projects tend to be vertically integrated, that is a capture plant is usually built along with its own dedicated downstream transport system. This favours large-scale projects, where economies of scale make downstream costs more tangible. Recently, there has been a trend towards projects sharing CO₂ Transport and Storage (T&S) infrastructure. The use of shared T&S systems means that smaller projects can also benefit from economies of scale, thus accelerating the extensive deployment of CCUS technology. According to Global Carbon Capture and Storage (CCS) Institute (GCCSI, 2021), 12 countries now have CCS networks in operation or under development. These countries, along with their respective largest network by capture capacity are summarised in table 1.2.

An essential element of the CCS chain is the transportation of the captured CO₂ to the storage sites. As can be read from both tables 1.1 and 1.2, almost all the operating CCUS facilities and planned major CCS networks adopt pipeline as the main transport mode. As of now, the CCUS projects in operation involves over 8,000 km of CO₂ pipelines, almost entirely for enhanced oil recovery and mostly located in the United States (IEA, 2021). According to International Energy Agency (IEA, 2010), the demand in CO₂ pipeline infrastructure is expected to grow to an estimated length of about 200,000 to 550,000 km by 2050 depending on the uptake of CCUS. In Europe, the CO₂ infrastructure network is projected to range from 5,000 to 15,000 km in 2030 and from 11,000 to 20,000 km in 2050, depending on the availability of storage locations and number of CCUS units installed (Haszeldine et al., 2010; Morbee et al., 2012).

Apart from the above, in order to ensure sustained economic growth and secure energy supplies, the transition away from fossil fuels as part of the quest for reducing CO₂ emissions requires the continued use of fossil fuels. This is underlined by the fact that the proportion of hydrocarbon resources in the global energy mix is estimated to amount

to c.a. 76% of the total by 2035 (BP, 2020). As a result, the existing hydrocarbon pipeline networks (over 4.4 million km in length (CIA, 2021)) are expected to remain in operation for the coming decades. China, as the world's largest energy consumer, for example, plans to expand oil and gas productions as part of its future energy reforms (SCIO, 2020).

In essence, pressurised pipelines are destined to play a major role both as a means of ensuring energy supply as well as tackling CO₂ emissions in the foreseeable future.

Table 1.1: Summary of commercial CCUS facilities in operation as of 2022 (GCCSI, 2022).

Country (Project count)	Industry (Project count)	Facility name	Operation year	CO₂ capture capacity (Mt/y)	Transport mode	Storage type
US (12)	Natural gas processing (4)	Shute Creek Gas Process Plant	1986	7.0	Pipe	EOR
		Century Plant	2010	5.0	Pipe	EOR
		Terrell Natural Gas Plant (formerly Val Verde)	1972	0.4 to 0.5	Pipe	EOR
		Core Energy CO ₂ EOR	2003	0.35	Pipe	EOR
	Ethanol production (3)	Illinois Industrial CCS	2017	0.55 to 1	Pipe	Dedicated
		Arkalon CO ₂ Compression Facility	2009	0.23 to 0.29	Pipe	EOR
		Bonanza Bio-energy CCUS EOR	2012	0.1	Pipe	EOR
	Fertiliser production (3)	Coffeyville Gasification Plant	2013	0.9	Pipe	EOR
		PCS Nitrogen CCS	2013	0.2 to 0.3	Pipe	EOR
		Enid Fertiliser	1982	0.1 to 0.2	Pipe	EOR
	Synthetic natural gas (1)	Great Plains Synfuels Plant (Weyburn/Midale)	2000	1.0 to 3.0	Pipe	EOR
	Hydrogen production (1)	Air Products Steam Methane Reformer	2013	1.0	Pipe	EOR
Canada (4)	Hydrogen production (2)	ACTL with NWR Sturgeon Refinery	2020	1.3 to 1.6	Pipe	EOR
		Quest	2015	1.2	Pipe	Dedicated
	Power generation (1)	Boundary Dam 3 CCS facility	2014	0.8 to 1	Pipe	Various
	Fertiliser production (1)	ACTL with Nutrien	2020	0.2 to 0.3	Pipe	EOR

Table 1.1: Summary of commercial CCUS facilities in operation as of 2022 (GCCSI, 2022) (continued).

Country (Project count)	Industry (Project count)	Facility name	Operation year	CO ₂ capture capacity (Mt/y)	Transport mode	Storage type
China (4)	Natural gas processing (2)	CNPC Jilin Oil Field CO ₂ EOR	2018	0.35 to 0.6	Pipe	EOR
		CNOOC South China Sea Offshore CCS	2021	0.3	N/A	Dedicated
	Chemical production (1)	Sinopec Zhongyuan CCUS	2006	0.12	Truck	EOR
	Methanol production (1)	Karamay Dunhua Oil Technology CCUS EOR	2015	0.1	Truck	EOR
Norway (2)	Natural gas processing (2)	Sleipner CO ₂ Storage	1996	1.0	Pipe	Dedicated
		Snøhvit CO ₂ Storage	2008	0.7	Pipe	Dedicated
Brazil (1)	Natural gas processing (1)	Petrobras Santos Basin Oil Field CCS	2011	4.6	Direct re injection	EOR
Australia (1)	Natural gas processing (1)	Gorgon CO ₂ Injection	2019	3.4 to 4	Pipe	Dedicated
Qatar (1)	Natural gas processing (1)	Qatar LNG CCS	2019	2.1	Pipe	Dedicated
UAE (1)	Iron & steel production (1)	Abu Dhabi CCS with Emirates Steel	2016	0.8	Pipe	EOR
Saudi Arabia (1)	Natural gas processing (1)	Uthmaniyah CO ₂ EOR	2015	0.8	Pipe	EOR
Hungary (1)	Natural gas processing (1)	MOL Szank Field CO ₂ EOR	1992	0.059 to 0.157	N/A	EOR
Iceland (1)	Direct air capture (1)	Orca	2021	0.004	N/A	Dedicated

Table 1.2: Selected major CCS networks (GCCSI, 2021).

Country	Largest network by capture capacity	Network status	CO₂ capture capacity (Mt/y)	Transport type	Primary storage type
US	Houston Ship Channel CCS Innovation Zone	Early development	100.0	Pipe	EOR
Netherlands	Aramis	Early development	20.0	Pipe, Ship	Dedicated
UK	Zero Carbon Humber	Advanced development	18.3	Pipe	Dedicated
Canada	Canada ACTL	In operation	14.6	Pipe	EOR
France	Dartagnan	Early development	10.0	Pipe, Ship	Dedicated
Belgium	Antwerp@C	Advanced development	9.0	Pipe	Dedicated
UAE	Abu Dhabi Cluster	In operation	5.0	Pipe	EOR
Australia	CarbonNet	Advanced development	5.0	Pipe	Dedicated
Norway	Langskip	Advanced development	5.0	Pipe, Ship	Dedicated
Italy	Ravenna Hub	Advanced development	4.0	Pipe	Dedicated
Denmark	Greensand	Advanced development	3.5	Pipe, Ship	Dedicated
China	Xinjiang Junggar Basin CCS Hub	In operation	3.0	Pipe, Truck	EOR

1.2 Pressurised Pipeline Safety

Both pressurised CO₂ and hydrocarbon pipelines may fail for a number of reasons such as external interference, corrosion, ground movement or material defect (Mahgerefteh et al., 2012a). Given that CO₂ is toxic at concentrations above 7% vol/vol (Kruse and Tekiela, 1996) and hydrocarbons are highly flammable and explosive, the failure of such pipelines, especially near populated areas, can lead to catastrophic consequences, resulting in loss of valuable inventory, damage to property, environmental pollution, or injuries & fatalities. For example, on 23 February 2020, a 24-inch pipeline transporting pressurised CO₂ owned by Denbury Enterprises ruptured near a highway close to the village of Satarita in Mississippi, US. The unhindered escape of the CO₂ resulted in the evacuation of over 300 residents, among which 46 were hospitalised. The incident in total caused nearly \$ 4 million economic losses. A failure investigation conducted by US Department of Transportation showed that the incident resulted from heavy rains which caused a landslide creating axial strain on the pipe and led to a full circumferential girth weld failure (Mathews, 2022). According to official records, the US, known for its stringent pipeline safety regulations among developed nations, has documented 12,794 pipeline loss of containment incidents over the past two decades, involving various fluid types (e.g. CO₂, oil, gas) and severity levels. These in total have caused 276 fatalities, 1,144 injuries and over \$ 10 billion worth of damage (PHMSA, 2022). Given the above, the safety of pressurised pipelines must be ensured during their operations.

Central to the above is the safety assessment of pressurised pipelines which usually consists of three key steps, as follows:

- 1) Pipeline decompression models are developed to predict the outflow and decompression characteristics in the event of pipeline failure, including the time-varying mass discharge rate, pressure, temperature, and phase composition.

- 2) Using the outflow data obtained from the pipeline decompression models, the Quantitative Risk Assessment (QRA) involving calculation of the magnitude of the failure consequences and the occurrence probability of the failure events is performed to determine the individual and societal risk levels.
- 3) Based on the calculated individual and societal risk levels from QRA, appropriate control and emergency mitigation planning measures are proposed to reduce the failure consequences to as low as reasonably practicable in the event of pipeline failure.

Given the above, the development of accurate, robust, and computationally efficient approaches to handle these key steps has been the focus of considerable attention. Their main features and limitations are discussed in the following.

As the starting point, the development of pipeline decompression models has been the focus of considerable attention. Several numerically based pipeline decompression models have been developed over the years (see for example Brown et al., 2013; Chen et al., 1995; Mahgerefteh et al., 1999; Oke et al., 2003). Given that in principle the mathematical problem addressed involves solving the conservation equations of mass, momentum and energy which are a set of coupled, non-linear and high-order partial differential equations usually containing terms that are not analytically solvable, their solutions are sought using numerical techniques (Flatt, 1986). Previous attempts include a Finite Difference Method (FDM) (see for example Bendiksen et al., 1991; Chen, 1993), a Finite Element Method (FEM) (see for example Bisgaard et al., 1987; Lang, 1991) and the Method of Characteristic (MOC) (see for example Chen et al., 1992; Olorunmaiye and Imide, 1993). Given that these methods invariably involve the numerical discretisation of the pipe fluid flow field into several small elements, they all share the fundamental drawback of long computational runtimes (Mahgerefteh et al., 2011). For a typical 100 km length, 800 mm internal diameter (i.d.) natural gas pipeline

experiencing a 20 mm puncture, for example, the CPU time for simulating its complete decompression typically ranges from days to weeks depending on the computer processing speed employed.

To address the above problem, many workers have proposed simplistic pipeline decompression models. Some notable attempts include a unified outflow model (Norris, 1994; Norris and Puls, 1993), a quasi-steady state model (Webber et al., 1999) and a Vessel Blowdown Model (VBM) (Mahgerefteh et al., 2011). These models were developed mainly based on steady state flow assumption for which analytical solutions can be obtained, largely addressing the issue of long computational runtimes associated with numerically based techniques (e.g. FEM, FDM and MOC) used for simulating pipeline failure. However, these models are mostly suitable only for specific failure scenarios, displaying limited applicability.

Turning to the second step where the QRA is involved, two types of studies are usually performed, with one type being modelling the failure consequences such as dense-gas dispersions (see for example Ermak, 1990; Ott and Nielsen, 1996; Witlox and A. Holt., 1999), fires (see for example Chamberlain, 1987; Johnson et al., 1994; van den Bosh and Weterings, 1997), or explosions (see for example Wiekema, 1980), and the other based on collecting historical pipeline incident statistics and developing corresponding techniques to estimate the pipeline failure frequencies (see for example Chaplin, 2017; Duncan and Wang, 2014, 2014; Miao and Zhao, 2012).

Nevertheless, despite the fact that the failure hole size, usually expressed in terms of the failure modes (e.g. leak, puncture, or Full Bore Rupture (FBR)), directly affects the magnitude of the failure consequences and hence the results of QRA, little attention has been paid to their probability of occurrence. The above requires the use of sufficiently large failure statistics data to reliably derive the corresponding failure hole size probability distribution. In previous studies, the most popular method is based on

deriving the corresponding histograms using existing pipeline failure statistics (see for example Duncan and Wang, 2014; Medina et al., 2012; Nyborg et al., 2011; Rusin and Stolecka, 2015). This involves first segmenting the entire range of failure hole sizes into a series of intervals (bins) and then counting how many values fall into each bin. Despite its simplicity, this method accounts for no information regarding the statistical significance of the samples being used to derive the histogram. Whether the size or quality of the samples suffices for a reliable histogram remains largely unclear. This issue is particularly challenging for CO₂ pipelines given their 1) relatively low number currently in operation and hence the small pool of failure statistics, and 2) different operating conditions compared to hydrocarbon pipelines and therefore the uncertainties in drawing analogies.

Based on the results of QRA, one can subsequently propose safety measures to mitigate the failure consequences in the event of pipeline failure. In the case of pressurised pipelines, inline Emergency Shutdown Valves (ESDVs) are extensively employed as a front-line mitigation tool (Martynov et al., 2018a). Configuring the ESDVs along the pipe length which involves determining their type, number, operation settings and strategic positioning that minimise the valve costs whilst reducing the risks to as low as reasonably practicable presents significant decision-making challenges. The solutions to such challenges are usually sought using the Multi-Objective Optimisation (MOO) technique.

The efficacy of applying MOO in finding the optimal ESDV configurations heavily depends on the accuracy of the metrics used to define the risk of pipeline failure. Nevertheless, in most of the relevant studies (see for example Brown et al., 2014; Yu et al., 2022), such metrics are defined relatively simply, that is, based on the QRA of one customised failure scenario (usually FBR for representing the worse-case scenario) assuming 100% occurrence probability. Nevertheless, given that uncertainties and variations exist in pipe characteristics and operating conditions (e.g. failure hole size,

failure location, fluid pressure), the failure scenario can vary greatly from one accident to the next, impacting the magnitudes of the failure consequences and the subsequent solution to the MOO problem. For example, Koornneef et al. (2009) performed a sensitivity analysis to evaluate the impact of the uncertainties in the input parameters on the results of QRA for a 20 km length, 406 mm i.d. pressurised CO₂ pipeline as the case study. The results showed that the predicted safe distance could vary largely from 0 to 204 m.

1.3 Research Aims and Objectives

The aim of this thesis is to develop advanced tools for the safety assessment of pressurised CO₂ and hydrocarbon pipelines, as part of the global quest to zero carbon emissions. The research focuses on addressing critical limitations in the three key steps of the assessment process involving pipeline decompression modelling, QRA and emergency mitigation planning. Given the above, the main objectives of this thesis are to develop, test, and assess:

- 1) A computationally efficient Modified Vessel Blowdown Model (MVBM) addressing the fundamental limitations of VBM in handling un-isolated releases and fluid/wall heat exchanges.
- 2) An analytical approach to reliably estimate the failure hole size probability distribution for pressurised CO₂ pipelines accounting for the statistical significance of the failure data being employed.
- 3) A probabilistic MOO technique to optimise the ESDV configuration for pressurised CO₂ pipelines accounting for the uncertainties in the pipe characteristics and operating conditions.

The following presents an overview of each of the proceeding chapters:

In Chapter 2, a comprehensive review of pressurised pipeline safety is presented. This chapter is divided into two parts. The first part focuses on the modelling of pressurised pipeline decompression. It commences with a detailed description of the background theory of the modelling approaches, mainly including the fluid flow dynamics, constitutive relations for fluid/wall interactions and physical property calculations. This is followed by a review of the applications of the Homogeneous Equilibrium Mixture (HEM) model for predicting pipeline decompression. The second part focuses on configuring ESDVs for pressurised pipeline. This part starts with a review of the QRA for pressurised CO₂ pipelines summarising the methods for modelling dense gas dispersion, calculating pipe failure frequency, and evaluating individual and societal risk levels. This is followed by a detailed description of the theoretical basis for the MOO technique covering the mathematical formulation of a MOO problem and the solution methods. Next, a review focusing on the applications of MOO in optimising the ESDV configuration and the design for pressurised pipelines is presented.

Chapter 3 presents the development and testing of the MVBM addressing the fundamental limitations of VBM in handling un-isolated releases and fluid/wall heat exchanges. The modified model is tested and compared against the results obtained using the VBM as well as an extensively validated but computationally demanding University College London (UCL) pipeline decompression model. The chapter commences with a detailed description of the background theory of the UCL model and VBM. Following this, the theoretical basis of the MVBM mainly including the fluid flow dynamics, physical properties, algorithm as well as the initial and boundary conditions is described. This is followed by its verification against the UCL model and VBM. The tests cover a wide range of hypothetical nevertheless realistic failure scenarios spanning various puncture diameters, feed flow rates and pipe lengths. Finally, an analysis of the computational runtimes is given.

In Chapter 4, the development and application of the analytical approach to estimate

the failure hole size probability distribution accounting for the data sample statistical significance is given. This chapter starts with an initial selection of the historical pipeline failure statistics suitable for the purpose of this study, followed by the description of the methodology employed to obtain a reliable failure hole size probability distribution using the selected statistics. Next, using the proposed methodology, the failure hole size probability distribution for pressurised CO₂ is derived. Comparative data for natural gas and crude oil pipelines are also presented and discussed.

Chapter 5 presents the development and application of the probabilistic MOO technique for optimising the inline ESDV configuration for pressurised CO₂ pipelines accounting for the uncertainties in the pipe characteristics and operating conditions. The above is based on treating the risk associated with pipeline failure as a probabilistic variable. The approach employed for modelling the parameter uncertainties is first presented together with the mathematical modelling of the failure consequences and the methods for evaluating the associated risk. This is followed by the description of the optimisation problem, detailing the optimisation variables and objective functions being considered. The optimisation results are next presented based on a case study involving a 300 km length, 309.6 mm i.d. pipeline transporting CO₂ initially at 129 bar and 307.24 K. Finally, a comparative study where the risk is taken deterministically as that resulting from the worst-case scenario is performed to demonstrate the effectiveness of the developed technique.

Chapter 6 presents a summary of the main conclusions of this thesis, followed by recommendations for future work.

Chapter 2: Literature Review

In this chapter, a comprehensive review of the key aspects of pressurised pipeline safety assessment, including modelling pressurised pipeline decompression and configuring inline Emergency Shutdown Valves (ESDVs) as a front-line tool for risk reduction is presented.

2.1 Modelling Pressurised Pipeline Decompression

2.1.1 Introduction

In essence, the quantitative consequence assessment for pipeline failures requires the development of rigorous mathematical relations encapsulating all the important physical processes taking place during pipeline decompression as well as employing appropriate mathematical techniques for their solutions.

The following section reviews the modelling of pressurised pipeline decompression and is organised as follows. First, the background theory of pipeline decompression modelling is described, chiefly focusing on the formulation of fluid dynamics phenomena accounting for multi-phase flows. Next, selected examples of the applications of Homogenous Equilibrium Mixture (HEM) assumption in pipeline decompression modelling are presented and reviewed.

2.1.2 Background Theory

2.1.2.1 General Conservation Equations for Fluid Dynamics

For any type of flow, a generic form of the conservation equations of mass, momentum and energy describing the fluid dynamics of the k^{th} fluid phase within an arbitrary flow control volume with a control surface can be written as (Zheng, 2018):

$$\frac{\partial \alpha_k \bar{\rho}_k}{\partial t} + \nabla \cdot (\alpha_k \bar{\rho}_k \underline{\mathbf{u}}_k) + I_k = 0 \quad 2.1$$

$$\frac{\partial \alpha_k \bar{\rho}_k \underline{\mathbf{u}}_k}{\partial t} + \nabla \cdot (\alpha_k \bar{\rho}_k \underline{\mathbf{u}}_k \underline{\mathbf{u}}_k) + \nabla \cdot (\alpha_k \bar{P}_k \mathbf{I}) - \nabla \cdot \alpha_k (\underline{\boldsymbol{\tau}}_k^{tb} + \bar{\underline{\boldsymbol{\tau}}}_k) + I_k^{\underline{\mathbf{u}}_k} - \alpha_k \bar{\mathbf{F}}_k = 0 \quad 2.2$$

$$\begin{aligned} \frac{\partial \alpha_k \bar{\rho}_k \bar{E}_k}{\partial t} + \nabla \cdot (\alpha_k \bar{\rho}_k \underline{\mathbf{u}}_k \bar{E}_k) + \nabla \cdot (\alpha_k \bar{P}_k \mathbf{I} \cdot \underline{\mathbf{u}}_k) - \nabla \cdot (\alpha_k \bar{\underline{\boldsymbol{\tau}}}_k \cdot \underline{\mathbf{u}}_k) + \nabla \cdot \alpha_k (\underline{\mathbf{q}}_k^{tb} + \bar{\underline{\mathbf{q}}}_k) \\ + \bar{P}_k \frac{\partial \alpha_k}{\partial t} + I_k^{E_k^*} - \alpha_k (\bar{\underline{\mathbf{F}}}_k \cdot \underline{\mathbf{u}}_k + \bar{Q}_k) = 0 \end{aligned} \quad 2.3$$

where the subscript, k denotes the k^{th} fluid phase present in the flow. The superscript, tb denotes the turbulence. The scalars, α_k , ρ_k , P_k , E_k and \dot{Q}_k are respectively the volume fraction, density, pressure, total energy (defined as $E_k = e_k + |\underline{\mathbf{u}}_k|^2/2$, where e_k is the internal energy and $|\underline{\mathbf{u}}_k|^2/2$ is the kinetic energy) and added heat per volume of the k^{th} fluid phase. The vectors, $\underline{\mathbf{u}}_k$, $\underline{\mathbf{F}}_k$ and $\underline{\mathbf{q}}_k$ respectively represent the velocity, body force and heat flux. $\underline{\boldsymbol{\tau}}_k$ on the other hand, denotes the stress tensor. The interface mass, momentum and energy interaction terms are respectively represented by I_k , $I_k^{\underline{\mathbf{u}}_k}$ and $I_k^{E_k^*}$. \mathbf{I} refers to the identity matrix. The averaging operators, $\bar{\quad}$ and $\underline{\quad}$ represent phase- and mass-weighted time-averaging, respectively.

2.1.2.2 Pipe Flow Modelling

Given the fact that the above conservation equations of mass, momentum, and energy (equations 2.1 to 2.3) are a set of highly coupled, non-linear and high-order Partial Differential Equations (PDEs), an analytical solution for these equations is not possible (Hoffman and Zucrow, 1976).

For most engineering problems involving pipe flows, the flow is usually assumed to be one-dimensional (see for example Mahgerefteh et al., 1999; Martynov et al., 2018b;

Oke et al., 2003). This assumption is considered appropriate given the fact that most pipe flows are dominated by convective effect (Saha, 1997). This means the variation of fluid properties along the streamline is much more significant than that across the pipe cross-section area. As a result, the latter can be neglected.

To account for the viscous effect resulting from the internal friction between the adjacent fluid layers (i.e. fluid/fluid friction), the viscid-inviscid interaction model (Batchelor, 1967) dividing the flow field into two separate regions is usually adopted in modelling pipe flows. This model assumes that the viscous effect is confined to a thin boundary layer near the pipe wall, thus passing the fluid/fluid friction to fluid/wall friction. The bulk flow, on the other hand, is assumed to be inviscid. Apart from the above, the momentum diffusion, energy diffusion and turbulence are usually neglected in modelling pipe flows (see for example Mahgerefteh et al., 1999; Oke et al., 2003).

Modifying equations 2.1 to 2.3 based on the above and dropping all the averaging operators, the resulting conservation equations of mass, momentum and energy describing pipe flow of the k^{th} fluid phase read:

$$\frac{\partial \alpha_k \rho_k}{\partial t} + \frac{\partial}{\partial x} \alpha_k \rho_k u_k + I_k = 0 \quad 2.4$$

$$\frac{\partial \alpha_k \rho_k u_k}{\partial t} + \frac{\partial}{\partial x} (\alpha_k \rho_k u_k^2 + \alpha_k P_k) + I_k^{u_k} - \alpha_k F_k = 0 \quad 2.5$$

$$\frac{\partial \alpha_k \rho_k E_k}{\partial t} + \frac{\partial}{\partial x} (\alpha_k \rho_k u_k E_k + \alpha_k u_k P_k) + P_k \frac{\partial \alpha_k}{\partial t} + I_k^{E_k^*} - \alpha_k (F_k u_k + \dot{Q}_k) = 0 \quad 2.6$$

2.1.2.3 Multi-phase Flow Modelling

Multi-phase flows are often encountered during pipeline decompression as a result of liquid evaporation due to low pressure or vapour condensation due to low temperature

(Saha, 1997; Zheng, 2018). Therefore, modelling the fluid dynamics for pipe flows usually requires two or more sets of the conservation equations 2.4 to 2.6 explicitly describing each constituent phase.

In real pipes, the constituent phases present in the flows have different degrees of mass, momentum and energy interactions, resulting in varying flow characteristics and leading to different phasic thermodynamic and mechanical properties. To describe the multi-phase flow phenomena, various modelling approaches generally divided into four groups have been developed (Munkejord et al., 2016; Pham and Rusli, 2016). These include Homogeneous Equilibrium Mixture (HEM) model, Homogeneous Relaxation Mixture (HRM) model, Drift Flux Mixture (DFM) model and Two Fluid Mixture (TFM) model. The four models each represent a different level of sophistication in describing the interphase interactions.

The highest level of sophistication is the TFM model where both thermodynamic and mechanical non-equilibria between the constituent phases are taken into consideration. Given this, the model is considered the most physically relevant and complete among the four models, and therefore can be applied to a wide range of flows. The next level includes the HRM and DFM models, both capable of partially handling the non-equilibrium effects resulting from limited interphase interactions. The HRM model is developed to account for thermodynamic non-equilibrium as a result of the delayed phase transition during pipeline decompression. The DFM model, on the other hand, is usually employed to model pipe flows experiencing mechanical non-equilibrium effects such as phase slip. The HEM model, which represents the lowest level of sophistication, assumes both thermodynamic and mechanical equilibria (i.e. instantaneous mass, momentum and energy exchanges) between the constituent phases, that is, the phasic pressures, temperatures or velocities are identical across phases.

Based on the above multi-phase flow models, modifying accordingly the general

conservation equations for pipe flows (equations 2.4 to 2.6) will give model-specific forms of these conservation equations.

In the case of the HEM model, since the corresponding mass, momentum and energy exchanges between fluid phases are instantaneous, the interface interaction terms, I_k , $I_k^{u_k}$, and $I_k^{E_k^*}$ in equations 2.4 to 2.6 can be ignored and the corresponding HEM model-specific conservation equations for pipe flows are given by:

$$\frac{\partial \rho}{\partial t} + \frac{\partial}{\partial x} \rho u = 0 \quad 2.7$$

$$\frac{\partial \rho u}{\partial t} + \frac{\partial}{\partial x} (\rho u^2 + P) - F = 0 \quad 2.8$$

$$\frac{\partial \rho E}{\partial t} + \frac{\partial}{\partial x} (\rho u E + P u) - (F u + \dot{Q}) = 0 \quad 2.9$$

where F represents the body force usually including the fluid/wall friction and gravitational force. \dot{Q} on the other hand, refers to the fluid/wall heat transfer. The constitutive relations for these terms will be given in later sections.

Despite its simplicity, the HEM model is most frequently employed in modelling pipe flows (see for example Buaprommart et al., 2019; Chen et al., 1995; Martynov et al., 2014) due to its capability in delivering accurate simulation results with relatively low computational costs.

Comparably, the applications of the HRM, DFM and TFM models in pipe flows are less frequently reported in open literature. Apart from their increased mathematical complexity, they are found to perform just as equally well as the HEM model in the case of pipeline decompression (see for example Brown et al., 2014a, 2013; Munkejord and Hammer, 2015). The mathematical formulations of the HRM, DFM and TFM

model conservation equations are out of the scope of this thesis and their details can be found elsewhere (Bendiksen et al., 1991; Brown et al., 2013; Hibiki and Ishii, 2003).

2.1.2.4 Constitutive Relations

As mentioned above, in modelling pipeline decompression, the volumetric terms in the above conservation equations 2.8 and 2.9 usually include the gravitational force, fluid/wall heat transfer and friction. In the following section, the constitutive relations typically employed for defining these terms are summarised.

2.1.2.4.1 Fluid/wall Friction

The fluid/wall friction force, F_w is usually defined in the below form (Mahgerefteh et al., 1999; Oke et al., 2003):

$$F_w = -\frac{2\rho u|u|f_w}{D_{in}} \quad 2.10$$

where D_{in} is the pipe internal diameter and f_w is the Fanning friction factor.

The Fanning friction factor is typically determined by empirical relations depending on the Reynolds number, Re of the flow.

For laminar pipe flow ($Re < 2300$), the Fanning friction factor is independent of the pipe roughness and can be given by (Rohsenow et al., 1998):

$$f_w = \frac{16}{Re} \quad 2.11$$

For transitional and turbulent flows ($4000 < Re < 4 \times 10^8$) in rough pipes, the Fanning friction factor can be calculated using Chen's correlation (Chen, 1979), given by:

$$\frac{1}{\sqrt{f_w}} = 3.48 - 1.7372 \ln \left(\frac{\varepsilon}{D_{in}/2} - \frac{16.2446}{Re} \ln K \right) \quad 2.12$$

where ε is the pipe wall roughness, and:

$$K = \frac{(\varepsilon/(D_{in}/2))^{1.0198}}{6.0983} + \left(\frac{7.149}{Re} \right)^{0.8981} \quad 2.13$$

For transitional and turbulent flows in smooth pipes, the corresponding Fanning friction factor can be given by (Rohsenow et al., 1998):

$$\frac{1}{\sqrt{f_w}} = 1.7372 \ln \left(\frac{Re}{1.694Re - 3.8215} \right) \quad 2.14$$

2.1.2.4.2 Fluid/wall Heat Transfer

The fluid/wall heat transfer, \dot{Q} is usually modelled based on Newton's cooling law, given by:

$$\dot{Q} = \frac{4}{D_{in}} U (T_w - T_f) \quad 2.15$$

where T_w and T_f respectively represent the pipe wall and fluid temperatures. U on the other hand, denotes the overall heat transfer coefficient.

In modelling the wall temperature during pipeline decompression, the pipe wall density, ρ_w and isobaric specific heat capacity, $C_{p,w}$ are usually assumed to be constant and the wall temperature gradient is usually neglected. Following this, the resulting time-varying wall temperature is given by:

$$C_{P,w}\rho_w \frac{4}{D_{in}} \frac{dT_w}{dt} = \dot{Q}\tilde{A} \quad 2.16$$

where \tilde{A} is the available heat transfer area per unit volume given by:

$$\tilde{A} = \frac{4D_{in}}{D_{ext}^2 - D_{in}^2} \quad 2.17$$

where D_{ext} is the pipe external diameter.

The overall heat transfer coefficient on the other hand is usually determined based on the following empirical correlations.

For forced convection heat transfer, the Dittus-Boelter equation (Green and Southard, 2019) can be adopted:

$$Nu = 0.023Re^{0.8}Pr^{0.4} \quad 2.18$$

where Nu and Pr are respectively the Nusselt number and Prandtl number.

For boiling heat transfer, the most widely used correlation is the Rohsenow correlation (Rohsenow, 1952), given by:

$$\dot{Q} = \mu_l h_{l,l} \left(\frac{g(\rho_l - \rho_g)}{\sigma_l} \right) \left(\frac{C_{P,l}(T_w - T_f)}{0.013h_{l,l}Pr_l^1} \right)^3 \quad 2.19$$

where ρ_l and ρ_g are respectively the densities of the liquid and vapour phases. μ_l , σ_l , $h_{l,l}$, Pr_l and $C_{P,l}$ respectively refer to the viscosity, surface tension, specific latent heat, Prandtl number and isobaric specific heat capacity of the liquid phase. g on the other hand is the gravitational acceleration.

Besides the above, in some engineering practices, the overall heat transfer coefficient can be obtained simply based on expert judgments. For example, 5 W/m^2 is usually recommended for insulated, sub-sea or buried pipelines (Mahgerefteh, 1997).

2.1.2.4.3 Gravitational Force

To describe the fluid flow dynamics for flows in inclined pipes, the gravitational force, F_g needs to be introduced as part of the volumetric terms in the above conservation equations 2.8 and 2.9. Mathematically, the gravitational force is expressed as:

$$F_g = \rho g \sin \theta \quad 2.20$$

where θ refers to the pipe inclination angle relative to the horizontal plane.

2.1.2.5 Physical Properties

2.1.2.5.1 Equation of State

The fluid thermodynamic properties and phase equilibrium data can be computed using an appropriate Equation of State (EoS). In modelling CO_2 pipeline decompression, the Peng-Robinson EoS (PR EoS) (Peng and Robinson, 1976) is the most adopted EoS given its established applicability and high computational efficiency (see for example Teng et al., 2016; Zhao and Li, 2014). Mathematically, it can be expressed as:

$$P = \frac{RT}{V_m - b_p} - \frac{a_p \alpha_p}{V_m^2 + 2b_p V_m - b_p^2} \quad 2.21$$

where V_m denotes the molar volume of the fluid and:

$$\alpha_p = 0.45724 \frac{R^2 T_c^2}{P_c} \quad 2.22$$

$$b_p = 0.07780 \frac{RT_c}{P_c} \quad 2.23$$

$$\alpha_p = \left(1 + (0.37464 + 1.54226\omega - 0.26992\omega^2)(1 - T_r^{0.5})\right)^2 \quad 2.24$$

where R , ω , T_c and P_c are respectively the gas constant, acentric factor, critical temperature, and critical pressure. T_r on the other hand, is defined as:

$$T_r = \frac{T}{T_c} \quad 2.25$$

It should be however noted that the use of PR EoS is not limited to CO₂. Its use can be also extensively found in the case of modelling hydrocarbon pipeline decompression (see for example Mahgerefteh et al., 1999; Oke et al., 2003; Yu et al., 2022).

2.1.2.5.3 Speed of Sound

The local speed of sound, c of the fluid needs to be calculated as part of the thermodynamic properties. For single-phase fluids, the local speed of sound can be determined analytically using:

$$c^2 = \frac{\gamma}{\kappa\rho} \quad 2.26$$

where γ is the ratio of specific heats and κ is the isothermal coefficient of volumetric expansion, given by:

$$\kappa = -\rho \left(\frac{\partial V}{\partial P} \right)_T \quad 2.27$$

For two-phase mixtures, defining γ becomes complicated (Mahgerefteh et al., 1999).

As such, the corresponding speed of sound is evaluated numerically by:

$$c^2 = \frac{\Delta P}{\rho(T, P)_s - \rho(T^*, P - \Delta P)_s} \quad 2.28$$

where the subscript, s denotes the isentropic condition. ΔP on the other hand, is the infinitesimal change in pressure and T^* refers to the corresponding temperature obtained from pressure-entropy flash calculation.

2.1.3 Applications of the HEM Model in Modelling Pipeline Decompression

In the preceding section, the mathematical modelling of multi-phase pipe flows together with the associated constitutive relations and physical property correlations are summarised. In particular, four groups of multi-phase flow models usually applied for pipe flows are discussed, with a focus on the HEM model given its established applicability in pipe flows and relatively low computational demand.

In modelling pipeline decompression, there are generally two types of HEM models based on how their fluid flow dynamics is constructed. The first type, also being the most popular type, is the numerically based models. The numerically based models are considered physically relevant and are therefore widely adopted in academic research. Nevertheless, given that the fluid flow dynamics for this type of models is usually formulated based on the conservation equations of mass, momentum and energy which are a set of coupled and non-linear PDEs, seeking their solutions requires the use of numerical techniques (e.g. finite different method, finite element method) and hence can be computationally demanding.

The second type, often developed to reduce the computational costs associated with the first type of models, is called the analytically based models. In this type, assumptions

are often made to simplify the fluid flow equations to a set of Ordinary Differential Equations (ODEs) to reduce the complexity of the mathematical problem involved and thus improve the computational efficiency. However, given usually the strong assumptions involved, this type of models has limited applicability. Table 2.1 summarises the features and examples of the numerically and analytically based models.

Table 2.1: Summary of the top-level features and examples of the numerically and analytically based models.

Type	Feature	Example
Numerically based model	• PDE-based	Mahgerefteh et al. (1999), Oke et al. (2003), Martynov et al. (2014), Zheng et al. (2017)
	• Physically relevant	
	• High applicability	
	• High computational costs	
Analytically based model	• ODE-based	Norris and Puls (1993), Norris (1994), Webber et al. (1999), Mahgerefteh et al. (2011)
	• Limited applicability	
	• Low computational costs	

In the following section, one typical example for each of the two types of the HEM model in pipeline decompression modelling is reviewed, including their background theory, performance, and computational efficiency.

2.1.3.1 University College London (UCL) Model

The University College London (UCL) model is the most validated among the numerically based models reported in open literature. It was initially developed by Mahgerefteh et al. (1999) for the quantitative failure consequence assessment for the Full Bore Rupture (FBR) failures of pressurised pipelines containing two-phase hydrocarbon mixtures. This was followed by a fundamental extension to accounting for pipeline punctures (Oke et al., 2003). Other important features of this model include the simulations of emergency shut-down valve dynamics (Mahgerefteh et al., 2000,

1997), pipe inclination (Mahgerefteh et al., 2008), pipe networks (Mahgerefteh et al., 2006a), brittle and ductile fractures (Mahgerefteh et al., 2016, 2010), as well as shale gas production well blowout (Buaprommart et al., 2019).

2.1.3.1.1 Theory

The model adopted the HEM assumption (equations 2.7 to 2.9) to describe the fluid flow dynamics. The volumetric terms including the fluid/wall friction and heat transfer were modelled using the standard correlations described in Section 2.1.2.4. The resulting mass, momentum and energy conservation equations can be given by (Mahgerefteh et al., 1999):

$$\frac{\partial \rho}{\partial t} + \frac{\partial}{\partial x} \rho u = 0 \quad 2.29$$

$$\frac{\partial \rho u}{\partial t} + \frac{\partial}{\partial x} (\rho u^2 + P) = \beta_x - \rho g \sin \theta \quad 2.30$$

$$\frac{\partial \rho E}{\partial t} + \frac{\partial}{\partial x} (\rho u E + P u) = \beta_x u - \rho u g \sin \theta + \dot{Q} \quad 2.31$$

where β_x refers to the fluid/wall friction, which was defined by equation 2.10 (see Section 2.1.2.4.1). The fluid/wall Fanning friction factor, f_w was modelled based on the Moody approximation (Massey, 1983) to Colebrooke's equation. To account for real fluid behaviour, the PR EoS (Peng and Robinson, 1976) was adopted to compute the fluid thermodynamic properties and phase equilibrium data. An interpolation grid (Mahgerefteh et al., 2007), serving as a look-up table for computing fluid thermodynamic properties, was employed to reduce the computational runtimes for flash calculations.

2.1.3.1.2 Numerical Method

The above flow equations 2.29 to 2.31 were solved based on the Method of Characteristics (MOC) (Hoffman and Zucrow, 1976). The MOC is based on resolving the system of PDEs into a set of ODEs, also known as compatibility equations, through a particular co-ordinate change. These co-ordinates represent curves (characteristic lines) in the space-time domain along which the compatibility equations hold. The method is well suited to handling fast transient flow where each disturbance is captured along the propagating characteristic lines. The implementation of the MOC for the solution to equations 2.29 to 2.31 is outlined below.

Step 1: Discretisation of the Flow Field

The method of specified time intervals (Flatt, 1986) was first adopted to discretise the flow field. In this method, the location of the solution points in the space-time domain was specified in advance and the characteristic lines were traced backwards in time to their origin in the previous points. A Compound Nested Grid System (CNGS) applying finer numerical grids near the rupture plane where the transients were most rapid was then employed to reduce the computational costs. The schematic representation displaying the CNGS-MOC grid setting employed for the UCL model is presented in figure 2.1.

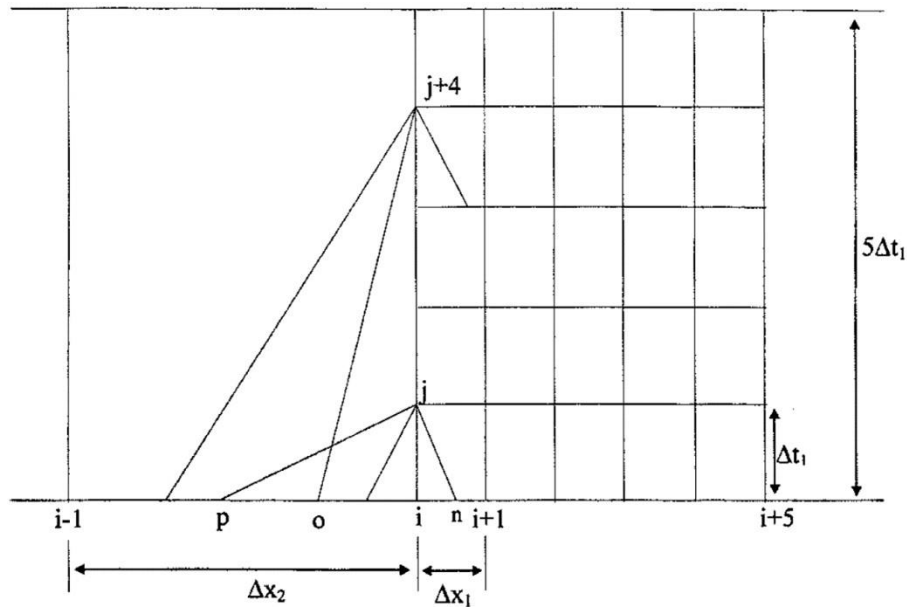


Figure 2.1: Schematic representation of the CNGS-MOC grid setting employed for the UCL model (Mahgerefteh et al., 1999).

Step 2: Conversion of PDEs into ODEs

Equations 2.29 to 2.31 which are a set of PDEs were converted into a set of compatibility equations (ODEs) along three characteristics lines in the space-time domain namely the path line (C_0), positive Mach line (C_+) and negative Mach line (C_-).

The resulting compatibility equations are respectively given by:

Along the path line characteristic:

$$\frac{d_0 P}{d_0 t} - c^2 \frac{d_0 \rho}{d_0 t} = \psi \quad 2.32$$

Along the positive Mach line characteristic:

$$\frac{d_+ P}{d_+ t} + \rho c \frac{d_+ u}{d_+ t} = (\psi + c\beta_x)\beta_x \quad 2.33$$

Along the positive Mach line characteristic:

$$\frac{d_P}{d_t} - \rho c \frac{d_u}{d_t} = (\psi - c\beta_x)\beta_x \quad 2.34$$

where the subscripts, 0, + and – respectively correspond to path line, positive and negative characteristics. ψ on the other hand, is the non-isentropic term incorporating heat exchange and friction. All other symbols have been previously defined in Section 2.1.2.

The positive and negative Mach lines govern the propagating speed of expansion and compression waves, while the path line dictates the flow rate through any given point along the pipe.

Step 3: Solution of Compatibility Equations

As previously mentioned, the solution of the compatibility equations requires the tracing of the characteristic lines in a discretised space-time domain. A schematic representation of these lines in the space-time domain is shown in figure 2.2.

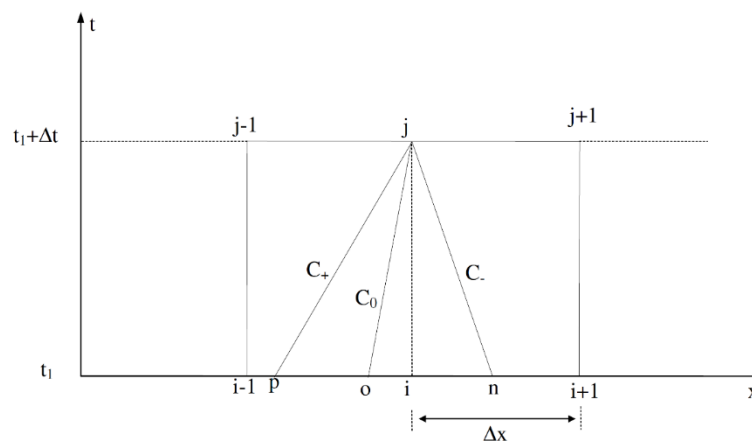


Figure 2.2: Schematic representation of the path line (C_0), positive Mach line (C_+) and negative Mach line (C_-) characteristics at a grid point in the space-time domain (Saha, 1997).

The fluid properties were assumed to be already known at the grid points $i - 1$, i and $i + 1$. The initial conditions at the foot of each characteristic line (i.e. points p , o and n) were evaluated by linear interpolation. The fluid conditions at the solution point, j were then computed by solving compatibility equations 2.32 to 2.34 based on the Euler predictor-corrector finite approximation technique (Hoffman and Zucrow, 1976). This involved transforming these equations into finite difference form using first- and second-order approximations.

In the predictor step, the first-order approximation was employed. The resulting path line, positive Mach line and negative Mach line compatibility equations in the finite difference form are respectively given by:

$$P_j - P_o - c_o^2(\rho_j - \rho_o) = \psi_o(t_j - t_o) \quad 2.35$$

$$P_j - P_p + (\rho c)_p(u_j - u_p) = (\psi + c\beta)_p(t_j - t_p) \quad 2.36$$

$$P_j - P_n - (\rho c)_n(u_j - u_n) = (\psi - c\beta)_n(t_j - t_n) \quad 2.37$$

Solving equations 2.35 to 2.37 simultaneously gave an initial estimation of the solution point pressure, P_j , density, ρ_j and velocity, u_j .

To improve the estimation accuracy, the corrector step involving the second-order approximation was performed. The corresponding compatibility equations along the path line, positive Mach line and negative Mach line characteristics are respectively given by:

$$P_j - P_o - \frac{1}{2}(c_o^2 + c_j^2)(\rho_j - \rho_o) = \frac{1}{2}(\psi_o + \psi_j)(t_j - t_o) \quad 2.38$$

$$\begin{aligned}
 P_j - P_p + \frac{1}{2}((\rho c)_p + (\rho c)_j)(u_j - u_p) \\
 = \frac{1}{2}((\psi + c\beta)_p + (\psi + c\beta)_j)(t_j - t_p)
 \end{aligned}
 \tag{2.39}$$

$$\begin{aligned}
 P_j - P_n + \frac{1}{2}((\rho c)_n + (\rho c)_j)(u_j - u_n) \\
 = \frac{1}{2}((\psi - c\beta)_n + (\psi - c\beta)_j)(t_j - t_n)
 \end{aligned}
 \tag{2.40}$$

Solving equations 2.38 to 2.40 simultaneously, an improved estimation of the pressure, density and velocity at the solution point was obtained. The above estimation process was repeated until a certain tolerance for the results was reached.

To ensure the numerical stability for the above process, the Courant-Friedrich-Lewy criterion (Courant et al., 1928) was satisfied. It is given by:

$$\Delta t \leq \frac{\Delta x}{|u + c|_{max}}
 \tag{2.41}$$

where Δt and Δx are respectively the time and space intervals defining the space-time domain.

2.1.3.1.3 Validation

The UCL model has been validated against the Isle of Grain LPG pipeline decompression tests (Richardson and Saville, 1996). The tests consisted of two parallel 100 m length, 154 mm internal diameter (i.d.) carbon steel pipelines containing commercial LPG (95 mol% propane, 5 mol% n-butane). For both pipelines, the pressure, temperature and inventory mass during decompression were respectively measured using pressure transducers, thermocouples and load cells installed along the pipe.

Two tests, coded as P40 and P45 respectively referring to puncture and FBR failures of

the pipelines, were performed. These tests were initiated by rupture of a disc at the downstream end of the test pipes. A summary of the initial conditions for these tests prior to disc rupture is presented below in table 2.2.

Table 2.2: Initial conditions for Isle of Grain LPG pipeline depressurisation tests P40 and P45 (Richardson and Saville, 1996).

Parameter	P40	P45
Failure mode	154 mm FBR	75 mm puncture
Initial pressure (bar)	21.6	11.4
Initial temperature (°C)	20.0	15.9
Ambient temperature (°C)	19.1	16.7
Wind speed (m/s)	8.8	6.5
Pipe length (m)	100	100
Pipe internal diameter (mm)	154	154
Pipe roughness (mm)	0.05	0.05
Pipe wall thickness (mm)	7.3	7.3

Figures 2.3 and 2.4 show the comparison between the simulated and measured data for pressure- and temperature-time profiles at both the pipe open and intact ends during P40 decompression test. Figure 2.5 on the other hand presents the total line inventory mass profile as a function of time for the same test.

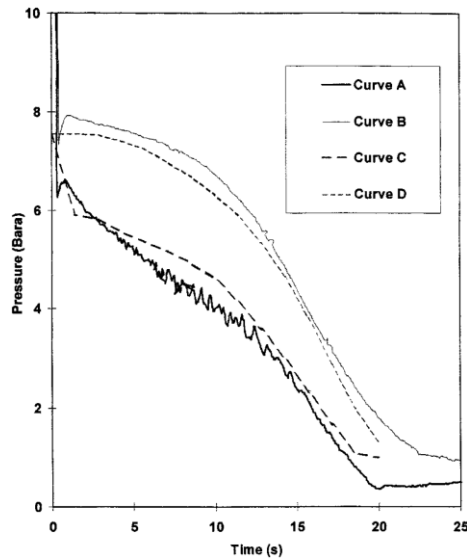


Figure 2.3: Pressure-time profiles at closed and open ends for the Isle of Grain P40 FBR test. Curve A: Field data (open end); Curve B: Field data (closed end); Curve C: UCL model predictions (open end); Curve D: UCL model predictions (closed end). (Mahgerefteh et al., 1999).

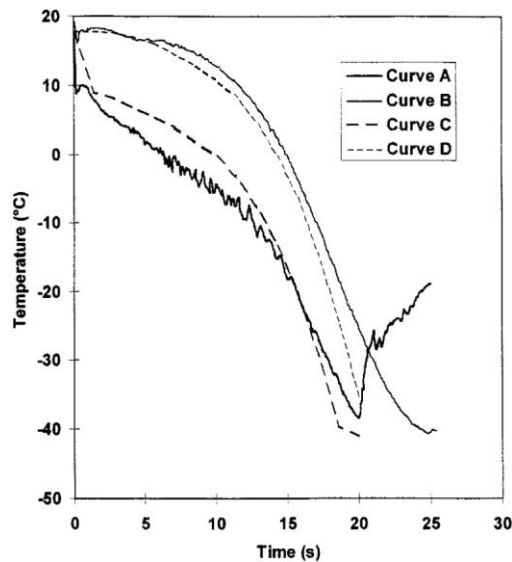


Figure 2.4: Temperature-time profiles at closed and open ends for the Isle of Grain P40 FBR test. Curve A: Field data (open end); Curve B: Field data (closed end); Curve C: UCL model predictions (open end); Curve D: UCL model predictions (closed end). (Mahgerefteh et al., 1999).

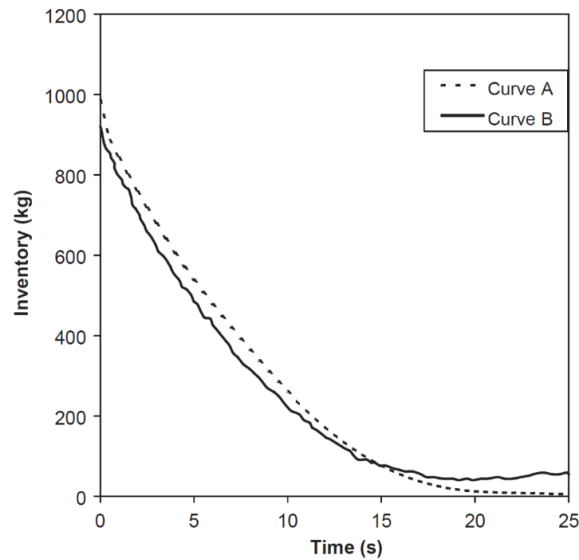


Figure 2.5: Total line inventory mass-time profiles for the Isle of Grain P40 FBR test. Curve A: UCL model predictions; Curve B: Field data. (Oke et al., 2003).

As can be observed from figure 2.3, the simulated pressure profiles in general present close agreement to the measured data at both open and intact ends of the test pipe throughout decompression. The initial sudden pressure drops as a result of the instantaneous phase-transition from liquid to two-phase mixture are accurately predicted. Referring to figure 2.4 for the temperature-time profiles, the experimental data are also well predicted by the model. The maximum discrepancy observed between the measured and predicted temperature is less than ca. 5 °C. With regards to figure 2.5 where the inventory mass-time profiles are presented, the model gives very similar predictions as compared to the experimental data. As expected, the amount of inventory declines monotonically with time.

Turning to test P45 which involves a 75 mm puncture failure (see table 2.2), the corresponding simulated and measured pressure variations as a function of time is shown in figure 2.6.

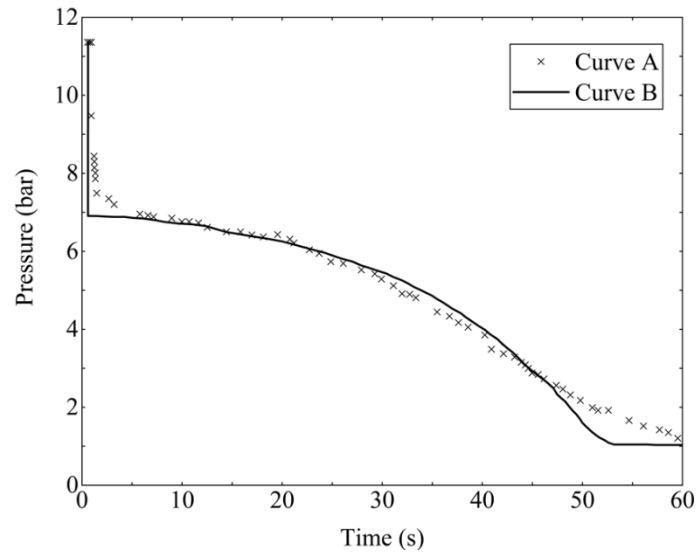


Figure 2.6: Pressure-time profiles for the Isle of Grain P45 puncture test. Curve A: Field data; Curve B: UCL model predictions. (Mahgerefteh et al., 2011).

As may be observed, again, relatively good agreement between the measured and simulated data is evident, well demonstrating the model's capability in simulating puncture failures.

Apart from hydrocarbon pipelines, the UCL model has been also validated against the field data from a series of CO₂ pipeline decompression tests as part of the COOTRANS project undertaken by National Grid UK (Cosham et al., 2012). These tests were carried out for CO₂ and CO₂-rich mixtures in order to understand the decompression wave behaviour in single- and two-phase flows. Among these tests, test 6, which was a pipeline FBR decompression test, consisted of a 144 m length, 150 mm. i.d., 11 mm pipe wall thickness heavily insulated ASTM A333 Grade 6 low carbon steel seamless pipe filled with gaseous mixtures of CO₂, N₂ and SO₂. The pertinent test conditions are summarised in table 2.3.

Table 2.3: Pertinent test conditions for COOTRANS CO₂ pipeline decompression test 6 (Mahgerefteh et al., 2012b).

Feed compositions	Feed temperature (°C)	Feed pressure (bar)	Ambient temperature (°C)
95.97 mol% CO ₂ + 4.03 mol% N ₂	5.3	37.9	20.4

The test pipe was equipped with multiple pressure and temperature transducers along its entire length to monitor transient variations in both parameters. Additionally, by comparing the recorded pressure-time profiles from adjacent pressure transducers (placed at a known distance apart), the decompression wave speed was determined and presented in the form of a fan diagram (a plot of pressure versus decompression wave speed).

Turning to validating the UCL model, the predicted decompression wave speed was compared to the corresponding measurement. The results are presented in figure 2.7.

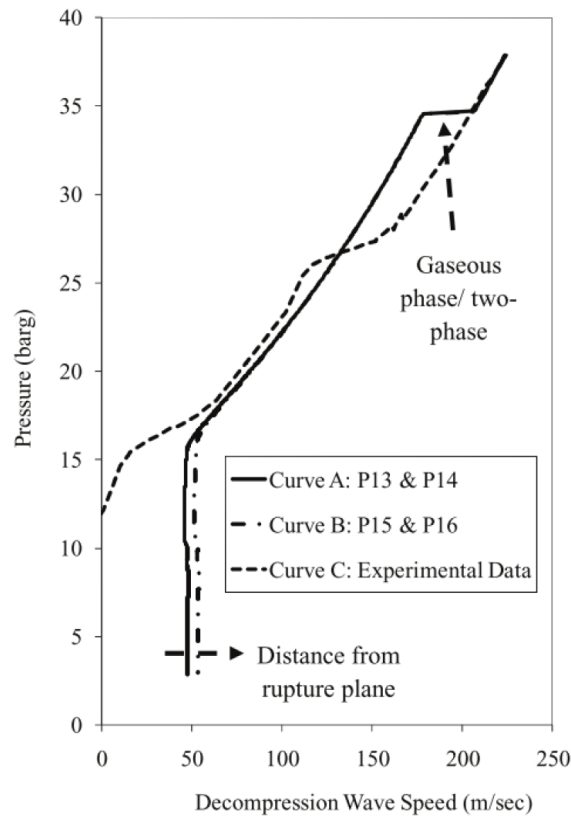


Figure 2.7: Fan diagram at pressure transducers P13 to P16 following FBR for test 6. Curve A and B: UCL model predictions; Curve C: measured data. (Mahgerefteh et al., 2012b).

As can be seen in figure 2.7, a pressure plateau is observed at ca. 34 bar, corresponding to vapour condensation, where the speed of sound, and thus the decompression wave speed, significantly decrease (by ca. 50 m/s in both cases). The wave speed eventually reaches zero when the local flow (between transducers P13 to P16) becomes sonic (choked). With regards to the model performance, the UCL model predictions demonstrate good overall agreement with the data across the testing domain.

In addition to the above, the UCL model has been also successfully validated against other large-scale high-pressure pipeline decompression tests for both CO₂ and hydrocarbons, such as CO₂PipeHaz project (Woolley et al., 2014) and CO₂QUEST project (Brown et al., 2014b), demonstrating broad capabilities.

2.1.3.1.4 Computational Runtimes

Mahgerefteh et al. (1999) performed a study to investigate the computational efficiency of the UCL model. This involved 1) performing simulation tests using three different numerical grid settings, and 2) comparing the corresponding CPU times and simulation accuracies. For the case study, the Piper Alpha tragedy (Cullen, 1990) involving the FBR failure of a 54 km length, 419.1 mm i.d. pipeline transporting natural gas initially at 117 bar and 283 K, was adopted.

Figure 2.8 presents the simulation test results, demonstrating the effect of using different grid settings on the simulation accuracy. Curve A shows the test results using a Simple Grid System (SGS) with a uniform grid size of only 10 m. The SGS employs the finest grid size among the tested grid settings and is therefore taken as a reference for accuracy. Curves B and C on the other hand are the results for the CNGS-MOC grid settings using respectively 500 and 250 m coarse grids. The details of the three tested grid settings and the corresponding test CPU times are summarised in table 2.4. All the simulations were performed using a DEC Alpha server 8400 5/440.

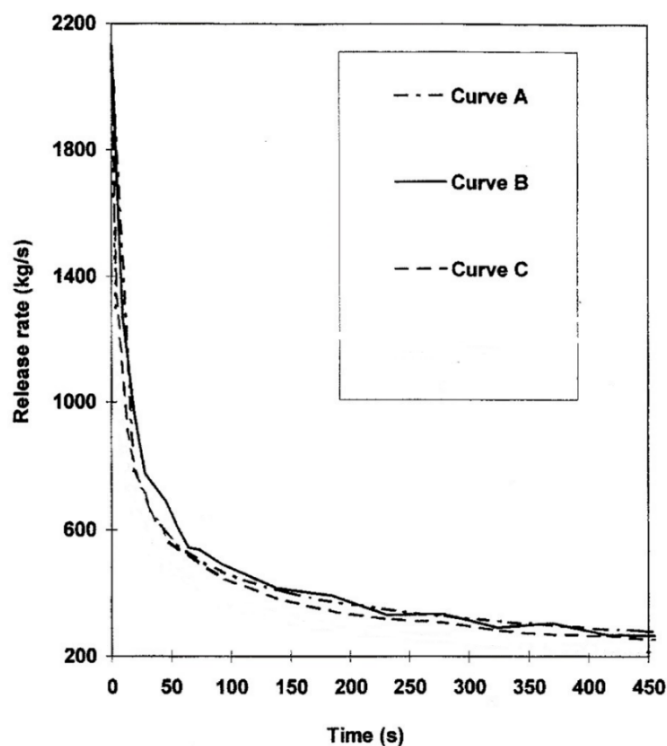


Figure 2.8: Predicted Piper Alpha FBR release rate-time profiles for three tested grid settings. Curve A: SGS (Grid size = 10 m); Curve B: second order CNGS-MOC (Grid size = 500 m); Curve C: second order CNGS-MOC (Grid size = 250 m). (Mahgerefteh et al., 1999).

Table 2.4: Summary of the three tested grid settings and the corresponding test CPU times (Mahgerefteh et al., 1999).

Test no.	Grid settings	CPU time (h)
1	SGS; Uniform grid size = 10 m	250
2	Second order CNGS-MOC; Coarse grid size = 500 m	3.75
3	Second order CNGS-MOC; Coarse grid size = 250 m	12.2

From figure 2.8, it can be observed that both CNGS-MOC settings deliver good agreements with the reference data. Turning to table 2.4, the CPU times for both test 2 (3.75 h) and 3 (12.2 h) adopting the CNGS-MOC grid settings are orders of magnitude lower than that of the reference test (250 h). The level of reduction on the other hand is

dependent on the grid size employed. The above suggests that the use of the UCL model applying the CNGS-MOC solution method can lead to significant CPU time reduction while retaining high-level simulation accuracy. Nevertheless, as the simulated pipeline becomes longer, the CNGS-MOC method unavoidably requires finer numerical discretisation of the flow field to retain simulation accuracy, therefore leading to drastically increased computational runtimes. The above makes the use of the UCL model unattractive in practice especially when multiple simulations may be required or where high-speed data processing computing power may not be readily available.

2.1.3.2 Vessel Blowdown Model (VBM)

The VBM developed by Mahgerefteh et al. (2011) is considered the most recent analytically based model aimed at addressing the issue of long computational runtimes associated with numerically based models. Reconstructing the fluid flow dynamics by assuming a pipeline as a vessel, the model has the capability of delivering exceptionally low computational workloads. In the following, the detailed background theory, verification and computational runtimes of the VBM are reviewed.

2.1.3.2.1 Theory

The VBM approximated the transient outflow from a punctured pipeline as that emanating from a zero-dimensional vessel through an orifice, where the momentum of the fluid upstream the release point was neglected. Hence, in the mathematical formulation of the fluid dynamics, the momentum equation was dropped. Adopting HEM assumption, the corresponding mass and energy conservation equations are respectively written as:

$$\frac{dM}{dt} + G = 0 \quad 2.42$$

$$\frac{1}{2}d(u^2) + gdz + dh = \delta q - \delta W_s \quad 2.43$$

where M , G , u and g are respectively the mass, mass discharge rate, fluid velocity and gravitational acceleration. z , h , q and W_s denote the elevation, fluid specific enthalpy, net heat flux into the pipe and shaft work, respectively.

Neglecting the fluid momentum, however, renders the VBM unable to handle un-isolated release scenarios which are highly plausible in real engineering practices.

To calculate the fluid thermodynamic properties and phase equilibrium data, the PR-EoS (Peng and Robinson, 1976) was adopted. The straw method (Morin et al., 2012) involving establishing an energy balance across the orifice was applied to evaluate the releasing flow conditions.

In solving the fluid flow equations, the following assumptions were made:

- Sufficiently small puncture diameter;
- Constant bulk fluid temperature during decompression
- No initial feed flow;
- Static bulk fluid during decompression;
- Isentropic expansion across the releasing point.

Based on the above assumptions, the simulation of the depressurisation process was then carried out using pressure intervals involving a series of equal pressure reductions.

2.1.3.2.2 Verification

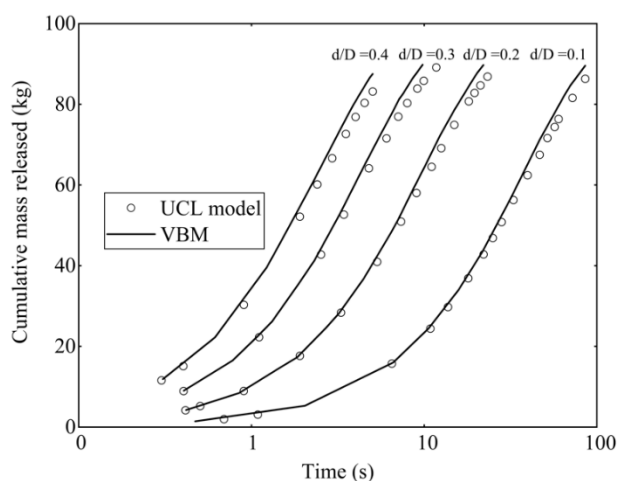
The VBM was verified against the simulation data produced using the extensively

validated numerically based UCL model (see Section 2.1.3.1) based on the failures of a hypothetical pipeline for two types of inventories. These included a permanent gas consisting of 100 mol% methane and a two-phase mixture containing 50 mol% methane and 50 mol% n-pentane. An extensive range of failure cases varying pipe length and puncture to pipe internal diameter ratio, d/D were simulated to provide an in-depth examination of the model performance. The relevant prevailing conditions, pipeline characteristics and the range of parameters used in the verification are presented in table 2.5.

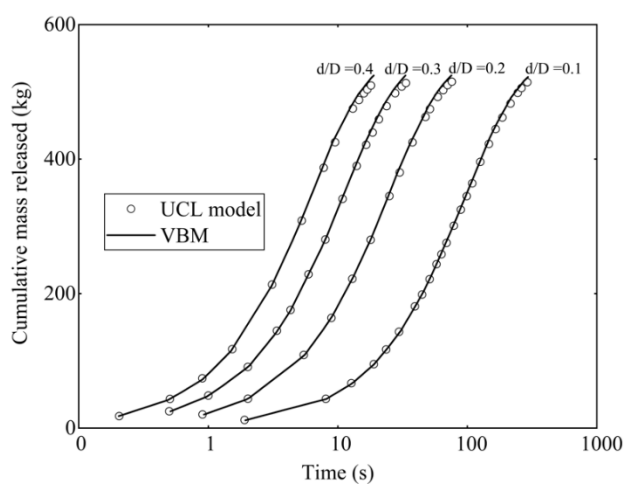
Table 2.5: Prevailing conditions and pipeline characteristics of the hypothetical pipeline failure cases used for the VBM verification (Mahgerefteh et al., 2011).

Parameter	Value
Pipe length (m)	100; 1000; 5000
Pipe internal diameter (mm)	300
Pipe wall thickness (mm)	10
Pipe roughness (m)	0.00005
Pipe wall material	Carbon steel
Initial pressure (bar)	21
Initial temperature (K)	300
Ambient pressure (K)	283
Puncture location	Mid length
Discharge coefficient	1
Puncture to pipe internal diameter ratio, d/D	0.1; 0.2; 0.3; 0.4

Figures 2.9 (a) and (b) respectively show the predicted cumulative mass released-time profiles for the permanent gas and two-phase mixture following puncture with different puncture to pipe internal diameter ratios, d/D ranging from 0.1 to 0.4. The data were produced for a 100 m length pipeline. The dotted lines show the simulated results of the UCL model. The solid lines show those of the VBM.



(a)



(b)

Figure 2.9: Comparison of cumulative mass released-time profiles based on the UCL model (data points) and VBM (solid lines) predictions for different d/D for 100 mol% methane (a) and 50 mol% methane & 50 mol% n-pentane (b) (Mahgerefteh et al., 2011).

As may be observed, for both inventories, the VBM produces excellent agreement with the predictions of the UCL model. The largest discrepancies reported are ca. +4.3% for the permanent gas and +1.5% for the two-phase mixture. The better performance of the VBM in the two-phase mixture may be attributed to its smaller Joule-Thomson expansion coefficient, rendering the isothermal bulk fluid assumption (see Section 2.1.3.2.1) more applicable.

Nevertheless, the authors pointed out that the degree of disagreement between the two models increased with increasing d/D and when the ratio exceeded 0.4, the VBM predictions became notably inaccurate. The authors suggested that this was due to that, when the ratio increased, the static bulk fluid assumption (see Section 2.1.3.2.1) became increasingly inapplicable because of the increased upstream fluid velocity. Ignoring the corresponding upstream kinetic energy was therefore the most likely cause of the observed discrepancy between the predictions of the two models.

2.1.3.2.3 Computational Runtimes

Mahgerefteh et al. (2011) reported the computational runtimes for simulating the complete depressurisation of a pipeline for both UCL model and VBM. Their comparison is given in table 2.6. The results were produced for three different pipe lengths including 100, 1000 and 5000 m (see table 2.5). The selected d/D was 0.4 and all simulations were performed using a 2.66 GHz, 3.0 GB RAM computer.

Table 2.6: Comparison in CPU times between the UCL model and VBM (Mahgerefteh et al., 2011).

Inventory	Pipe length (m)	CPU time	
		UCL model	VBM
100 mol% methane	100	4 min 2 s	0.321 s
	1000	35 min 2 s	0.322 s
	5000	4 h 12 min 33 s	0.320 s
50 mol% methane & 50 mol% n-pentane	100	2 h 15 min 5 s	1.022 s
	1000	5 h 34 min 33 s	1.022 s
	5000	12 h 18 min 33 s	1.019 s

As may be seen, in all tested cases, the computational runtimes for the VBM are orders of magnitude smaller than those for the UCL model. This is due to the fact that the mathematical formulation of the fluid dynamics for the VBM treats the whole pipeline

as a single numerical cell, thereby requiring no numerical discretisation in solving the flow equations as in the UCL model. The number of calculations involved is therefore significantly reduced, resulting in negligible computational runtimes.

2.1.3.3 Concluding Remarks

In the above review, the effectiveness of the numerically and analytically based HEM models and their limitations in simulating pipeline decompression have been demonstrated. Of the two types of solution techniques, the numerically based models are well suited for handling a wide range of failure scenarios such as different failure modes (e.g., FBR, puncture), emergency shut-down valve closure dynamics and pipe elevation. Nevertheless, they have the fundamental drawback of long computational runtimes. In addition, employing iterative methods for evaluating the fluid thermodynamic properties, the numerically based models can become increasingly computationally demanding for simulating long pipelines, especially for multiple simulations or where high-speed data processing computing powers are not readily available. The above makes the use of numerically based models unattractive in practice.

In light of addressing the above issue, several analytically based pipeline decompression models such as Norris and Puls (1993), Norris (1994), Webber et al. (1999) and VBM (Mahgerefteh et al., 2011) whose fluid flow equations are constructed based on ODEs have been developed. Apart from their exceptionally low computational workloads, in some specific cases, they perform equally well as the numerically based models. Despite the above, however, the analytically based models generally have limited applicability due to their pertaining simple assumptions such as constant bulk fluid temperature. As such, further study can be performed to improve their applicability to practical engineering problems.

2.2 Configuring Emergency Shutdown Valves for Pressurised Pipelines

2.2.1 Introduction

As mentioned in Chapter 1, the failure of pressurised pipeline can lead to the release of large amounts of hazardous inventories, posing significant risks to life, environment, and property. To mitigate such risks, inline Emergency Shutdown Valves (ESDVs) are extensively employed as a front-line mitigation tool. Configuring the ESDVs along the pipe length considering their type, number, operational settings and positioning for striking a balance between the risk reduction against valve costs presents significant decision-making challenges. To determine the optimal ESDV configuration, a two-step process first involving performing a Quantitative Risk Assessment (QRA) study for pressurised pipeline and subsequently solving a carefully defined Multi-Objective Optimisation (MOO) problem based on the results of QRA may be adopted.

In light of the above, the following review has been split into three parts. The first part comprises a detailed review of the key building blocks for QRA with a focus on CO₂ pipelines, mainly including the methods for calculating the pipeline failure probability, models typically employed for determining the magnitude of the failure consequences and how the above two are combined to evaluate the risk levels. The second part presents an in-depth description of the background theory of MOO. This part chiefly includes how an MOO problem can be defined and solved according to the subjective preferences of decision makers. Finally, case example studies focusing on the application of MOO in configuring ESDVs and in optimising the design for e.g. the network and compressor of pressurised pipelines are presented.

2.2.2 Quantitative Risk Assessment for Pressurised CO₂ Pipelines

Quantitative Risk Assessment (QRA) is a formal and systematic risk analysis tool to

estimate the likelihood and consequences of hazardous events, and expressing the results quantitatively as risk to people, environment, property or business. QRA also assesses the robustness and validity of quantitative results, by identifying critical assumptions and risk driving elements. QRA studies are typically required for production, processing, transportation, and storage facilities. They contribute to improved decision-making by highlighting the accident scenarios that contribute most to the overall risk. This is carried out in order to demonstrate if the risk acceptability criteria have been met and that the residual risks are as low as reasonably practicable.

A general QRA process (given in figure 2.10) can be summarised as follows.

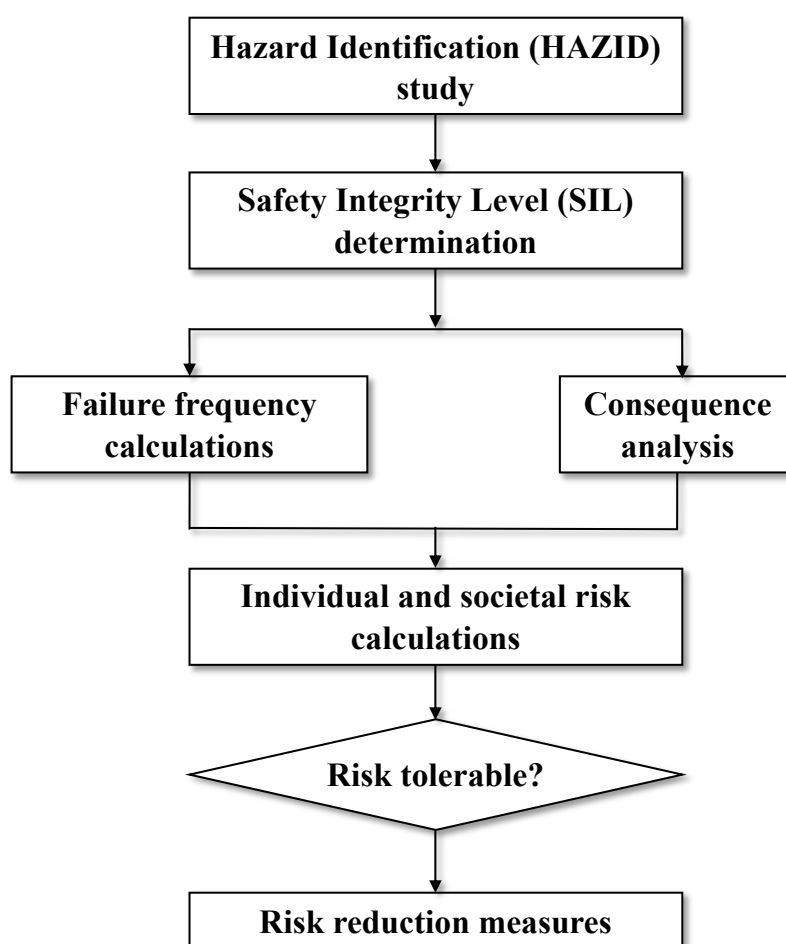


Figure 2.10: A typical QRA process (Smith, 2021).

First, a Hazard Identification (HAZID) study is performed to identify a series of potential hazardous scenarios that could lead to significant adverse consequences. Second, the Safety Integrity Level (SIL) of the facility under consideration is determined using SIL techniques such as calibrated risk graph and layers of protection analysis. These techniques typically involve 1) estimating the frequencies of the identified hazardous scenarios that can lead to loss of containment and 2) calculating the magnitude of the corresponding consequences using relevant consequence models. Third, the calculated frequencies and magnitude of consequences are combined to assess the individual and societal risk levels. Finally, the results are compared with the tolerable risk levels of the decision makers to determine the safe distances and to decide if further safety measures need to be taken.

QRA enables the investigation of possible failure scenarios accounting for their interactions, hence providing an in-depth and systematic understanding of the system failure (Apostolakis, 2004). Nevertheless, lack of data and constraints in data quality, time, personnel, or resources may render QRA unreliable (Coleman and Marks, 1999).

In recent years, the growing uptake of Carbon Capture Utilisation and Storage (CCUS) worldwide has led to the extensive deployment of pressurised CO₂ pipelines. As such, QRA has been extensively applied to improve the safety for their operations (see for example Lisbona et al., 2014; Teng et al., 2021; Vianello et al., 2016). Albeit unlikely, loss of containment events do occur in CO₂ pipelines leading to toxic atmospheric dispersion at concentrations greater than 7% vol/vol, resulting in adverse effects to the population near the failed pipe, such as headache, breathing problems, and even death, depending on the concentration presented and duration of exposure (Rusin and Stolecka, 2015). The use of QRA enables pipeline operators to rationally manage inspection and preventive maintenance and is hence important in allocating risk mitigation resources.

Generally, a reliable QRA for CO₂ pipelines requires 1) a robust model to describe the

CO₂ dispersion process following pipeline failure; 2) the accurate estimation of the pipeline failure frequency and 3) appropriately defined failure scenarios for the subsequent risk evaluation. These points largely form the basis for the accuracy of the risk levels to be assessed and the effectiveness of the subsequent risk mitigation strategies to be implemented.

In view of the above three points, the following section presents a comprehensive review consisting of three parts. The modelling approaches for CO₂ dispersion are briefly summarised in the first part. This is followed by a detailed review of the methods for estimating the pipeline failure frequency, given its direct relevance to the current work. In the last part, an overview for undertaking the subsequent risk evaluation with a focus on defining the failure scenarios is given.

2.2.2.1 Dispersion Modelling

The release of CO₂ from pressurised pipelines produces a gas cloud that is denser than air. The dominant physical effects occurring during the dispersion of the dense gas usually include those (e.g. turbulence damping and gravity spreading) that are not observed in the case of neutrally or positively buoyant gases (Koopman et al., 1989; Markiewicz, 2012). As such, specific models need to be developed to describe the atmospheric dense-gas dispersion.

Generally, four categories of dispersion models with varying physical completeness and mathematical complexity are reported in open literature. These include advanced models, similarity profile models, empirical models, and modified Gaussian plume models. Table 2.7 summarises their top-level features and examples.

Table 2.7: Summary of the top-level features and examples of common categories of dense-gas dispersion model.

Category	Feature	Example
Advanced models	<ol style="list-style-type: none"> 1) Conservation equations treated explicitly in three dimensions; 2) Computationally expensive; 3) Full applicability 	SIGMET (England et al., 1978), CFX (ANSYS, 2011), FLACS (GexCon, 2013)
Similarity profile models	<ol style="list-style-type: none"> 1) Conservation equations simplified by averaging cloud properties over crosswind plane; 2) Computationally efficient; 3) High applicability 	SLAB (Ermak, 1990), SLAM (Ott and Nielsen, 1996), UDM (Witlox and Holt, 1999)
Empirical models	<ol style="list-style-type: none"> 1) Derived based on field test observations; 2) Limited applicability 	McQuaid and Britter (1988), VDI (1990)
Modified Gaussian plume models	<ol style="list-style-type: none"> 1) Modified from the conventional Gaussian plume model for neutrally buoyant gases; 2) Limited applicability 	Burgess and Zabetakis (1973), Clancey (1976)

Among the above dense-gas dispersion models, two similarity profile models including UDM (Witlox and Holt, 1999) and SLAB (Ermak, 1990) are frequently adopted in modelling the dispersion of CO₂ following pipeline failure (see for example Brown et al., 2014c; Dixon et al., 2012; Gant et al., 2014; Papanikolaou et al., 2011; Rusin and Stolecka, 2015; Vianello et al., 2016; Woolley et al., 2014). They are relatively physically complete, computationally efficient, and commercially accessible, hence being capable of delivering reliable QRA within reasonable timeframe.

2.2.2.2 Pipeline Failure Frequency Calculation

The pipeline failure frequency can be defined as the probability of pipeline failure in the unit time following the period of normal functioning of the pipe (Woo, 2020). It usually adopts the unit of the number of failures per year per unit pipe length (Jo and Ahn, 2005). Mathematically, it can be expressed as (Li et al., 2019):

$$\lambda_0(t) = \frac{dP_f(t)}{(1 - P_f(t)) dt} \quad 2.44$$

where, $\lambda_0(t)$ denotes the pipeline failure frequency in times/(km·year). t refers to the working time of the pipeline. $P_f(t)$ on the other hand, is the failure probability of the pipeline of length, L at time t , which is given by:

$$P_f(t) = 1 - e^{-\int_0^t \lambda_0(t) L dt} \quad 2.45$$

Existing methods for estimating the pipeline failure frequency can be generally divided into three categories, namely the historical failure data analysis, structural reliability analysis and expert judgement. Of these methods, the most robust and reliable one is historical failure data analysis. This method, however, requires large datasets of real incidents, which is often practically problematic for pipelines. To address this, one may turn to the other two methods which are both suitable for situations where sufficiently detailed and validated historical failure data are not readily available.

The following presents an elaborated review of the above three methods.

2.2.2.2.1 Historical Failure Data Analysis

Where possible, the most commonly adopted method to estimate the failure frequency

for pressurised pipelines is based on analysing a large number of historical incident data from pipe failure databases. This method involves two major steps.

The first step is to identify a well-established pipeline failure database where the key aspects associated with pipeline failure including the number of incidents, risk exposure mileage and incident-specific information (e.g. failure cause, failure mode, pipe fluid, pipe characteristics) are recorded. Such databases frequently reported in open literature include those by:

- Concawe (Concawe, 2011), EU
- European Gas Pipeline Incident Data Group (EGIG, 2018), EU
- United Kingdom Onshore Pipeline Operator's Association (Lyons et al., 2020), UK
- Pipeline and Hazardous Materials Safety Administration (PHMSA, 2020), US
- National Energy Board (NEB, 2010), Canada
- Transpetro (Alves et al., 2018), Brazil

Other institutions such as PetroChina and Mexican Petroleum Institute have also involved in the development of pipeline incident databases (Wang et al., 2013). But given that as compared to the above, these databases have relatively poor accessibility (some of them are for corporate internal use only), they are in general less popular.

Once an appropriate database is identified, the second step is to compute the pipeline failure frequency by dividing the total number of incidents recorded in the database by the total risk exposure time:

$$\lambda = \frac{\text{Total number of incidents}}{\text{Total risk exposure time}} \quad 2.46$$

However, equation 2.46 only gives the overall pipeline failure frequency. Usually in QRA practices, the failure frequencies for specific pipelines or failure parameters, such as those for a specific failure cause or a pipe section routing through a specific area, are needed. The approach to calculate such failure frequencies is similar as that given by equation 2.46, that is, dividing the number of incidents recorded for the specific parameters of interest by the corresponding risk exposure time data. In practice, the most commonly studied parameter of interest is the cause of pipeline failure, typically categorised into external interference, corrosion, construction defect, ground movement and others/unknown factors (EGIG, 2018). Among these, external interference, also referred to as third-party damage, is observed as the most prevalent cause for holes and ruptures. In contrast, for pinhole/crack leaks which are comparably smaller scale failure modes, corrosion remains the primary cause.

The resulting data of specific parameters can be further processed to derive easy-to-use equations where the specific failure frequency is expressed as a baseline value multiplied by several correction factors accounting for the various aspects associated with pipeline failure (e.g. pipe internal diameter, failure type). The failure frequency can be thus adjusted easily according to the questions at hand. Typical examples of such equations include Thomas (1981), de Stefani and Carr (2010) and Li et al. (2019).

As mentioned above, the validity of the historical failure data analysis method in estimating the pipeline failure frequency largely depends on the number of incidents being recorded. Apart from this, whether the statistics is detailed enough is also crucial, especially when case-specific data are required. It is therefore fundamentally important for the failure statistics collecting bodies to record their data in a detailed manner.

2.2.2.2 Structural Reliability Analysis

The structural reliability analysis method relies on fracture mechanics to determine the pipe wall material's reaction to stresses that are imparted on it. The method usually

involves analysing the mechanism of a hazardous event (e.g. corrosion, excavating machinery) that will threaten the mechanical integrity of the pipe and potentially lead to its failure. A typical process of employing the method to calculate the pipeline failure frequency comprises the following steps (Chaplin, 2015a; Li et al., 2019).

First, well-established statistical models (e.g. normal, Weibull) are applied to capture the randomness of the parameters (e.g. operating pressure, pipe wall thickness, pipe wall material yield strength) that may affect the failure of a pipe. In this step, the probability distribution of each associated parameter is first determined. Second, a limit state function (see for example Chaplin, 2017; Melchers, 2005; Pesinis and Tee, 2017) providing criteria for determining whether the pipe will fail is defined. A limit state function for pipeline failure is usually a mathematical expression used to describe the conditions under which a pipeline transitions from a safe state to a failure state. It typically defines the boundary between acceptable performance and failure by comparing the demand (e.g., applied stress, pressure) with the capacity (e.g., material strength, resistance) of the pipeline based on the hazardous event being studied. Third, Monte Carlo method is adopted to randomly generate a large number of sets of values of the parameters from their corresponding probability distributions. Fourth, each value set which corresponds to a specific failure case is applied to the defined limit state function to examine the state of the pipe (i.e. whether it fails or not) in this specific case. Fifth, the number of cases where the pipe is considered in the state of failure is divided by the total number of Monte Carlo iteration performed to obtain the pipe failure probability. The resulting failure probability is then multiplied with the hazardous event occurrence rate to obtain the pipeline failure frequency.

The above method can be used without any reference to real failure statistic. But its use requires the mathematical modelling of several processes taking place during pipeline failure. The method is hence not suitable for handling cases where the pipe failure mechanisms are not well understood.

2.2.2.2.3 Expert Judgement Method

The expert judgement method, in its literal sense, refers to estimating the pipeline failure frequency based on expert knowledge and experiences. Common methods in this category include the Kent grading method (Muhlbauer, 1996), fault tree analysis (Watson, 1961), analytic hierarchy process (Saaty, 1977), elimination et choice translation reality (Benayoun et al., 1966) and fuzzy comprehensive evaluation based on fuzzy mathematics (Zadeh, 1965).

These methods are essentially a group of decision-making supporting tools usually applied in pipeline QRA to assist the estimation of the pipeline failure frequency. Typical applications in pipeline failure frequency calculation include those by Wang et al. (2008), Yuhua and Datao (2005), Yazdi et al., (2017), Badida et al. (2019), Li et al. (2016), Brito et al. (2010) and Miao and Zhao (2012).

Among these methods, the fault tree analysis is the most extensively adopted one in pipeline QRA. Although there is a vast array of literature on the pipeline failure fault tree, the details of the fault trees produced by different researchers can be different. Even for the same problem, fault trees can differ greatly, hence delivering varied failure frequency calculations.

A common limitation of the expert judgement method is that its use is heavily subjective. As such, to properly use the method takes highly trained personnel, hence limiting its applicability. The method is usually regarded as an alternative in the case of lacking historical failure statistics.

2.2.2.3 Risk Evaluation

Two popular measures to evaluate the risk following pipeline failure are individual risk and societal risk (Uijt de Haag et al., 2001). The former is usually shown on a risk contour plot while the latter is always presented with a Frequency-Number (F-N) curve.

Typical examples of the risk contour plot and F-N curve are respectively shown in figures 2.11 and 2.12.

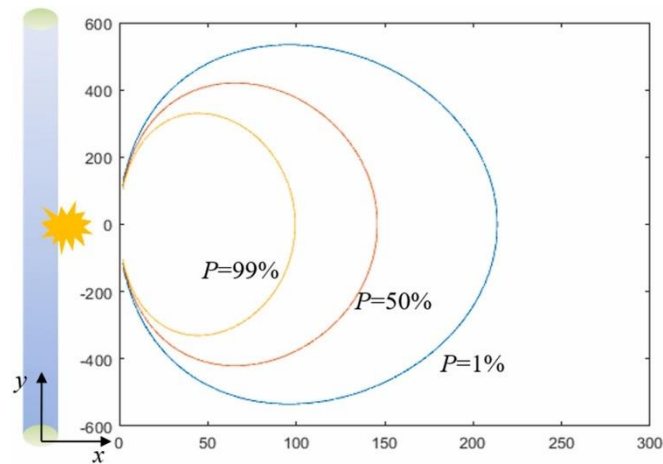


Figure 2.11: An example of the risk contour plot (Teng et al., 2021).

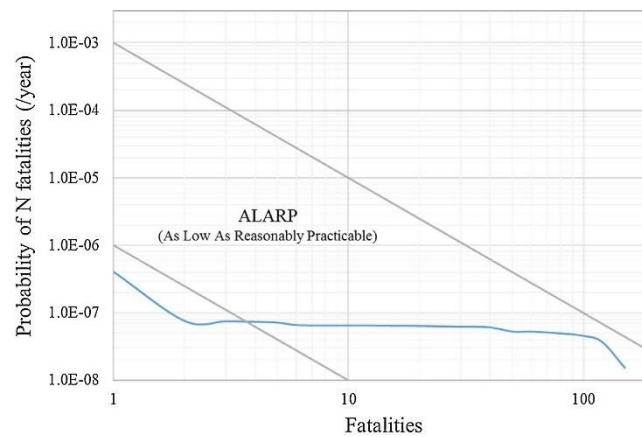


Figure 2.12: An example of the F-N curve (Haszeldine et al., 2010).

2.2.2.3.1 Individual Risk

The individual risk is defined as the probability of a person becoming a fatality (i.e. probability of death) at a given location within a year. It can be estimated by the addition of the failure frequency of a failure scenario multiplied by the corresponding probability of human death for all possible pipe failure scenarios, given by (Jo and Ahn, 2005):

$$IR = \sum_i \lambda_i P_{d,i} \quad 2.47$$

where IR refers to the individual risk. The subscript, i on the other hand denotes the failure scenarios. λ_i and $P_{d,i}$ are respectively the overall pipeline failure frequency and probability of death for failure scenario, i .

The failure frequency is usually determined using the methods reviewed in Section 2.2.2.2. For CO₂ pipelines, despite the fact that their number of incidents are small due to the relatively shorter operational experience as compared to hydrocarbon pipelines (Gale and Davison, 2004), their failure frequencies are usually calculated based on historical failure data analysis where a large number of real incident data are required (see Section 2.2.2.2.1). The failure statistics for CO₂ pipelines however is often not used directly to perform the analysis. Instead, in many studies, those of natural gas pipelines are adopted as a proxy (Duncan and Wang, 2014b). The reason for such an analogy between CO₂ and natural gas pipelines is mainly based on the fact that they both:

- 1) use the same grade of carbon steels (typically API 5 X55 to X70 or higher) as pipe wall materials (Spinelli and Prandi, 2012);
- 2) are welded and installed using the same techniques (Akselsen et al., 2010);
- 3) use similar internal and external coatings (Sørensen et al., 2009);
- 4) are subject to the same corrosion issues involving the formation of carbonic and other acid (e.g. sulfuric, nitric) due to the presence of water and other acid forming impurities such as H₂S, NO₂ (Sim et al., 2014);
- 5) use the same cathodic protection for external corrosion mitigation.

The probability of death corresponding to a given failure scenario is usually obtained

using the Probit function, which defines the relationship between the consequence of a failure scenario and the corresponding lethality taking into account the human exposure duration (Koorneef et al., 2009). The use of the Profit function varies depending on the type of fluid being transported in the pipe and how in the event of pipeline failure, the escaping material will cause fatalities. In the case of CO₂ pipeline failure, the fatality is usually the result of people being exposed to high-concentration CO₂ in the surrounding air (Mahgerefteh et al., 2012b; Martynov et al., 2013; Woolley et al., 2014). The corresponding Probit function is hence linked to the CO₂ concentration and may take the form (McGillivray and Wilday, 2009):

$$P_r = -90.80 + 1.01 \ln(C^8 t) \quad 2.48$$

where P_r refers to the Probit value. C is the CO₂ concentration which can be obtained from the dispersion models reviewed in Section 2.2.2.1. t , on the other hand, is the human exposure time. Once the Probit value is obtained, the probability of death for a given failure scenario, $P_{d,i}$ can then be determined using the curve shown below (figure 2.13).

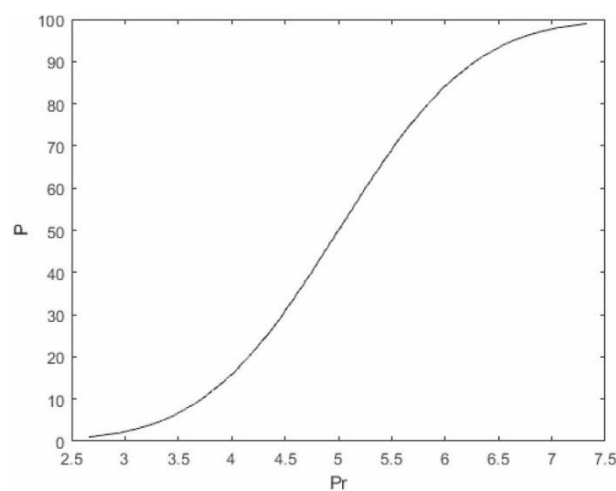


Figure 2.13: Relationship between the Probit value and probability of death (Teng et al., 2021).

For computational purposes, the use of the curve in figure 2.12 is not convenient. Hence, an analytical expression for the curve can be adopted (Crowl and Louvar, 2011):

$$P_{d,i} = \frac{1}{\sqrt{2\pi}} \int_{-\infty}^{Pr^{-5}} e^{-\frac{x^2}{2}} dx \quad 2.49$$

2.2.2.3.2 Societal Risk

In comparison to the individual risk, the societal risk is defined from the societal point of view. It concerns the number of fatalities in a given populated area following an incident. It is often expressed in the form of a F-N curve where the cumulative failure frequency of the failure scenario with N or more fatalities is plotted against N .

The number of fatalities for a given failure scenario, N_i is usually calculated by integrating the product of probability of death and population density over the area affected by pipeline failure, given by (Jo and Ahn, 2005):

$$N_i = \int_{A_i} \rho_p P_{d,i} dA_i \quad 2.50$$

where, ρ_p is the population density and A_i is the affected area.

The cumulative failure frequency on the other hand is determined by:

$$F_c = \sum_i \lambda_i u(N_i \geq N) \quad 2.51$$

where, F_c represents the cumulative failure frequency of the failure scenario with N or more fatalities. $u(N_i \geq N)$ is the unit function which is equal to 1 if N_i is greater than N and 0 if otherwise.

The societal risk is considered more important than the individual risk (Jo and Ahn,

2005). Many regulative requirements for risk acceptability criteria are expressed in the form of societal risk (F-N curve). A typical example is illustrated in figure 2.14.

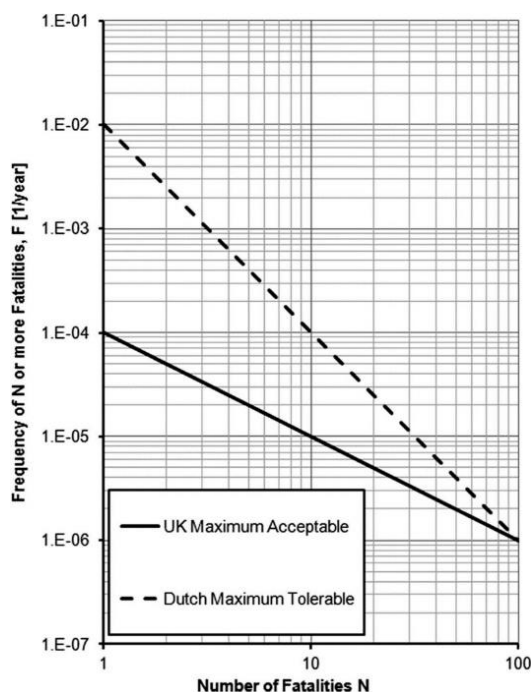


Figure 2.14: Typical F-N curve and UK/Dutch societal risk criteria for a process facility (Neunert and Kaufmann, 2012).

As may be observed from figure 2.14, the societal risk can be ‘acceptable’, ‘intolerable’ or ‘tolerable but not acceptable’, depending on the regulative requirement. In the latter case, the risk needs to be mitigated according to the as low as reasonably practicable principle, that is, the cost involved in reducing the risk further would be grossly disproportionate to the benefit gained.

2.2.2.3.2 Defining Failure Scenarios

A major challenge facing the risk evaluation for pipeline QRA is defining the failure scenarios following pipeline failure. Many associated parameters such as the hole size on the pipe, meteorological conditions etc. may vary greatly at the time of pipeline failure, leading to different possible failure scenarios (Jo and Ahn, 2005). Whether all

these scenarios are reasonably covered in the risk evaluation process is hence fundamentally important for the reliability of QRA.

Key to the above is that the randomness of the associated parameters is properly modelled, which requires the use of well-established probability distribution models. Below reviews some of the most used ones.

Normal Distribution

The normal distribution, also known as the Gaussian distribution, is a type of continuous distribution for a real-valued random variable, $x \in \mathbb{R}$. It is usually denoted by $N(\mu, \sigma^2)$. The general form of its Probability Density Function (PDF) and Cumulative Distribution Function (CDF) are respectively given by (Ahsanullah et al., 2014):

$$f(x) = \frac{1}{\sigma\sqrt{2\pi}} e^{-\frac{1}{2}\left(\frac{x-\mu}{\sigma}\right)^2} \quad 2.52$$

$$F(x) = \frac{1}{2} + \frac{1}{2} \operatorname{erf}\left(\frac{x-\mu}{\sqrt{2}\sigma}\right) \quad 2.53$$

where $f(x)$ and $F(x)$ respectively denote the PDF and CDF. μ and σ on the other hand are respectively the mean and standard deviation of the distribution. erf refers to the error function which is given by:

$$\operatorname{erf}(x) = \frac{2}{\sqrt{\pi}} \int_0^x e^{-t^2} dt \quad 2.54$$

The graph of the PDF of normal distribution is a symmetric and bell-shaped curve. The normal distribution is suited for modelling parameters whose values are practically default but with certain levels of variations, such as the pipe internal pressure, internal

diameter, or wall thickness (Chaplin, 2015a).

Weibull Distribution

The Weibull distribution (Weibull, 1951), denoted by $\text{Wei}(\alpha, \beta)$, is a continuous probability distribution for a random variable, $x \in [0, +\infty)$. It is commonly used to model failure in engineering applications. Its PDF and CDF respectively take the form (Rinne, 2008):

$$f(x) = \begin{cases} \frac{\beta}{\alpha} \left(\frac{x}{\alpha}\right)^{\beta-1} e^{-\left(\frac{x}{\alpha}\right)^\beta} & x \geq 0 \\ 0 & x < 0 \end{cases} \quad 2.55$$

$$F(x) = \begin{cases} 1 - e^{-\left(\frac{x}{\alpha}\right)^\beta} & x \geq 0 \\ 0 & x < 0 \end{cases} \quad 2.56$$

where α is the scale parameter that stretches or squeezes the Weibull distribution graph and β is the shape parameter that determines the general shape of the graph.

Unlike the normal distribution whose graph is symmetric, the Weibull distribution is quite flexible and can be used to model both left- and right-skewed data. The Weibull distribution has been used to model the probability distribution of the defect length on pipe walls in many studies (see for example Chaplin, 2015b; Goodfellow et al., 2012).

Lognormal Distribution

The lognormal distribution, usually denoted by $\ln N(\mu, \sigma^2)$, is a continuous probability distribution for a random variable, $x \in (0, +\infty)$ whose logarithm is normally distributed. Its PDF and CDF can be respectively written as (Kissell and Poserina, 2017):

$$f(x) = \frac{1}{\sigma\sqrt{2\pi}x} e^{-\frac{1}{2}\left(\frac{\ln x - \mu}{\sigma}\right)^2} \quad 2.57$$

$$F(x) = \frac{1}{2} + \frac{1}{2} \operatorname{erf}\left(\frac{\ln x - \mu}{\sigma\sqrt{2}}\right) \quad 2.58$$

Similar as the Weibull distribution, the lognormal distribution has high flexibility, thus capable of handling both left- and right-skewed data. The lognormal distribution has been used to represent the probability distribution of the yield stress of the pipe wall material in the HSE's PIPIN code for determining the failure frequencies of major hazard pipelines (Chaplin, 2015a).

Continuous Uniform Distribution

The continuous uniform distribution, or rectangular distribution describes a function where a continuous random variable, x has an equal probability of occurrence within a certain boundary whose lower and upper limits are usually defined respectively by parameters, a and b . The distribution is often denoted by $U(a, b)$ and its PDF and CDF respectively take the form (Jabeen and Zaka, 2020):

$$f(x) = \begin{cases} \frac{1}{b-a} & a \leq x \leq b \\ 0 & \text{otherwise} \end{cases} \quad 2.59$$

$$F(x) = \begin{cases} 0 & x < a \\ \frac{x-a}{b-a} & a \leq x \leq b \\ 1 & x > b \end{cases} \quad 2.60$$

The continuous uniform distribution is a family of symmetric probability distributions whose graphs are symmetric curves. In studying pipeline failures, variables which have

an infinite number of equally likely values such as the pipe failure location can be described using the continuous uniform distribution.

2.2.3 Multi-Objective Optimisation

The optimal solution to a problem can be found via an optimisation process using one or more objectives (Gunantara, 2018). Optimisation processes involving finding the optimal solution values of more than one desired objective are referred to as Multi-Objective Optimisation (MOO). In solving MOO problems, the objectives are often conflicting. Therefore, the solutions to the problems are usually sought in the presence of trade-offs between some contradictory issues. In MOO, there is usually no single best solution for all objectives, but rather several solutions. Most real-world optimisation problems in mathematics, science or engineering are multi-objective, involving multiple criteria to be considered simultaneously (Bechikh et al., 2015).

MOO technique has found extensive applications in investigating pipeline failures, mainly focusing on the reliability-based and risk-informed design, operation, maintenance, and regulation of pipe systems (Yu, 2021). Few of such studies, however, can be found for CO₂ pipelines despite the significantly growing interest in them as part of the CCUS chain.

In the following section, a review of the fundamental theory of the MOO technique is presented, with a focus on how an MOO problem can be formulated and solved.

2.2.3.1 Mathematical Formulation of an MOO Problem

Mathematically, an MOO problem can be defined as (Coello et al., 2007):

$$\text{Min/Max } \mathbf{f}(\mathbf{x}) = \begin{bmatrix} f_1(\mathbf{x}) \\ f_2(\mathbf{x}) \\ \vdots \\ f_i(\mathbf{x}) \\ \vdots \\ f_n(\mathbf{x}) \end{bmatrix} \quad 2.61$$

where, n is the number of objectives reflected in the n objective functions in the MOO problem being solved. $f_i(\mathbf{x})$ is the i^{th} objective function and $\mathbf{f}(\mathbf{x})$ is the vector function formed by the n objective functions. \mathbf{x} on the other hand, is the vector of optimisation variables, which is given by:

$$\mathbf{x} = \begin{bmatrix} x_1 \\ x_2 \\ \vdots \\ x_j \\ \vdots \\ x_k \end{bmatrix} \quad 2.62$$

Subject to: $x_j \in \Omega$

where, k is the number of optimisation variables being considered in the MOO problem and x_j denotes the j^{th} optimisation variable. Ω on the other hand, corresponds to the universe of the optimisation variable, x_j .

In most MOO problems, there are always restrictions imposed (e.g., physical limitations, time restrictions, etc.) in order to consider a certain solution acceptable. All these restrictions in general are referred to as constraints. These constraints are usually expressed in the form of either mathematical inequalities (Coello et al., 2007):

$$g_i(\mathbf{x}) \leq 0 \quad i = 1, 2, \dots, m \quad 2.63$$

or equalities:

$$h_j(\mathbf{x}) = 0 \quad j = 1, 2, \dots, p \quad 2.64$$

where m and p are respectively the numbers of inequality and equality constraints. Note that p must be less than the number of optimisation variables, k , because if $p \geq k$, there are no degrees of freedom left to be optimised and the problem is said to be over-constrained.

2.2.3.2 Solution Methods

As mentioned above, given the conflicting nature of the objective functions, there is no single solution to an MOO problem that is optimal with respect to all objectives simultaneously, but rather many different solutions which are optimal may exist. The solution methods of an MOO problem can be generally divided into three groups based on when the decision makers provide their preferences, including (Coello et al., 2007):

- 1) non-interactive methods where the preference information is given before the optimisation process (*a priori* articulation of preferences);
- 2) generating methods where the preference information is given after the optimisation process (*a posteriori* articulation of preferences);
- 3) interactive methods where the preference information is given during the optimisation process (progressive articulation of preferences).

A detailed review of these solution methods is given below.

2.2.3.2.1 Non-interactive Methods

The idea behind the non-interactive methods is to make the MOO problem create a single solution by assigning the decision makers' preference information *a priori*, i.e.

before the results of the optimisation process are known. The preference information is thus integrated into the mathematical formulation of the MOO problem itself. Many approaches have been developed for the above purpose. The major ones include weighing the objective functions (Yang, 1996), changing the dominance definition (Molina et al., 2009), formulating a utility function (Malakooti, 1988), and ranking the objective functions by priorities (Yang, 2000).

Among these approaches, the most widely reported in the open literature is weighing the objective functions (de Weck, 2004), where the MOO problem is solved by translating it back to a single objective problem by aggregating all the objective functions being considered in the problem based on the weights assigned to them before the optimisation process. The resulting aggregated objective function can be expressed as (Murata et al., 1996):

$$f_a(\mathbf{x}) = \sum_{i=1}^n w_i f_i(\mathbf{x}) \quad 2.65$$

where $f_a(\mathbf{x})$ denotes the aggregated function. w_i on the other hand, is the weight assigned to objective function $f_i(\mathbf{x})$. The weight of an objective function will determine the solution to $f_a(\mathbf{x})$ and shows the performance priority (Dodgson et al., 2009). Objective functions that are assigned with larger weights have higher priorities. In general, there are three approaches to assign the weights, namely the equal weighing, Rank Order Centroid (ROC) weighing and Rank Sum (RS) weighing (Jia et al., 1998).

Equal weighing, in its literal sense, means that the weights are assigned equally between objective functions. Mathematically, it can be expressed as (Dawes and Corrigan, 1974):

$$w_i = \frac{1}{n} \quad 2.66$$

ROC weighing on the other hand, is normally used in the situation where the rank order of the true weights is known but no other quantitative information between the weights is further given. This approach assumes that the weights are uniformly distributed on the simplex of rank order weights, $w_1 \geq w_2 \geq \dots \geq w_n \geq 0$ where $\sum_i w_i = 1$, and are hence calculated using (Barron and Barrett, 1996):

$$w_i = \frac{1}{n} \sum_{k=1}^n \frac{1}{k} \quad 2.67$$

RS weighing is adopted when the quantitative information about the weights is known. Accordingly, it puts each objective in a proportional position and the corresponding weight is calculated using (Einhorn and McCoach, 1977):

$$w_i = \frac{2(n+1-i)}{n(n+1)} \quad 2.68$$

The interactive methods are considered relatively simple but a major limitation of theirs is that the decision makers do not necessarily know the possibility of the problem, thus leading to inaccurate or even misleading results (Corne and Knowles, 2007).

2.2.3.2.2 *Generating Methods*

In contrast to the interactive methods, the generating methods do not require prior preference information from the decision makers. Instead, the preference is given *a posteriori* i.e. after the feasible solutions to the MOO problem are generated.

This group of methods keeps the elements of the solution vectors independent during the optimisation process and will consequently give multiple feasible solutions. These solutions are usually plotted in the space of objective functions and are usually differentiated using the concept of dominance (Gunantara, 2018). Dominance is defined

as follows (Bechikh et al., 2015; de Weck, 2004):

Let $\mathbf{u} = (u_1, u_2, \dots, u_n)$ and $\mathbf{v} = (v_1, v_2, \dots, v_n)$ be two vectors and \mathbf{u} is said to dominate \mathbf{v} if and only if:

$$\mathbf{u} \preceq \mathbf{v} \quad 2.69$$

if the MOO problem involved is minimisation and:

$$\mathbf{u} \succeq \mathbf{v} \quad 2.70$$

if the MOO problem involved is maximisation.

where the symbols \preceq and \succeq respectively denote ‘partially smaller and greater than’.

In other words, \preceq means $\forall m \in \{1, 2, \dots, M\} u_m \leq v_m$ and $\exists m \in \{1, 2, \dots, M\}$ where $u_m < v_m$. Conversely, \succeq means $\forall m \in \{1, 2, \dots, M\} u_m \geq v_m$ and $\exists m \in \{1, 2, \dots, M\}$ where $u_m > v_m$.

Following the above definition, a solution is considered dominated if in the objective space, there exists another solution whose objective function dominates that of the said solution. If otherwise, the solution is non-dominated. The non-dominated solutions are achieved when improving one objective function can only be done by compromising at least another one, hence presenting the optimal trade-offs between the different objectives. These solutions are also called Pareto optimal solutions.

In mathematical terms, a solution $\mathbf{x} \in \Omega$ is said to be Pareto optimal with reference to Ω if and only if there exists no other solution $\mathbf{x}' \in \Omega$ for which $\mathbf{f}(\mathbf{x}')$ dominates $\mathbf{f}(\mathbf{x})$.

The collection of Pareto optimal solutions is called Pareto set which is mathematically

defined as:

$$\mathcal{P}^* := \{x \in \Omega \mid \neg \exists x' \in \Omega \ f(x') \leq f(x)\} \quad 2.71$$

where \mathcal{P}^* denotes the Pareto set.

When plotted in the objective space, the set of Pareto optimal solutions is collectively referred to as the Pareto front. Mathematically, the Pareto front can be defined as:

$$\mathcal{PF}^* := \{f(x) \mid x \in \mathcal{P}^*\} \quad 2.72$$

where \mathcal{PF}^* denotes the Pareto front.

Once the set of Pareto optimal solutions is obtained, preference criteria of the decision makers can be imposed to generate the region of interest on the Pareto front, which essentially represents the set of optimal solutions preferred by the decision makers.

An illustration of a typical solution space using the generating methods based on two objective functions (two-dimensional) is demonstrated in figure 2.15, showing the Pareto front and dominated & non-dominated (Pareto optimal) solutions. Also presented in the figure is the Utopia point which is an infeasible solution point that optimises all the objective functions individually.

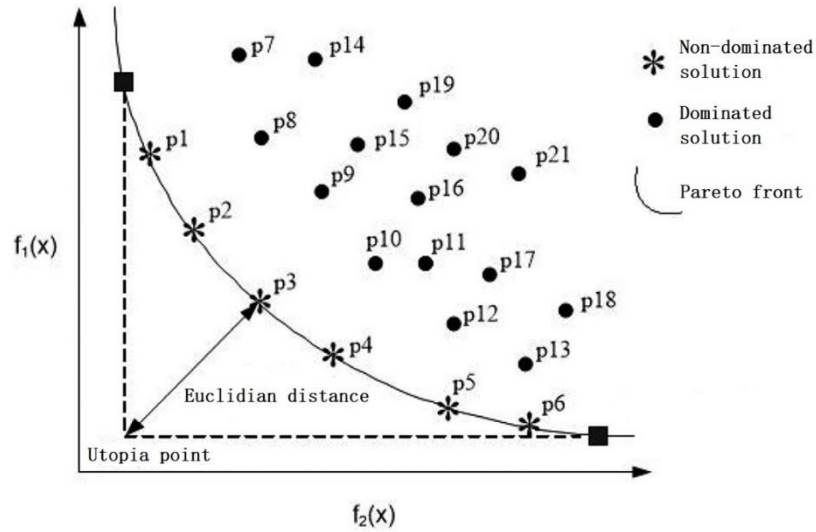


Figure 2.15: Illustration of Pareto front for two objective functions (Gunantara, 2018).

Mathematically, the Utopia point, denoted by $z^U = (z_1^U, z_2^U, \dots, z_i^U, \dots, z_n^U)$, is expressed as:

$$z_i^U = \min_{x \in \Omega} f_i(x) \quad i = 1, 2, \dots, n \quad 2.73$$

The Utopia point can be used for locating the optimal solution on the Pareto front if no region of interest is designated. This is usually done by finding the point on the Pareto front that is closest to the Utopia point in the Euclidian-distance sense (Ozçelebi, 2006).

The main goal of the generating methods is to find the Pareto front or a well-converged and well-distributed approximation of it from which the decision makers can select the optimal solution based on their subjective preferences. Using this group of methods, the decision makers usually have a clearer understanding of the trade-offs between the objectives. Nevertheless, as the objectives number increases, solving the corresponding MOO problem can be increasingly computationally expensive (Khare et al., 2003). Typically, most of the evolutionary MOO algorithms belong to this group (Yu, 2021).

2.2.3.2.3 Interactive Methods

Methods where the preference information is expressed during the optimisation process represent a third, albeit less well-developed group. In this group of methods, the decision makers are able to participate and direct the optimisation process by modifying their preferences based on the domain knowledge acquired. These methods usually operate in the following three stages: 1) finding a non-dominated solution; 2) getting the reaction of decision makers regarding this non-dominated solution and modifying the preferences of the objectives, accordingly; 3) repeating steps 1) and 2) until the decision makers are satisfied or no further improvement is possible.

In comparison with the non-interactive and generating methods, the interactive methods are in general less computationally demanding as only those Pareto optimal solutions that the decision makers are interested in are generated during the optimisation process (Wang et al., 2017). Typical examples of this group include the probabilistic trade-off development method (Goicoechea et al., 1979a), STEP method (Goicoechea et al., 1979b), and sequential multi-objective problem solving method (Monarchi et al., 1973).

2.2.4 Applications of MOO for Pressurised Pipelines

In the preceding sections, comprehensive reviews focusing on 1) the key building blocks for CO₂ pipeline QRA and 2) the mathematical formulation & solution methods of an MOO problem are presented. In the following section, selected examples for the applications of MOO in configuring ESDVs and for optimising the design for pressurised pipeline are reviewed and discussed.

2.2.4.1 Brown et al. (2014c)

Brown et al. (2014c) proposed an MOO methodology for optimising the ESDV spacing for CO₂ pipelines as a trade-off between the risk reduction against the valve installation and maintenance costs. Mathematically, the MOO problem is summarised as:

$$\text{Min}_{d \in D} J_1(d), J_2(d) \quad 2.74$$

where, d refers to the ESDV spacing. $J_1(d)$ is the objective function for the risk associated with a pipeline failure, and $J_2(d)$ on the other hand is the objective functions defined for the valve installation and maintenance costs.

In defining $J_1(d)$, the failure scenario was assumed to be the FBR of a hypothetical 96 km length, 571.2 mm i.d. pipeline transporting dense-phase CO₂ initially at 151 bar and 303 K. Other pipeline characteristics and fluid conditions are summarised in table 2.8. To obtain the FBR failure consequences, the pipeline decompression model developed by Mahgerefteh et al. (1999) coupled with the SLAB model (Ermak, 1990) for dense-gas dispersion was employed. $J_1(d)$ was then defined as the area bounded by the 7% vol/vol concentration contour of the dispersing CO₂.

Table 2.8: Pipeline characteristics and fluid conditions for the FBR failure scenario (Brown et al., 2014c).

Parameter	Value
Pipe external diameter (mm)	610
Pipe wall thickness (mm)	19.4
Pipe wall roughness (mm)	0.005
Pipe length (km)	96
Pipe angle	Horizontal
Pipe upstream condition	Reservoir (Constant pressure)
Pipe downstream condition	No back flow
Feed pressure (bar)	151
Feed temperature (K)	303
Ambient temperature (K)	283

$J_2(d)$ on the other hand, was calculated using the following equation (Seider et al., 2004):

$$J_2(d) = \frac{V_{PN} r_d (1 + r_d)^{yr} L}{((1 + r_d)^{yr+1}) d} \quad 2.75$$

where, V_{PN} is the present net value of a single ESDV cost. r_d is the discount rate. yr is the average lifetime of the ESDV and L is the overall length of the pipe.

To solve the MOO problem described above, 30 different ESDV spacings, ranging from 5 to 40 km were sampled. The ESDVs were assumed to close 900 s following pipeline failure at a rate of 1.904 cm/s. The values used for $J_2(d)$ were respectively $V_{PN} = 15,556$ €, $r_d = 0.035$ and $yr = 10$, following Medina et al. (2012).

Figure 2.16 shows the variation of the shape of the 7% vol/vol CO_2 concentration contour with time following pipeline failure. Figure 2.17 on the other hand presents the Pareto front of the MOO problem showing the variation of normalised risk, J_1 as a function of normalised ESDV costs, J_2 .

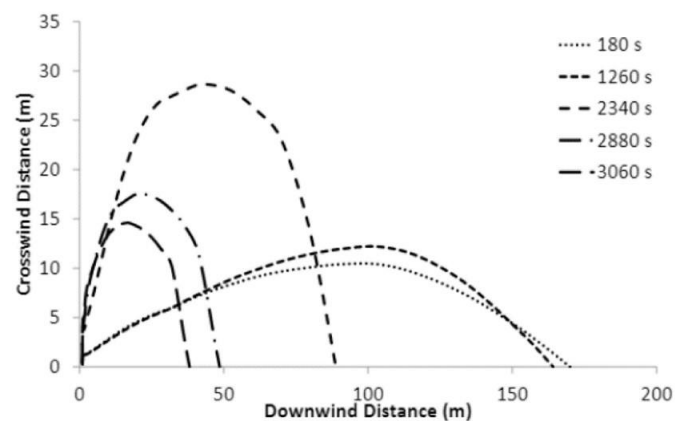


Figure 2.16: Variation of the shape of the 7% vol/vol CO_2 concentration contour with time following pipeline failure (Brown et al., 2014c).

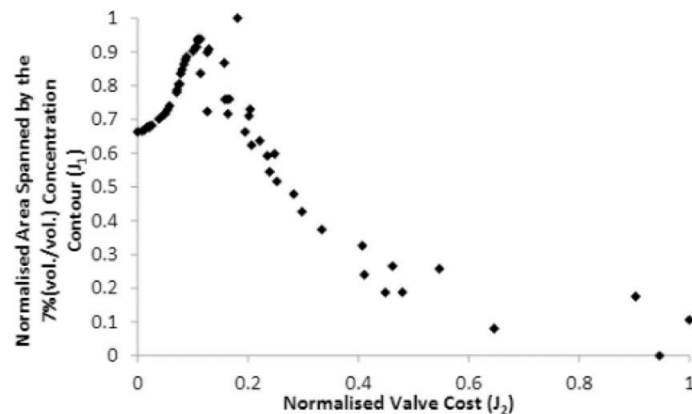


Figure 2.17: Pareto front of the MOO problem showing the variation of normalised J_1 as a function of normalised J_2 (Brown et al., 2014c).

As can be observed from figure 2.16, from 180 to 2340 s following the pipeline failure, the size of the dispersing CO_2 cloud varies greatly. The half width of the cloud increases from ca. 10 to 30 m, while its downwind length decreases from ca. 170 to 90 m. As the release continues, the area of the cloud bounded by the 7% vol/vol concentration contour will gradually shrink with time, corresponding to decreasing risk levels.

Turning to figure 2.17, the variation of the normalised risk, taken as the area spanned by the 7% vol/vol concentration contour, is observed to experience an unexpected increase (from ca. 0.65 to 0.95) as the normalised costs increase from 0 to ca. 0.1. The authors reported that this was not due to real effects but a result of the model integration which led to numerical noise observed throughout. Following the unexpected increase, the normalised risk decreases hyperbolically to ca. 0.2 at a normalised cost of ca. 0.5 and approaches 0 at a normalised area of 1, as expected. The results imply that the hazard reduction obtained by increasing the number of valves becomes marginal above a certain range, indicating the existence of a threshold beyond which decreasing valve spacing provides little protection with substantial costs.

2.2.4.2 Yu et al. (2022)

The methodology proposed by Brown et al. (2014c) only considered the valve spacing as the optimisation variable. However, apart from valve spacing, other essential parameters of ESDVs such as their type and operational settings must also be considered for a valve optimisation problem. Inevitably, considering more optimisation variables leads to increased mathematical complexity whilst making solutions difficult to visualise and analyse. To overcome this limitation, variable reduction techniques can be adopted to identify the redundant optimisation variables that can be omitted.

In light of the above, Yu et al. (2022) developed an MOO methodology incorporating variable reduction techniques for selecting the optimal inline ESDV configuration for high-pressure pipelines for striking a balance amongst three objectives, namely, the ESDV capital cost, ESDV failure rate and risk associated with pipeline failure.

The MOO problem involved can be written as:

$$\text{Min}_{\mathbf{x} \in \Omega} J_1(\mathbf{x}), J_2(\mathbf{x}), J_3(\mathbf{x}) \quad 2.76$$

where, \mathbf{x} is the vector of the independent optimisation variables representing the inline ESDV configuration.

Using variable reduction techniques enabled the proposed methodology to handle multiple optimisation variables simultaneously. In this study, six optimisation variables including the ESDV type, activation pressure, combination, quantity & spacing and the failure location were considered for the MOO problem. The objective functions, $J_1(\mathbf{x})$, $J_2(\mathbf{x})$ and $J_3(\mathbf{x})$ on the other hand were respectively defined as follows.

$J_1(\mathbf{x})$, representing the risk associated with a pipeline failure, was defined as the total inventory escaping prior to complete valve closure following pipeline failure.

Mathematically, it is given by:

$$M_{total} = \int_0^{t_c} G dt + A_P \int_0^d \rho(x, t_c) dx \quad 2.77$$

where, M_{total} denotes the total inventory loss. G , t_c , d and A_P are respectively the transient mass discharge rate, valve closure time, ESDV spacing and pipe cross-section area. M_{total} was computed using the pipeline decompression model developed by Mahgerefteh et al. (1997) accounting for the impact of the valve closure dynamics.

$J_2(\mathbf{x})$, is the total annual cost of ESDVs, which was calculated using the same equation adopted by Brown et al. (2014c), given by equation 2.75.

$J_3(\mathbf{x})$, referring to the failure rate of the ESDV system installed along the pipe, was expressed as the total unavailability of the ESDV system. In the study, the failure scenario was assumed to be the FBR of a real 555 km length, 1016 mm i.d. natural gas transmission pipeline planned by China Petroleum Pipeline Engineering Corporation (CPPEC, 2012). The pipeline passes through several highly populated regions in China and the study focused on the first section of the line, from Harbin to Dehui, spanning a total length of 150.2 km. The detailed pipeline characteristics and prevailing conditions for this section are summarised in table 2.9.

Table 2.9: Pipeline characteristics and prevailing conditions for the CPPEC planned Harbin-Dehui natural gas transmission pipeline (Yu et al., 2022).

Parameter	Value
Pipe outer diameter (mm)	1051
Pipe wall thickness (mm)	17.5
Pipe roughness (mm)	0.005
Pipe length (km)	150.2
Feed pressure (bar)	80
Feed temperature (K)	307.24
Heat transfer coefficient (kW/m ² K)	5
Pipe upstream condition	Reservoir (Constant pressure)
Pipe downstream condition	Closed
Ambient pressure (bar)	1
Ambient temperature (K)	293.15

In solving the above MOO problem, the principal component analysis, one of the most frequently reported variable reduction techniques in open literature, was first applied to discard the redundant optimisation variables. This involved 1) converting the set of inter-related optimisation variables into a set of uncorrelated variables known as Principal Components (PCs) via orthogonal transformation process; 2) computing the eigenvectors and eigenvalues of the PCs measuring the amount of variance carried in each PC and 3) based on the variances computed from 2), determining the number of PCs preserving sufficient information contained in the original variables based on the 90% total variance criterion, that is, the number of PCs is considered sufficient if their variances combined account for more 90% of the variances of all PCs. Mathematically, the criterion is given by (Cadima and Jolliffe, 2001):

$$Pr_k = \frac{\sum_{i=1}^k \text{Variance}_i}{\sum_{i=1}^k \text{Variance}_i} = \frac{\sum_{i=1}^k \text{Variance}_i}{\text{tr}(Cov)} \geq 90\% \quad 2.78$$

where Pr_k denotes the cumulative proportion of the variance explained by k PCs. k is the number of selected PCs that preserve enough information contained in the original variables. Cov on the other hand, is the covariance matrix of the original variables.

Based on the selected number of PCs, Yanai's Generalised Coefficient of Determination (GCD) criterion (Ramsay et al., 1984) was then employed to select the best subset of the original variables for the subsequent multivariate analysis. Briefly, the GCD is defined as the cosine of the angle between the matrices of orthogonal projections on two subspaces, in which the degree of similarity between those subspaces is measured. The GCD criterion adopts the following algebraic form (Cadima and Jolliffe, 2001):

$$\text{GCD} = \frac{1}{k} \sum_{i=1}^k (r_m)_i^2 \quad 2.79$$

where $(r_m)_i$ is the multiple correlations between the i^{th} PC and the k selected variables.

Combining the above, the best suited subset of the original variables was then determined by 1) computing the GCD criteria for all possible subsets of the original variables for a given k ; 2) calculating the corresponding cumulative variance proportion, Pr_k for the subset that presents the maximum GCD criterion value; and 3) increasing the value of k and repeating steps 1) and 2) until Pr_k reaches 90%.

Table 2.10 presents the variable selection results based on maximising the GCD criterion. The cumulative variance proportion, Pr_k , GCD criteria and corresponding original optimisation variables described in table 2.8 are summarised.

Table 2.10: Variable selection results based on maximising the GCD criterion given by equation 2.79 (Yu et al., 2022).

k	GCD criterion	Original optimisation variable	Pr_k (%)
2	0.829	ESDV type, spacing	83.27
3	0.929	ESDV type, spacing, quantity	93.26
4	0.963	ESDV type, combination, activation pressure, spacing	97.25
5	0.999	Failure location, ESDV type, quantity, activation pressure, combination	99.98

As can be observed from table 2.10, the variance proportion of 3 PCs in total account for 93.26% of the total variance of all PCs, surpassing the 90% criterion given by equation 2.78. As such, the number of selected PCs, $k = 3$ was then determined in this study for the subsequent variable selection process. As clearly shown in the table, when $k = 3$, the GCD is 0.929 and the corresponding best subset of the original optimisation variables are the ESDV type, spacing and quantity.

The three selected optimisation variables were then applied to the MOO problem. Figure 2.18 presents the corresponding MOO results showing the variation of the normalised total inventory loss (J_1) and ESDV failure rate (J_3) as a function of the normalised total annual valve cost (J_2). The data points each represent one ESDV configuration (i.e. ESDV type, spacing and quantity).

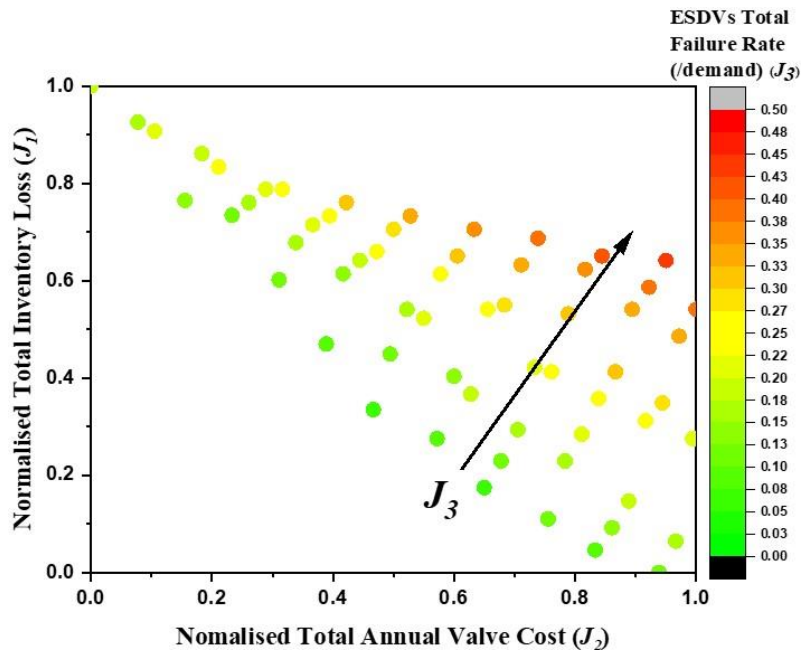


Figure 2.18: ESDV MOO results: Variation of the normalised total inventory loss (J_1) with normalised total annual valve cost (J_2). The colour of each data point represents ESDV total failure rate (J_3) (Yu et al., 2022).

As can be observed, with the increase in the annual valve cost, the total inventory loss decreases as expected while the ESDV system failure rate increases in general. This indicated that lowering the pipeline failure risks by increasing the capital investment in valves was essentially at the cost of compromising the valve system availability. Such a finding can guide the decision makers to select the optimal ESDV configuration based on their subjective preferences for the tolerable risk, cost and valve system reliability.

The authors also mentioned that though demonstrated only for hydrocarbon pipelines, the MOO technique proposed in this study could be easily employed for CO₂ pipelines.

2.2.4.3 Demissie (2015)

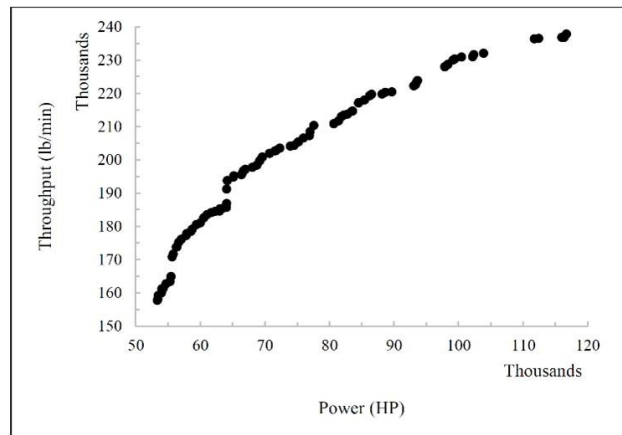
Demissie (2015) employed MOO to find the optimal pipeline and compressor design for a natural gas pipe system accounting for two objectives: 1) minimising the power consumption and 2) maximising the delivery flow rate. In this study, linear, branched

and looped topologies for the design were considered. For each topology, a corresponding MOO problem involving unique descriptions of the optimisation variables, objectives and constraints was established (see table 2.11).

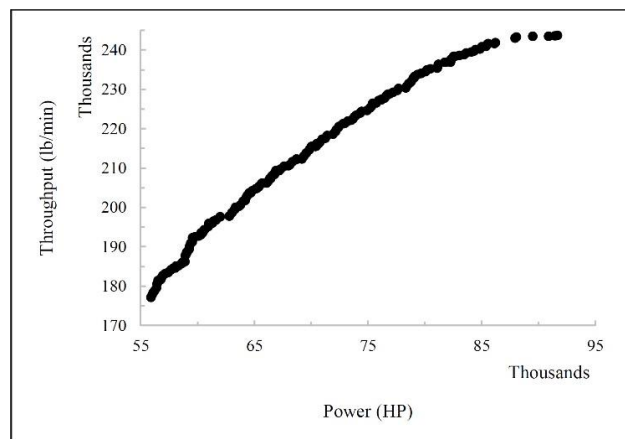
Table 2.11: Summary of the studied topologies and the key information of the corresponding MOO problems (Demissie, 2015).

Topology	Topology description	No. of optimisation variables	No. of constraints
Linear	A single supply-delivery network: 2 compressor stations, each with 6 identical compressors arranged in parallel	8	23
Branched	A branched network: 7 pipelines + 3 compressor stations	14	40
Looped	A single loop network: 6 pipelines + 2 compressor stations, each with 5 identical compressors arranged in parallel	10	30

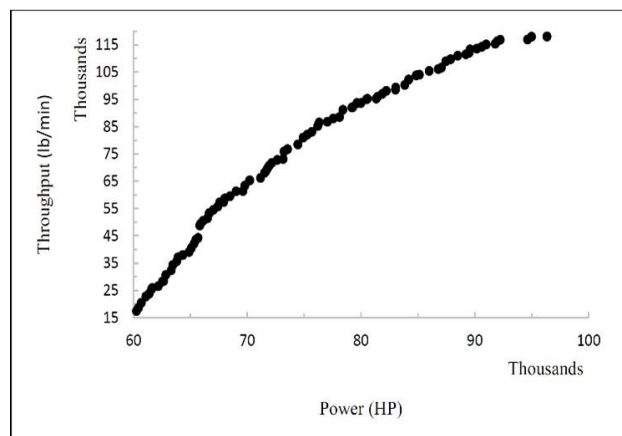
Figures 2.19 (a), (b) and (c) respectively present the MOO results showing the Pareto fronts for minimising power consumption and maximising delivery flow rate for linear (a), branched (b) and looped (c) topologies.



(a)



(b)



(c)

Figure 2.19: Pareto fronts for minimising power consumption and maximising delivery flow rate for linear (a), branched (b) and looped (c) topologies (Demissie, 2015).

As may be observed, for all three studied topologies, the delivery flow rates grow nearly logarithmically as the power consumptions increase. The points on the Pareto front represent all acceptable optimal design solutions among which, as pointed out by the author, the decision makers may select the best one based on their insights regarding the network operation and the associated costs.

2.2.4.4 Concluding Remarks

A typical MOO problem consists of three major components, namely the optimisation variables, objective functions, and constraints. From the above review, it is evident that considerable progress has been made to handle complex optimisation problems involving a large number of optimisation variables and constraints. In particular, the capability of simultaneously considering these variables and constraints has been significantly improved.

However, in the case of configuring ESDVs, the objective functions for representing the risk following pipeline failure are usually defined relatively simply. The metrics postulated for the above are usually based on the worst-case scenario of pipeline failure (i.e. FBR) while the much more probable, but nevertheless smaller magnitude failure releases (e.g. leak, puncture) are not considered in the risk estimation, therefore rendering the recommendations for ESDV configurations unreliable. As such, to further improve the degree of confidence in making such recommendations, how the MOO technique can be implemented to account for various failure scenarios (e.g. leak, puncture, FBR etc.) in configuring ESDVs needs to be studied.

Chapter 3: An Analytically Based Pressurised Pipeline Decompression Model

3.1 Introduction

As mentioned in Chapter 1, to address the long computational runtimes associated with simulating fluid decompression following pressurised pipeline failures using numerically based models, several analytically based decompression models such as a unified outflow model (Norris, 1994; Norris and Puls, 1993) and a quasi-steady state model (Webber et al., 1999) have been developed. However, it was shown that the range of applicability of the unified outflow model remains unclear and that the quasi-steady state model was limited to simulating pure components.

The Vessel Blowdown Model (VBM) (Mahgerefteh et al., 2011) (reviewed in Section 2.1.3.2) presents the most recent attempt to address the above limitations. In this model, the transient outflow from a punctured pipeline was approximated as that emanating from a vessel. The model adopted the classic vessel discharge equations (Coulson et al., 1999) to simulate the fluid flow dynamics. This essentially defined the decompression from a pipe as a solely time-dependent process requiring no numerical discretisation of the flow field for seeking solutions to the flow equations. Given this, the CPU times were drastically reduced to a negligible level. For example, the simulation of the complete depressurisation of a 5 km length, 300 mm internal diameter (i.d.) pipeline containing equi-molar methane and pentane following a 120 mm puncture took ca. 1 s on a 2.66 GHz, 3.0 GB RAM computer (Mahgerefteh et al., 2011). However, despite its exceptionally low computational costs, the VBM has two major limitations.

First, it cannot handle the highly plausible pipeline failure scenario involving unisolated releases where pumping of the pressurised inventory continues despite puncture. Second, the VBM becomes unreliable when simulating punctures larger than

40% of the pipe internal diameter. This is thought to be as a result of its static bulk flow assumptions, limiting its applicability.

In light of the above, this chapter describes the development and testing of a Modified Vessel Blowdown Model (MVBM) addressing the above limitations of the VBM. The proposed model approximates the transient outflow from an un-isolated pipeline as the blowdown from a vessel with inflow. The fluid flow equations are modified from the standard vessel discharge equations (Coulson et al., 1999) by incorporating additional mass and energy terms accounting for the effect of inflow. The fluid/wall friction effect is accounted for by a correlation used for calculating the pressure drop for isothermal steady state flow (Mahgerefteh et al., 1999). This, along with the assumption that the flow inside the pipe remains quasi-steady state during decompression, is employed to evaluate the flow conditions upstream the failure plane which in turn serve as the boundary conditions for modelling the transient mass discharge rate following pipeline failure.

The model is tested against the extensively validated but computationally demanding numerically based University College London (UCL) model (reviewed in Section 2.1.3.1) based on simulating the un-isolated releases of a hypothetical pipeline containing pure methane initially at 21 bar and 300 K. Using the same case study, the MVBM is also applied to simulate isolated releases. The results for isolated releases are verified against the predictions by both UCL model and VBM. The simulation runs for the above are based on a mid-way puncture covering a wide range of pipeline failure scenarios varying inflow rate (1 to 7.5 kg/s), pipe length (100 to 5000 m) and puncture to pipe internal diameter ratio (0.2 to 0.8). Following the testing, the CPU times of the MVBM for simulating the above failure scenarios are compared against those obtained using the UCL model.

This chapter is organised as follows. The theoretical basis for the development of the

MVBM, including the fluid flow dynamics, physical properties, initial & boundary conditions, and algorithm is first presented in Section 3.2. This is followed by the results for the verification of the MVBM against both UCL model and VBM in Section 3.3. In Section 3.4, the computational runtimes of the MVBM are analysed. Conclusions are drawn in Section 3.5.

3.2 Theory

The UCL model and VBM employed in the verification tests have been respectively reviewed in detail in Sections 2.1.3.1 and 2.1.3.2. As such, the description of their theories is omitted here. In the following section, the theoretical development of the MVBM is detailed.

3.2.1 The Discharge Model

A schematic representation of the outflow from a horizontal pressurised pipeline is given in figure 3.1, indicating the pertinent fluid properties used in the mathematical development of the new analytically based pipeline decompression model.

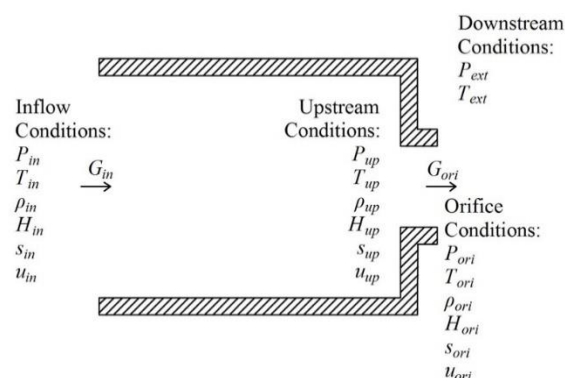


Figure 3.1: Schematic representation of the outflow from a horizontal pressurised pipeline indicating the pertinent fluid properties required for the mathematical development of the MVBM. The symbols are defined in Sections 3.2.1 to 3.2.5.

To avoid numerical discretisation in solving the flow equations to maintain a high level of computational efficiency, the standard analytically based vessel discharge equations adapted for the HEM assumption (Martynov et al., 2014) are employed to describe the outflow from a horizontal pressurised pipeline following its failure. Written in integral form, the corresponding mass and energy conservation equations are given by:

$$\frac{dM_o}{dt} = -G_{ori} \quad 3.1$$

$$\frac{dM_o e_o}{dt} = -G_{ori} h_{ori} + \dot{Q} \quad 3.2$$

where M and e are respectively the mass and specific energy. G and h on the other hand are respectively the mass discharge rate and specific enthalpy. The subscripts, o and ori respectively denote the pipe bulk fluid and orifice fluid conditions (see figure 3.1). \dot{Q} on the other hand, refers to the fluid/wall heat transfer, which is defined using the Newton's cooling law (reviewed in Section 2.1.2.4.2, Chapter 2).

To account for pipe inflow, additional mass and energy terms are incorporated into equations 3.1 and 3.2, giving:

$$\frac{dM_o}{dt} = G_{in} - G_{ori} \quad 3.3$$

$$\frac{dM_o E_o}{dt} = G_{in} H_{in} - G_{ori} H_{ori} + \dot{Q} \quad 3.4$$

where the subscript, in denotes the inlet fluid condition (see figure 3.1). E and H are respectively the specific total energy and specific total enthalpy respectively defined by:

$$E = e + \frac{u^2}{2} \quad 3.5$$

$$H = h + \frac{u^2}{2} \quad 3.6$$

Using the following thermodynamic relations:

$$dh = Tds + VdP \quad 3.7$$

$$h = e + PV \quad 3.8$$

where T , P , s and V are respectively the temperature, pressure, specific entropy and specific volume.

And replacing the pipe inventory mass with the product of the density of the pipe bulk fluid, ρ_o and pipe volume, V_o :

$$M_o = \rho_o V_o \quad 3.9$$

Equations 3.3 and 3.4 then become:

$$V_o \frac{d\rho_o}{dt} = G_{in} - G_{ori} \quad 3.10$$

$$\rho_o V_o T_o \frac{ds_o}{dt} = G_{in}(H_{in} - H_{up}) + G_{ori}(H_{up} - H_{ori}) + \dot{Q} \quad 3.11$$

3.2.2 Physical Properties

The fluid thermodynamic properties and phase equilibrium data are computed using the

Peng-Robinson Equation of State (PR EoS) (Peng and Robinson, 1976), the details of which are reviewed in Section 2.1.2.5.1, Chapter 2 and are again presented below:

$$P = \frac{RT}{V_m - b_p} - \frac{a_p \alpha_p}{V_m^2 + 2b_p V_m - b_p^2} \quad 3.12$$

$$a_p = 0.45724 \frac{R^2 T_c^2}{P_c} \quad 3.13$$

$$b_p = 0.07780 \frac{RT_c}{P_c} \quad 3.14$$

$$\alpha_p = \left(1 + (0.37464 + 1.54226\omega - 0.26992\omega^2)(1 - T_r^{0.5})\right)^2 \quad 3.15$$

$$T_r = \frac{T}{T_c} \quad 3.16$$

The number of the fluid phases present in the flow during pipeline decompression is determined by the stability test based on the Gibbs tangent plane criterion (Michelsen, 1982). The properties of a two-phase mixture are handled based the Homogeneous Equilibrium Mixture (HEM) assumption, that is, the pressure, temperature and velocity are identical across phases. The pseudo properties including the heat capacity, specific volume, energy, and entropy of two-phase mixtures are calculated based on mass-averaged pure liquid and pure gas properties obtained from PR EoS:

$$\phi_f = \phi_g \chi + \phi_l (1 - \chi) \quad 3.17$$

where ϕ_f , ϕ_g and ϕ_l are the mass-specific properties of a two-phase mixture and its constituent saturated vapour and liquid phases, respectively. χ on the other hand, is the fluid quality.

The local speed of sound, c and φ are calculated either analytically or numerically, depending on the number of phases presented in the flow. For single-phase fluids, the speed of sound is determined analytically using (Groves et al., 1978; Picard and Bishnoi, 1988):

$$c^2 = \frac{\gamma}{\kappa\rho} \quad 3.18$$

$$\varphi = \frac{\rho\xi T c^2}{C_p} \quad 3.19$$

where γ and C_p are the ratio of specific heats and isobaric specific heat capacity, respectively. κ is the isothermal coefficient of volumetric expansion, given by (Walas, 1985):

$$\kappa = -\rho \left(\frac{\partial V}{\partial P} \right)_T \quad 3.20$$

ξ on the other hand, is the isobaric coefficient of volumetric expansion, which is given by:

$$\xi = \frac{1}{V} \left(\frac{\partial V}{\partial P} \right)_T \quad 3.21$$

The term $\left(\frac{\partial V}{\partial P} \right)_T$, which is the differentiation of the PR EoS, is given by:

$$\left(\frac{\partial V}{\partial P} \right)_T = \left(\frac{RT}{(V_m - b_p)^2} - \frac{2a_p\alpha_p(V_m + b_p)}{(V_m^2 + 2b_pV_m - b_p^2)^2} \right)^{-1} \quad 3.22$$

For two-phase mixtures, defining γ and C_p becomes complicated (Mahgerefteh et al.,

1999) and the speed of sound, c and φ are evaluated numerically:

$$c^2 = \frac{\Delta P}{\rho(T, P)_s - \rho(T^*, P - \Delta P)_s} \quad 3.23$$

$$\varphi = \rho^2 \left(\frac{\Delta T}{\Delta \rho} \right)_s \quad 3.24$$

Equation 3.23 is solved for T^* iteratively using Newton-Raphson method with the following objective function:

$$\omega^{(n)} = s(T, P)_s - s(T^{*(n)}, P - \Delta P)_s \quad 3.25$$

where n denotes the iteration level.

3.2.3 Initial Conditions

Due to fluid/wall friction, the presence of inflow leads to pressure drop inside the pipe resulting in the variation of fluid properties along the pipe (Menon, 2005). As a result, the fluid conditions upstream the orifice vary at different failure locations. Such conditions finally govern the orifice conditions during the release and therefore are fundamentally important for the subsequent outflow assessment. Given this, frictional losses must be accounted for, especially for long pipelines where the pressure drop is significant.

In the present study, to maintain a coherent analytical scheme, an analytically based, 1-D, isothermal, steady state model following Mahgerefteh et al. (1999) is employed to evaluate the fluid conditions prior to pipeline failure. The corresponding pressure drop between two given locations along the pipe, respectively denoted by 1 and 2, is given by:

$$P_2 = P_1 + \frac{\beta_{x,1}}{\left[1 - \frac{u^2}{ZRT}\right]_1} (x_2 - x_1) \quad 3.26$$

where Z is the compressibility factor. β_x on the other hand, is the fluid/wall friction which is defined as:

$$\beta_x = -\frac{2\rho u|u|f_w}{D_{in}} \quad 3.27$$

The Fanning friction factor, f_w is determined based on the Reynold's number:

$$Re = \frac{\rho u D_{in}}{\mu_f} \quad 3.28$$

where, μ_f is the fluid viscosity, which is determined as follows.

For single-phase flows, the fluid viscosity is calculated using the Ely and Hanley scheme for gas and the Dymond and Assael scheme for liquid (Massey, 1983). For two-phase mixtures, the viscosity is determined based on mass-averaged pure liquid and pure gas properties (Mahgerefteh et al., 1999):

$$\frac{1}{\mu_f} = \frac{\chi}{\mu_g} + \frac{(1 - \chi)}{\mu_l} \quad 3.29$$

where the subscripts, g and l respectively denote the vapour and liquid phases.

Turning back to the Fanning friction factor, for transition and turbulent flows ($4000 < Re < 4 \times 10^8$), it is calculated using Chen's correlation (Chen, 1979) given its simple analytical form and high accuracy when compared to Colebrook correlation (Colebrook, 1939) which is accepted as the benchmark in Fanning friction factor predictions

(Ouyang and Aziz, 1996). For laminar pipe flow ($Re < 2300$), the friction factor is computed using a standard correlation given by Rohsenow et al. (1998).

The details of both correlations are reviewed in in Section 2.1.2.4.1, Chapter 2.

3.2.4 Boundary Conditions

The flow inside the pipe is assumed to be quasi-steady state following pipeline failure, that is:

$$G_{up} = G_{in} \quad 3.30$$

where, G_{up} is the mass flow rate upstream the orifice.

By assuming quasi-steady state flow inside the pipe, equations 3.26 adopted for the initial condition calculation (see Section 3.2.3) can then be applied to calculate the instantaneous fluid conditions upstream the orifice during pipeline decompression. The same assumption was adopted by Webber et al. (1999) in the development of a two-phase discharge model for pipeline FBR and was found to have good validity following the model's validation against Isle of Grain P40 test (Richardson and Saville, 1996). It should be noted that by adopting this assumption, the bulk fluid temperature along the pipe is unchanged during decompression.

The orifice flow conditions are determined using the steady state 'straw method' (Morin et al., 2012). This method essentially involves establishing an energy balance across the orifice assuming isentropic fluid expansion. Mathematically, the energy balance and isentropic condition can be respectively expressed as:

$$h_{up} + \frac{1}{2}u_{up}^2 = h_{ori} + \frac{1}{2}u_{ori}^2 \quad 3.31$$

$$s_{ori} = s_{up} \quad 3.32$$

where the subscript, up denotes the condition of the fluid upstream the orifice (see figure 3.1).

For choked flows, equation 3.31 is solved iteratively using the Brent method (Press, 1992). This involves guessing and updating the choked pressure based on the isentropic expansion assumption until equation 3.31 is satisfied. Once a solution is obtained, other fluid conditions at the orifice are determined by performing a corresponding pressure-entropy flash calculation. In this case, the orifice choked fluid velocity, u_{ori} in equation 3.31 is equal to the local speed of sound:

$$u_{ori} = c \quad 3.33$$

For unchoked flows, no iterations are required to determine the fluid conditions at the orifice. Here, the orifice pressure, P_{ori} is equal to the pipe external (ambient) pressure, P_{ext} , that is:

$$P_{ori} = P_{ext} \quad 3.34$$

Knowing the above, equation 3.31 is then directly solved for u_{ori} . Other fluid conditions are computed following a corresponding pressure-entropy flash calculation based on the isentropic expansion assumption (equation 3.32).

A detailed calculation algorithm for evaluating the orifice flow conditions is presented in figure 3.2.

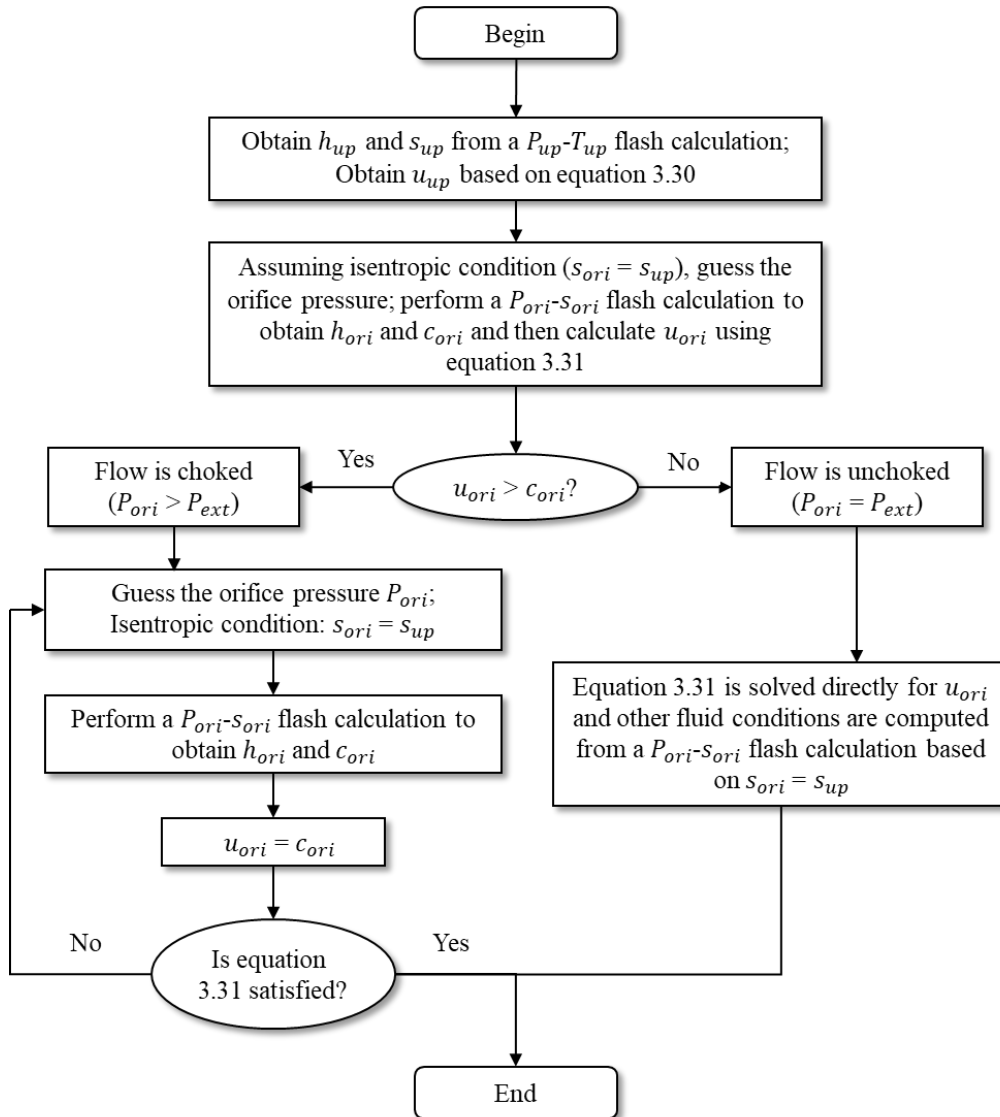


Figure 3.2: Calculation algorithm for evaluating the orifice flow conditions.

The inlet condition on the other hand is assumed to correspond to the fluid being pumped at a constant flow rate during depressurisation, that is:

$$G_{in} = \text{const} \quad 3.35$$

3.2.5 Non-isentropic Effect

The resistance posed by the orifice plane and the fluid/pipe wall heat transfer introduce

irreversibility leading to non-isentropic conditions. As a result, the exiting flow will undergo a contraction in its area and its actual flow rate is expected to be smaller than that under the isentropic condition. The contracted flow is often known as Vena Contracta. This effect can be particularly significant in the case of puncture failures. In calculating the mass discharge rate, the discharge coefficient is introduced to account for the non-isentropic effect, that is:

$$G_{ori} = C_D \rho_{ori} u_{ori} A_{ori} \quad 3.36$$

where ρ_{ori} and A_{ori} are the orifice fluid density and orifice area, respectively. C_D on the other hand, is the discharge coefficient, given by:

$$C_D = \frac{\text{Area of Vena Contracta}}{\text{Area of orifice}} \quad 3.37$$

3.2.6 Algorithm

The calculation algorithm for simulating the pipeline decompression process using the MVBM is presented in detail in figure 3.3.

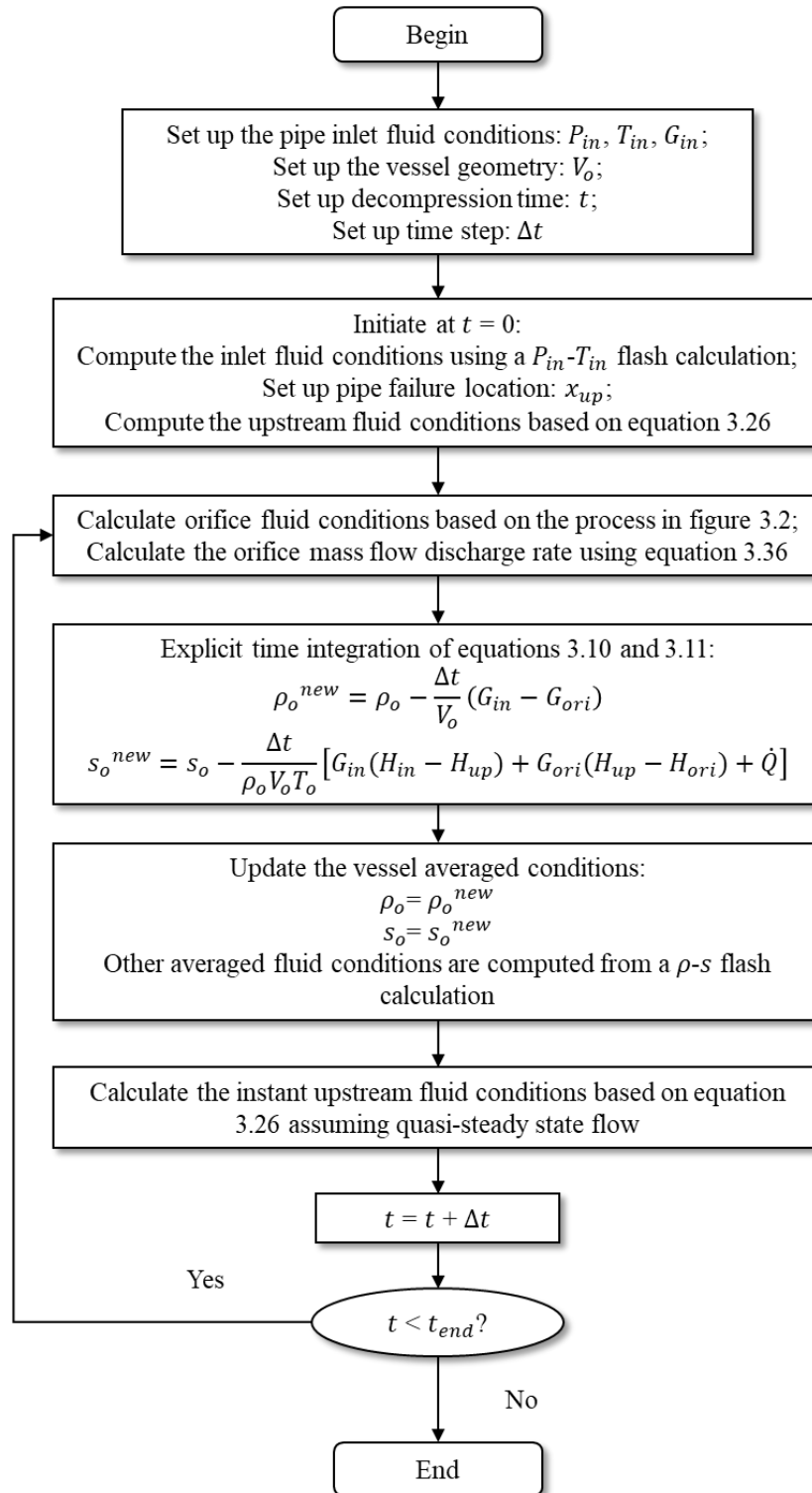


Figure 3.3: Detailed calculation algorithm for simulating the pipeline decompression process using the MVBM.

The decompression process calculation algorithm as presented in figure 3.3 is described as follows:

- 1) Set up the pipe inlet fluid conditions, P_{in} , T_{in} , G_{in} , vessel geometry, V_o and decompression time, t .
- 2) For a given pipeline failure location, calculate the fluid conditions upstream the orifice using equation 3.26.
- 3) Calculate the orifice pressure, P_{ori} using equation 3.31 and other orifice fluid conditions by performing a corresponding pressure-entropy flash calculation based on the isentropic expansion assumption (equation 3.32).
- 4) Update the bulk fluid conditions using equations 3.10 and 3.11.
- 5) Use the updated bulk fluid conditions from step 4) to update the fluid conditions upstream the orifice using equation 3.26 based on the quasi-steady state flow assumption (see Section 3.2.4).
- 6) Go to step 3) and terminate the calculation until the decompression time, t is reached.

3.3 Verification

3.3.1 Case Study

The efficacy of the MVBM is tested against the rigorously validated UCL model (reviewed in Section 2.1.3.1) and the analytically based VBM (reviewed in Section 2.1.3.2) using a hypothetical 300 mm i.d. thermally insulated pipeline. The pipeline is assumed to contain pure methane. The relevant pipeline characteristics and prevailing conditions are summarised in table 3.1. The failure location is assumed to be mid-way along the pipe. The tests involve simulating both un-isolated and isolated releases

covering several realistic failure scenarios. For the simulations using the numerically based UCL model, an automatic nested grid system (Mahgerefteh et al., 1999) applying finer numerical discretisation near the orifice plane is used. For simplicity, a discharge coefficient of unity is assumed.

Table 3.1: Pipeline characteristics and prevailing conditions used for the simulation tests for examining the efficacy of the MVBM.

Parameter	Value	
<i>Pipe characteristics</i>	Pipe internal diameter (mm)	300
	Pipe wall thickness (mm)	10
	Pipe roughness (mm)	0.05
	Heat transfer coefficient (W/m ² K)	5
<i>Inlet conditions</i>	Feed composition (mol%)	Methane 100
	Feed pressure (bar)	21
	Feed temperature (K)	300
<i>Failure parameters</i>	Failure location	Mid-length
	Discharge coefficient	1
<i>Ambient conditions</i>	Ambient pressure (bar)	1.01
	Ambient temperature (K)	290

3.3.2 Simulation of Un-isolated Releases

In this section, the efficacy of the MVBM in handling un-isolated releases is tested. The simulation runs are based on a range of pipeline failure scenarios varying the feed flow rate (1 to 7.5 kg/s), pipe length (100 to 5000 m) and puncture to pipe internal diameter ratio (0.2 to 0.8). The simulated mass discharge rate-time profiles from both UCL model and the MVBM are compared.

3.3.2.1 Impact of Feed Flow Rate

Figure 3.4 shows the simulated mass discharge rate variation with time predicted by both models. The data points and solid lines are respectively the predictions of the UCL model and MVBM. The simulated results are produced for pipeline feed rates ranging from 1 to 7.5 kg/s. A puncture to pipe internal diameter ratio of 0.2 (puncture diameter = 60 mm) is chosen. Other pipeline characteristics and prevailing conditions used for the simulations are summarised in table 3.1.

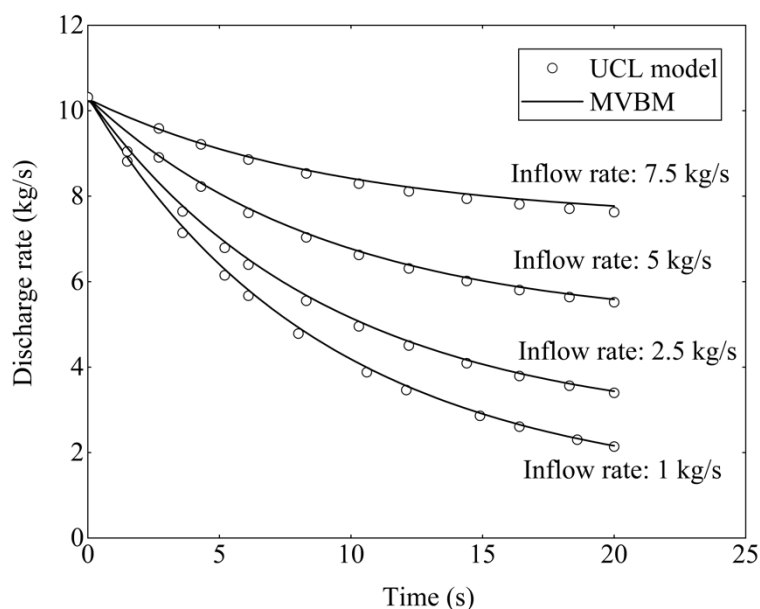


Figure 3.4: Comparison of the mass discharge rate variation with time at the orifice based on the UCL model (data points) and MVBM (solid lines) predictions for different inflow rates (puncture to pipe internal diameter ratio: 0.2; pipe length: 100 m).

As can be observed from figure 3.4, the MVBM produces generally good agreement with the UCL model predictions indicating minor discrepancies throughout for all tested feed flow rates. As the decompression continues, the mass discharge rate decreases more slowly with time in the case of a higher inflow rate. A reason for this is that a higher inflow rate provides more compensation to the inventory during

decompression. This would essentially maintain the pressure inside the pipe at a higher level, therefore leading to a slower rate of decompression. It should be noted that the mass discharge rate will eventually reach the initial inflow rate as the depressurisation proceeds.

Table 3.2: Average % error in the mass discharge rate for the MVBM predictions at different inflow rates.

Inflow rate (kg/s)	Average % error
1	2.02
2.5	1.66
5	1.09
7.5	0.97

Table 3.2 presents the corresponding average % error in the mass discharge rate for the MVBM predictions at different inflow rates. As may be observed, as the feed flow rate increases, the error in the MVBM predictions decreases. As mentioned earlier, this may be attributed to the fact that during decompression, a larger feed flow rate replenishes the inventory to a greater extent and hence the upstream fluid conditions will be less affected by the rapid fluid expansion near the failure orifice. As a result, the quasi-steady state flow assumption (see Section 3.2.4) becomes increasingly applicable.

3.3.2.2 Impact of Pipe Length

The following examines the efficacy of the MVBM in handling un-isolated flow as a function of pipeline length. Figure 3.5 shows the mass discharge rate variation with time predicted by both models. The data points and solid lines are respectively the predictions of the UCL model and MVBM. The results are determined for different pipe lengths: 500, 1000, 2500 and 5000 m. A feed flow rate of 2.5 kg/s is assumed in all simulation runs. The puncture to pipe internal diameter ratio on the other hand is taken as 0.2 (i.e. puncture diameter = 60 mm). Other pipeline characteristics and prevailing

conditions used for the simulations are summarised in table 3.1.

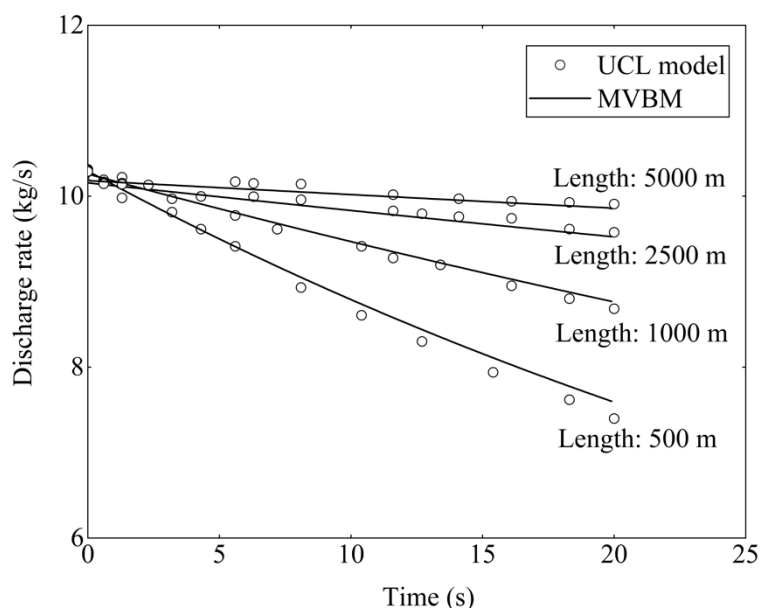


Figure 3.5: Comparison of the mass discharge rate variation with time at the orifice based on the UCL model (data points) and new model (solid lines) predictions for different pipe lengths (puncture to pipe internal diameter ratio: 0.2; inflow rate: 2.5 kg/s).

Once again, relatively good agreement between the predictions of the UCL model and the MVBM is obtained for all pipe lengths tested. The profiles display a similar pattern with those in figure 3.4. As the pipe length increases, the mass discharge rate tends to decrease more slowly with time. Given that a longer pipeline contains a larger amount of inventory, it is therefore capable of maintaining the pressure inside the pipe for a longer duration following pipeline failure. This in turn would lead to a slower decompression rate as compared to that for a shorter pipeline.

Table 3.3: Average % error in the mass discharge rate for the MVBM predictions as compared to the UCL model predictions at different pipe lengths.

Pipe length (m)	Average % error in the mass discharge rate between the UCL model and MVBM predictions
500	1.33
1000	0.83
2500	0.62
5000	0.43

Table 3.3 presents the corresponding average % error in the mass discharge rate for the MVBM predictions at different pipe lengths. As may be observed, the MVBM delivers better performances for longer pipelines. The reason for the above is similar as that discussed for the study of different inflow rates (see Section 3.3.2.1). Given the larger inventory in a longer pipeline, the quasi-steady state flow assumption (see section 3.2.4) becomes more applicable.

3.3.2.3 Impact of Puncture to Pipe Internal Diameter Ratios

This section primarily investigates the capability of the MVBM in handling different puncture to pipe internal diameter ratios. The failure scenarios investigated involve 60, 120, 180 and 240 mm punctures, respectively corresponding to 0.2, 0.4, 0.6 and 0.8 puncture to pipe internal diameter ratios. Figures 3.6 (a), (b), (c) and (d) respectively present the simulated mass discharge rate-time profiles from both models for 0.2, 0.4, 0.6 and 0.8 puncture to pipe internal diameter ratios. The data points and solid lines are respectively the predictions of the UCL model and MVBM. The results are determined for a 100 m length methane pipe with 2.5 kg/s inflow rate. Other pipeline characteristics and prevailing conditions used for the simulations are included in table 3.1. Table 3.4 on the other hand, shows the corresponding average % error in the mass discharge rate

for the MVBM predictions as compared to the UCL model predictions at different puncture to pipe internal diameter ratios.

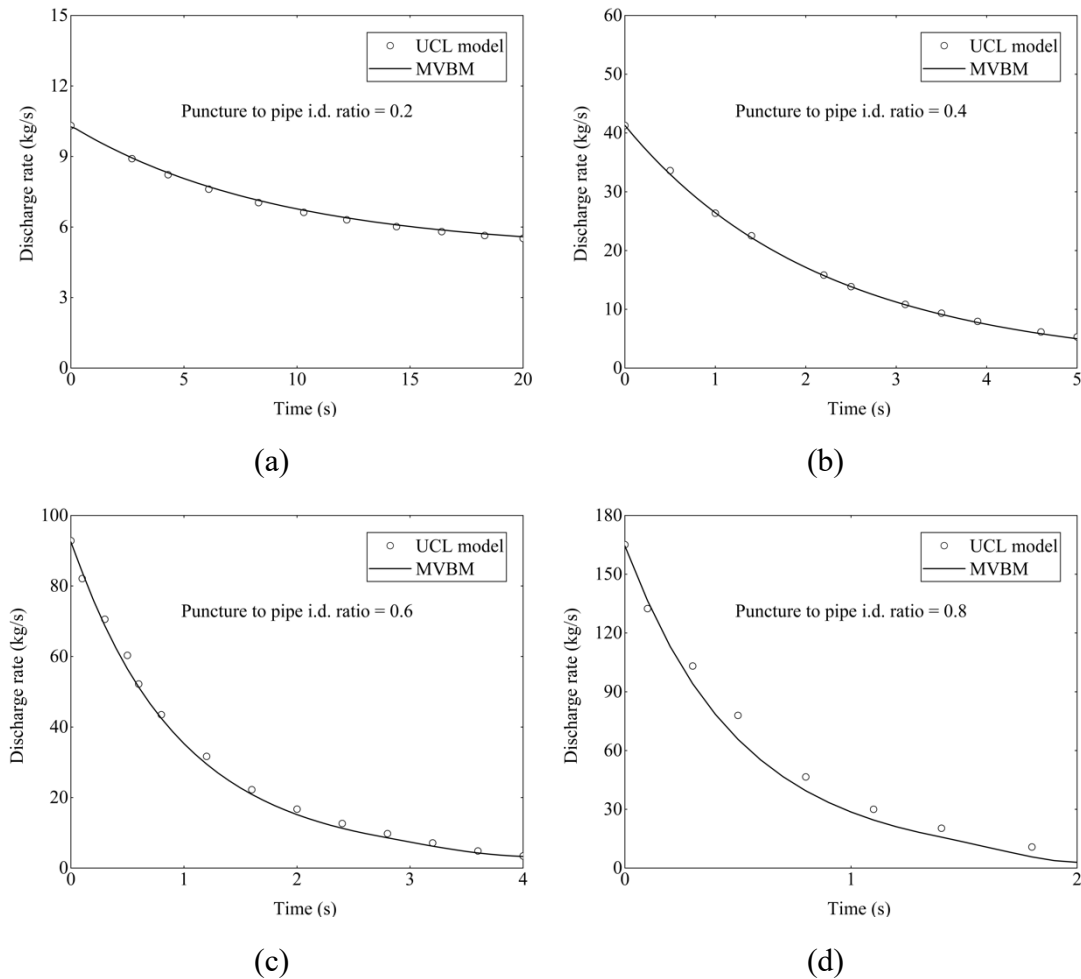


Figure 3.6: Comparison of the mass discharge rate variation with time at the orifice based on the UCL model (data points) and MVBM (solid lines) predictions for 0.2 (a), 0.4 (b), 0.6 (c) and 0.8 (d) puncture to pipe internal diameter ratios (pipe length: 100 m; feed flow rate: 2.5 kg/s).

As may be observed from figure 3.6, for all investigated values of puncture to pipe internal diameter ratio, generally good agreement can be observed between the two model predictions. The above is considered a substantial improvement to the VBM where, as mentioned in Section 3.1, punctures larger than 40% of the pipe internal diameter cannot be handled (Mahgerefteh et al., 2011). This limitation of the VBM

could be due its isothermal bulk flow assumption, which ignores the fluid/wall heat exchanges during pipeline decompression. When the puncture diameter increases, such an assumption becomes increasingly inapplicable given the much quicker decompression involved which leads to rapid cooling inside the pipe.

Table 3.4: Average % error in the mass discharge rate for the MVBM predictions at different puncture to pipe internal diameter ratios.

Puncture to pipe internal diameter ratio	Average % error in the mass discharge rate between the UCL model and MVBM predictions
0.2	1.66
0.4	1.71
0.6	2.63
0.8	6.88

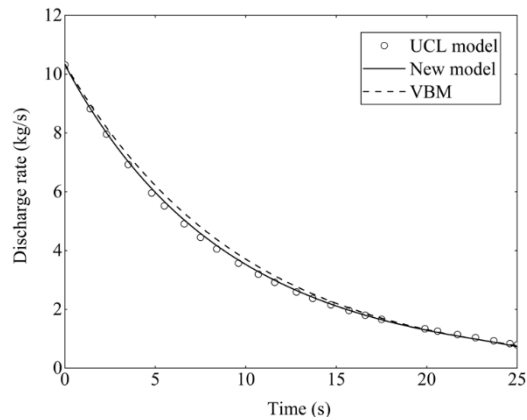
Despite the generally good agreement observed for all the puncture to pipe internal diameter ratios investigated, turning to the average % error in the predictions as shown in table 3.4, it is noteworthy that discrepancy between the predictions of the UCL model and MVBM increases with increasing puncture to pipe internal diameter ratio. The above is probably due to the different magnitudes of fluid/wall friction involved. A larger puncture leads to a higher acceleration of the fluid upstream the orifice thus resulting in increase in the frictional losses. However, given the present model assumes quasi-steady flow, such frictional losses and hence the corresponding energy losses are not taken into consideration. Consequently, the above assumption becomes increasingly inapplicable with increase in puncture diameter thus leading to increased computational errors.

3.3.3 Simulation of Isolated Releases

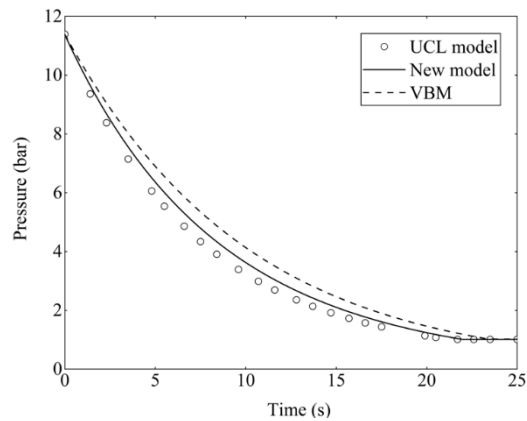
Isolated pipeline releases, where there is no feed flow, are also simulated using the

MVBM. The simulation results are verified against the predictions of the UCL model and VBM. The simulations involve two puncture diameter scenarios including 60 and 120 mm, respectively corresponding to 0.2 and 0.4 puncture to pipe internal diameter ratios. The results are determined for a 100 m length isolated pipeline. Other pipeline characteristics and prevailing conditions used for the simulations are summarised in table 3.1.

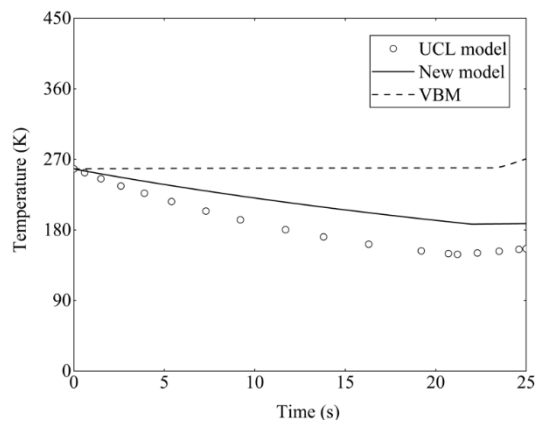
Figures 3.7 and 3.8 show the simulated variations of the mass discharge rate, pressure and temperature with time predicted by the three models for 0.2 and 0.4 puncture to pipe internal diameter ratios respectively. The data points, dashed lines and solid lines respectively represent the simulated results from the UCL model, VBM and MVBM.



(a)

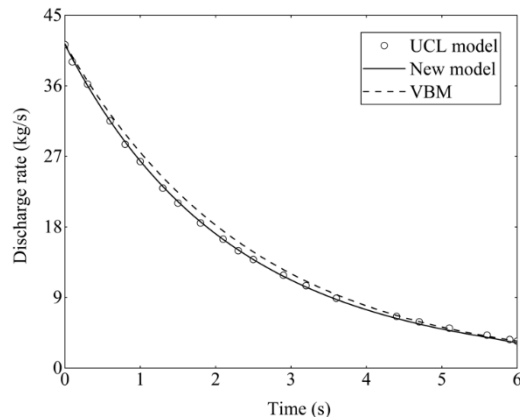


(b)

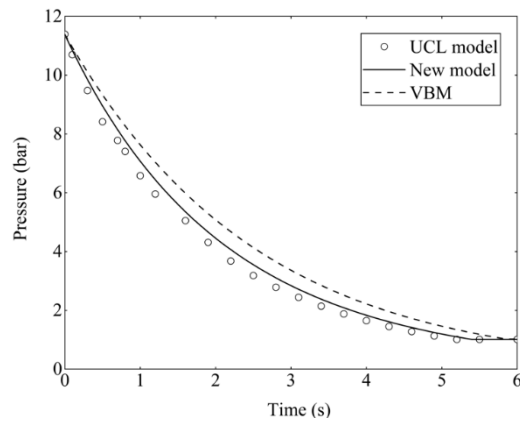


(c)

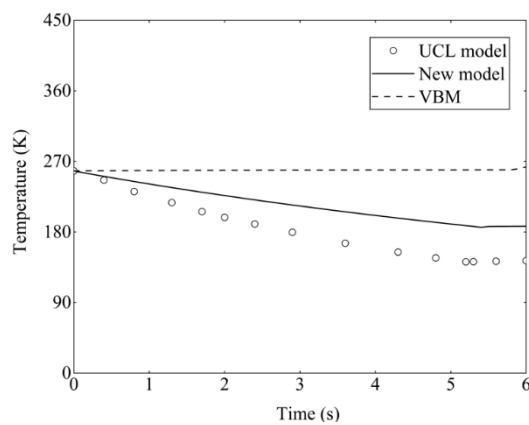
Figure 3.7: Comparison of the mass discharge rate (a), pressure (b) and temperature (c) variations with time at the rupture plane based on the UCL model (data points), VBM (dashed lines) and MVBM (solid lines) predictions for 0.2 puncture to pipe internal diameter ratio (pipe length: 100 m; feed flow rate: 0 kg/s).



(a)



(b)



(c)

Figure 3.8: Comparison of the mass discharge rate (a), pressure (b) and temperature (c) variations with time at the rupture plane based on the UCL model (data points), VBM (dashed lines) and MVBM (solid lines) predictions for 0.4 puncture to pipe internal diameter ratio (pipe length: 100 m; feed flow rate: 0 kg/s).

As can be observed from figures 3.7 and 3.8 for both puncture to pipe internal diameter ratio values investigated, the MVBM produces better agreement with the UCL model as compared to the VBM predictions throughout the decompression process. The reason for the improved performance is most likely a consequence of the fact that as opposed to the VBM, the MVBM accounts for fluid/wall heat exchange where isothermal flow assumption adopted in the former case is based on infinite fluid/wall heat transfer which is unrealistic.

Turning to the temperature-time profiles (see figures 3.7 (c) and 3.8 (c)), the MVBM also produces better agreement with the UCL model as compared to the VBM predictions throughout the decompression process. The simulated temperature profile using the VBM displays a marginal increase in temperature with time during the decompression process. The MVBM, on the other hand, performs reasonably well in reproducing the temperature-time history as compared to the UCL model where, the fluid temperature initially declines due to rapid decompression, and gradually recovers as a result of the finite heat transfer from the warmer surrounding ambient through the pipe wall.

It is noteworthy that the performance of the MVBM in predicting the temperature-time profiles is generally worse than those in predicting the mass discharge rate and pressure-time profiles. This may be due to the quasi-steady state flow assumption employed (see Section 3.2.4). As a consequence of this assumption, the MVBM considers a uniform temperature along the pipe length during decompression. As a result, the expansion-induced Joule Thomson cooling effect at rupture plane, which leads to much lower temperatures in the vicinity of the puncture as compared to the rest of the pipeline, is not taken into consideration.

3.3.4 Source of Errors

The quasi-steady state flow assumption made in the development of the MVBM (see

Section 3.2.4) can invariably induce errors in the simulations. These errors will be eventually reflected on the evaluation of the LHS of equation 3.31, which is the energy balance prescribed for the boundary condition calculations, as rewritten below:

$$h_{up} + \frac{1}{2}u_{up}^2 = h_{ori} + \frac{1}{2}u_{ori}^2 \quad 3.31$$

The first term on the LHS of the equation represents the upstream enthalpy. The second term on the other hand, is the upstream kinetic energy. Their summation is often referred to as the total upstream enthalpy, denoted by H_{up} . Whether this term is calculated accurately determines the accuracy of the predictions for the orifice flow conditions.

Based on the previous discussion for the simulations of both un-isolated and isolated releases (see Sections 3.3.2 and 3.3.3), there could be two sources of errors in computing H_{up} . These are:

- 1) Errors incurred by ignoring the bulk fluid acceleration upstream the failure location, which will lead to the underprediction of the corresponding upstream kinetic energy, $\frac{1}{2}u_{up}^2$ in equation 3.31;
- 2) Errors incurred by assuming uniform bulk fluid temperature along the pipe length, which ignores the expansion-induced cooling effect to the bulk fluid upstream of the failure location that will in turn result in the inaccurate prediction of the upstream enthalpy, h_{up} in equation 3.31.

In the following, the importance of the two sources of errors outlined above will be assessed by studying their contribution to the upstream total enthalpy, H_{up} based on simulating different failure scenarios involving various puncture diameters.

Figure 3.9 presents the results for investigating the importance of the sources of errors, showing the variation of the upstream kinetic energy to total upstream enthalpy ratio

$(\frac{1}{2}u_{up}^2/H_{up})$ with time following pipeline failures. The data are generated using the UCL model for different puncture diameters including 60, 120, 180 and 240 mm respectively corresponding to 0.2, 0.4, 0.6 and 0.8 puncture to pipe internal diameter ratios. A 100 m length, 2.5 kg/s feed flow rate pipeline is simulated as an example. Other pipeline characteristics and prevailing conditions used for the simulations are summarised in table 3.1.

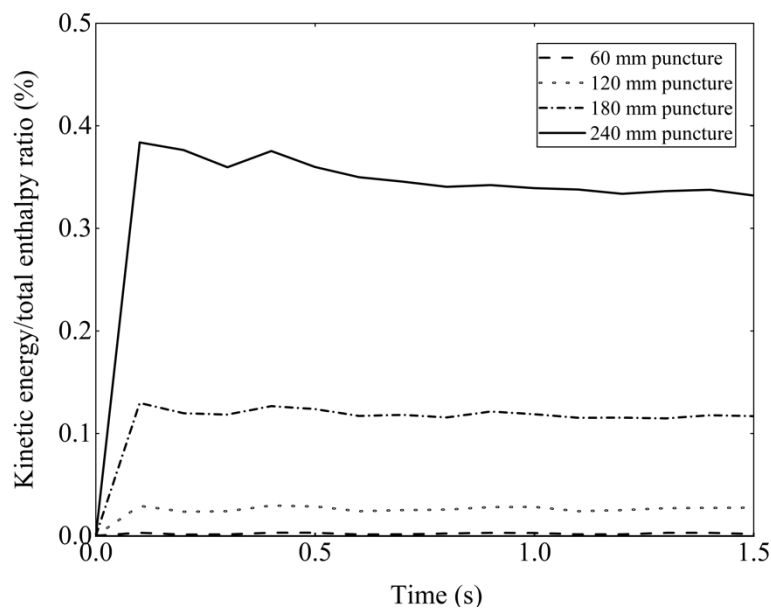


Figure 3.9: Results for investigating the importance of the sources of errors, showing the variation of the kinetic energy/total enthalpy ratio $(\frac{1}{2}u_{up}^2/H_{up})$ with time at the upstream of the orifice for 60, 120, 180 and 240 mm puncture diameters.

As can be observed, an increase in puncture diameter results in a corresponding increase in the upstream kinetic energy to total upstream enthalpy ratio. This means that as the puncture diameter increases, the contribution of the kinetic energy to the total enthalpy will increase. This is consistent with the observation from table 3.4 that as the puncture diameter increases, the simulation errors will increase. However, despite this, the kinetic energy/total enthalpy ratios for all puncture diameters are small in absolute terms, with the largest value observed being only ca. 0.4%. This means even for very

large punctures, the impact of the first source of errors on the simulation results can be very limited.

The above indicates that for the investigated scenarios, the upstream enthalpy, h_{up} dominates the total upstream enthalpy, H_{up} . As a result, assuming uniform bulk fluid temperature along the pipe length (the second source of errors) could have a much more substantial impact on the simulation results than ignoring the bulk fluid acceleration upstream the failure location (the first source of errors).

3.4 Computational Runtimes

Table 3.5 presents the comparison of the computational runtimes between the UCL model and MVBM for simulating various pipeline failures. The simulations involve the complete decompression of isolated pipelines with lengths corresponding to 100, 1000 and 5000 m. The selected puncture diameter for these simulations is 60 mm, corresponding to 0.2 puncture to pipe internal diameter ratio. All other input conditions used are summarised in table 3.1. These simulations are performed using a 3.80 GHz, 16.0 GB RAM computer.

Table 3.5: Comparison of the computational runtimes between UCL model and MVBM.

Pipe length (m)	Computational runtimes		
	UCL model	MVBM	% reduction
100	1 min 41 s	6.6 s	93.44
1000	16 min 37 s	55.9 s	94.39
5000	2 hr 34 min 59 s	4 min 6 s	97.35

As can be observed from table 3.5, the computational runtimes using the MVBM are significantly lower than those based on the UCL model for all pipe lengths simulated. Such reductions are even more notable in the case of longer pipelines. This makes the

application of the MVBM to simulating long pipelines particularly attractive.

3.5 Concluding Remarks

In this chapter, the development and testing of a computationally efficient analytically based MVBM for predicting the outflow pressurised pipeline decompression model was described. The developed model addresses the fundamental limitations of the VBM in handling un-isolated releases and punctures with relatively large puncture to pipe internal diameter ratios. It should be noted that, though tested on hydrocarbon pipelines, the MVBM was developed for general-purposed use and therefore can be readily implemented to simulate CO₂ pipeline failures.

Based on the results and analysis presented in this chapter and the ranges of the parameters tested, the following key conclusions may be made:

- The MVBM has been successfully extended to simulate un-isolated releases and punctures with relatively large puncture to pipe internal diameter ratios, presenting a substantial improvement as compared to the VBM;
- The accuracy of the MVBM decreases with the increase in puncture to pipe internal diameter ratio. This could be due to the increasing incapability of the quasi-steady state assumption employed, which ignores the growing influence of fluid/wall frictional effects in the vicinity of the puncture as its diameter increases;
- The MVBM performs generally better as the feed flow rate or the pipe length increases. This may be attributed to the fact that a larger feed flow rate or a longer pipeline usually comes with a larger pipe inventory that will render the quasi-steady state flow assumption of the MVBM increasingly applicable during decompression;
- Ignoring the bulk fluid acceleration upstream of the failure location, and assuming isothermal flow along the pipe length were respectively postulated to be the two

main sources of simulation errors in the MVBM. An analysis of both factors showed that the isothermal flow assumption introduced the bigger source of error;

- An analysis of the computational runtimes showed that using the MVBM, the computational runtimes in simulating pipeline puncture failures could be significantly reduced by over 90% as compared to using the numerically based UCL model. Such reductions were even more notable for longer pipelines, making the application of the MVBM in simulating long pipelines particularly attractive.

Chapter 4: An Analytical Approach to Estimate Failure Puncture Size Probability Distribution for Pressurised CO₂ Pipelines

4.1 Introduction

As highlighted in Chapter 1, an important part of the Quantitative Risk Assessment (QRA) of pressurised pipelines is calculating the probability of loss of containment events. Such information is in turn employed to estimate the individual and social risk levels (Goodfellow et al., 2012) forming the basis for appropriate control and emergency mitigation planning.

Given that the failure hole size directly affects the magnitude of failure consequences and hence the results of QRA, a reliable technique for estimating the puncture size failure frequency must be established. The efficacy of such techniques is largely dependent on ensuring that a ‘sufficiently’ large number of real incident data points is available to be representative. This is however problematic in the case of CO₂ pipelines given their relatively low number. Another important issue to address is how such a probability distribution of CO₂ pipelines compares to that for hydrocarbon pipelines.

To obtain the puncture size probability distribution, a histogram using existing pipeline failure data is constructed by first segmenting the entire range of puncture sizes into a series of intervals (bins) and then counting how many values fall into each bin. Duncan and Wang (2014) employed the above technique to approximate the occurrence probability distribution of puncture diameters for CO₂ pipelines using the incident data from the Pipeline and Hazardous Material Safety Administration (PHMSA) database. In their study, puncture diameters ranging between 0 and 380 mm were divided into 6 bins. The analysis showed that the most prevailing puncture diameters were between

50 to 100 mm, whereas medium-sized punctures (150 to 200 mm) had the lowest probability of occurrence.

The resulting histogram can be parameterised and extended to a smooth probability distribution function. The validity of such functions is largely dependent on the size of the sample employed to derive the underlying histograms. Despite their usefulness, based on the review of the existing literature, methods to reliably handle ‘small’ samples sizes are not well-established.

Given the above limitation, in most risk assessment studies for pressurised pipelines, the puncture size is usually assumed to be a discrete variable as opposed to a continuous variable, as is the case in reality. In many of these studies, as shown below, only a limited number of representative puncture sizes are used to cover the whole size spectrum and as a result the predicted failure risk levels can only present rough estimations, rendering the subsequent strategies for risk mitigation uncertain.

Medina et al. (2012) for example, used only two representative pipeline puncture sizes of 10 and 40 mm and Full Bore Rupture (FBR) to calculate the expected cost of pipeline failure consequences for a risk-based optimisation of emergency shut down valve spacing for on-shore pipelines. Rusin and Stolecka (2015) on the other hand, used the same approach to calculate the frequency of the various failure modes for CO₂ pipelines for optimising inline emergency isolation valve spacing. In this study, the through-wall failure was simply assumed to be either puncture or rupture with the ratio of puncture/rupture occurrence probability taken as 9:1.

Considering the above limitations, this chapter presents the development of a statistical analytical technique for determining reliable failure hole size probability distribution for pressurised CO₂ pipelines using the limited historical failure data. The above involves a) using the Maximum Likelihood Estimator (MLE) to fit statistical distribution functions to historic failure data for estimating the unknown fitting

parameters that characterise these statistical distribution functions, and b) performing a Monte Carlo simulation test to assess the quality (statistical significance) of the MLE based on the data sample size. When the MLE ‘quality’ is low, a bootstrapping method, which can artificially inflate the sample size, is employed to calculate the MLE confidence intervals.

The chapter proceeds as follows. Section 4.2 commences with a brief introduction, filtering and processing of the pipelines failure historic data used for this study, followed by the description of the methodology employed to obtain a credible probability distribution of the puncture size. In Section 4.3, the ‘quality’ of MLE is first evaluated based on Monte Carlo simulation tests involving calculating the corresponding mean squared error of the MLE. Next, failure puncture size probability distributions derived from the filtered and processed historic fault data alongside the recommended fitting parameters for CO₂ pipelines are presented and compared against those for natural gas and crude oil pipelines. Conclusions are given in Section 4.4.

4.2 Methodology

4.2.1 Data Review

Several bodies collecting and publishing the failure statistics for CO₂ and hydrocarbon pipelines exist (e.g. Concawe, EGIG, PHMSA, UKOPA, see Section 2.2.2.2.1, Chapter 2) but few provide detailed information on the size of through-wall puncture. This study adopts the PHMSA database where such information is available. The failure puncture size, assumed to be oval, is expressed in terms of Equivalent Puncture Diameter (EPD) given by (Koch, 2008):

$$\text{EPD} = 1.55 \frac{A_p^{0.625}}{P_p^{0.25}} \quad 4.1$$

where A_p and P_p are respectively the oval puncture area and perimeter calculated based on the circumferential and longitudinal lengths of the puncture recorded in the database.

The PHMSA database holds data on the loss of containment incidents for federal- and state-regulated CO₂ and hydrocarbon pipelines operating in the US since 1970s. These incidents are documented in a very detailed manner, mainly including failure-specific information (e.g. incident year, incident pressure, failure mode), pipeline characteristics (e.g. pipe material, pipe diameter, fluid type), and operator details. Whilst the focus is on CO₂ pipelines, this study also examines natural gas and crude oil pipelines for comparison purposes.

In much of the databases spanning over 50 years, the records are of varying quality and level of detail for the various incidents. So, it is necessary to review and filter such data before use. The PHMSA updates its reporting criteria for pipeline incidents every 10 to 20 years for the past 5 decades. This study employs the data since 2010, when the reporting criteria were last updated to include both the longitudinal and circumferential measurements of the pipe opening in pipeline failure incidents. From 2010 to present, 6495 loss of containment incidents have been recorded but not all are relevant for this study for the following reasons.

First, a large proportion of the loss of containment incidents reported are for leaks from pipeline auxiliary equipment (e.g. relief valves, compressors, connectors) rather than those from the pipeline itself (i.e. pipe wall). Second, the failure puncture size information along with the pipe internal diameter is reported for selected incidents only. Accounting for the above limitations leads to a remaining total of 1906 useful EPD data points employed in the current work, covering CO₂, oil and gas pipelines.

4.2.2 Statistical Distribution Models

The probability distribution of a continuous variable is often expressed as the Cumulative Distribution Function (CDF). In this study, we employ the Weibull (Weibull, 1951) and lognormal distributions as the potential statistical functions to represent the CDF of the failure hole size. Both functions are widely used in reliability engineering for the assessment of pipeline failures (see for example Chaplin, 2015a; Goodfellow et al., 2012). Other possible distributions such as the gamma and exponential distributions have been used to a much lesser extent and hence are not considered here. The CDF of the Weibull distribution is reviewed in Section 2.2.2.3.2, Chapter 2 and is repeated below:

$$F(x) = \begin{cases} 1 - e^{-\left(\frac{x}{\alpha}\right)^\beta} & x \geq 0 \\ 0 & x < 0 \end{cases} \quad 4.2$$

The CDF of the lognormal distribution, also reviewed in Section 2.2.2.3.2, Chapter 2, is once again presented:

$$F(x) = \frac{1}{2} + \frac{1}{2} \operatorname{erf}\left(\frac{\ln x - \mu}{\sigma\sqrt{2}}\right) \quad 4.3$$

where erf is the error function which is defined as:

$$\operatorname{erf}(x) = -\frac{2}{\sqrt{\pi}} \int_x^\infty e^{-t^2} dt \quad 4.4$$

4.2.3 Distribution Fitting

The selected failure puncture size sample data described in Section 4.2.1 are fitted to both Weibull and lognormal distributions to acquire the fitting parameters. The

Maximum Likelihood Estimator (MLE) is used for this purpose to best characterise the probability distribution of the sample data. The MLE is a widely adopted method for estimating the parameters of an assumed probability distribution for a given set of observed data, by finding the parameter values that will most likely generate the observed data. Mathematically, the MLE can be defined as:

$$\hat{\theta} \stackrel{\text{def}}{=} \underset{\theta}{\operatorname{argmax}} F_L(\theta; X) \quad 4.5$$

where θ is the unknown parameter characterising the assumed probability distribution and $\hat{\theta}$ refers to the MLE of θ . X , denotes the data sample that contains n observations ($x_1, x_2, \dots, x_i, \dots, x_n$) of the data population. F_L , on the other hand, is called the likelihood function which calculates the product of the probability densities of each value in X , mathematically expressed as:

$$F_L(\theta; X) = \prod_{i=1}^n f(x_i; \theta) \quad 4.6$$

In essence, the process of maximum likelihood estimation is to find the estimator that maximises the likelihood function (equation 4.6).

According to Ginos (2009), the MLE is among the most dependable statistical estimators for parameter estimation. Some appealing features of the MLE include it being consistent, efficient, and asymptotically normal (Ji, 2020; Long and Freese, 2006). However, these properties have been only proven to hold if the number of data being used in the estimation process approaches infinity (Ji, 2020). This is an issue in the case of CO₂ pipelines, where relatively small sample sizes are available thus limiting the applicability of MLE for the present study. Given this, whether the sample size can suffice for a high-quality MLE needs to be determined.

Eliason (1993) suggested a sample size of more than 60 is usually large enough for estimating no more than 5 parameters using MLE. Long and Freese (2006) on the other hand, suggest it is risky to use MLE with sample sizes smaller than 100, while sample sizes over 500 are presumed adequate. However, most of the literature dealing with MLE do not provide specific sample size guidelines. In general, there are no rules of thumb, and the appropriate sizes heavily depend on the question at hand.

In this study, to determine the appropriate sample size, the MLE quality is assessed by examining the mean squared error which is the averaged square difference between the estimated and the actual values (Ryan, 2007). The use of mean squared error is very common in the study of MLE (see for example Ginos, 2009; Nielsen, 2011), and it is considered an excellent general-purpose error metric for numerical predictions (Neill and Hashemi, 2018). Mathematically, the mean squared error of the MLE, $\hat{\theta}$ to an unknown parameter, θ is defined as the addition of the variance and bias squared:

$$\text{MSE}(\hat{\theta}) = \text{Variance}(\hat{\theta}) + \text{Bias}^2(\hat{\theta}, \theta) \quad 4.7$$

where MSE denotes the mean squared error. The variance and bias are respectively given by:

$$\text{Variance}(\hat{\theta}) = E \left[(\hat{\theta} - E[\hat{\theta}])^2 \right] \quad 4.8$$

$$\text{Bias}(\hat{\theta}, \theta) = E[\hat{\theta}] - \theta \quad 4.9$$

where, E denotes the expected value.

In the present study, Monte Carlo simulation tests are performed to investigate the quality of MLE based on computing the mean squared errors for different sample sizes.

The tests involve, i) determining the Weibull and lognormal distribution parameters and sample sizes being tested; ii) for a given sample size, N , calculating the corresponding MLE using N data randomly sampled from the Weibull and lognormal distributions determined in step i); iii) repeating step ii) for a sufficiently large number of times (typically over 1,000 times) and computing the corresponding mean squared error.

4.2.4 Determination of Probability Distribution

Following the above Monte Carlo simulation tests, the sample size sufficing for a high-quality MLE is obtained. For sufficiently large samples, the resulting high-quality MLE can be used with confidence to characterise the probability distribution of the failure hole size. However, given that two distribution models (i.e. Weibull and lognormal) are employed in this study, the one-sample Kolmogorov-Smirnov (K-S) goodness-of-fit test (Kolmogorov, 1933) involving comparing the sample data with the predictions of both models is further employed to determine which model provides a statistically better fit representing the sample population.

The test process involves, i) specifying a null hypothesis; ii) computing the K-S statistic and critical value at a chosen significance level and iii) accepting the null hypothesis if the K-S statistic is smaller than the critical value or rejecting the null hypothesis if otherwise.

The K-S statistic is computed based on quantifying the greatest vertical distance between the empirical CDF (the sample data) and the CDF of the reference distribution, that is (Conover, 1999):

$$D = \sup_x |F_n(x) - F(x)| \quad 4.10$$

where, D is the K-S statistic. \sup stands for supremum which means the greatest value. $F_n(x)$, on the other hand, is the empirical CDF for n ordered sample data points

$(x_1 < x_2 < \dots < x_n)$, which is a step function jumping up by $1/n$ at each of the n data points.

The critical value, on the other hand, is usually determined using a K-S test critical value table, which can be easily obtained from several literatures, such as Massey Jr (1951). In particular, for $n \geq 40$, the critical value is computed based on a specific equation depending on the chosen significance level. In the current study, a significance level of 0.01 is chosen for the K-S test and the corresponding equation for calculating the critical value is given by:

$$\text{Critical value} = \frac{1.63}{\sqrt{n}} \quad 4.11$$

To deal with the small sample sizes, the bootstrapping method, which can artificially inflate the sample size by random sampling with replacement is employed to calculate the MLE confidence interval. The methodology was first introduced by Efron (1979) for making inferences from data without making strong distributional assumptions and was later employed by many authors for enhancing the confidence in using MLE when the sample size is too small. Wei and Li (2019), for example, presented a bootstrapping estimation for Weibull distribution parameters using samples containing only 10 to 30 data points. Tsagkanos (2008), on the other hand, developed a bootstrapping enhanced MLE for improving the accuracy of the classical MLE for Logit model in the presence of small samples. Unlike the case for sufficiently large samples where a single value of the MLE is acquired, the bootstrapping process produces a range of values where the MLE is expected to lie. It should be noted that for small samples which may not be statistically representative of the population being considered, the aforementioned K-S test cannot accurately reflect the goodness-of-fit between the model predictions and the data. Given this, the probability distributions derived based on either Weibull or lognormal models are considered statistically valid for the purpose of this study if the

bootstrapping method is employed.

The bootstrapping process for calculating the confidence interval of the MLE is shown in figure 4.1.

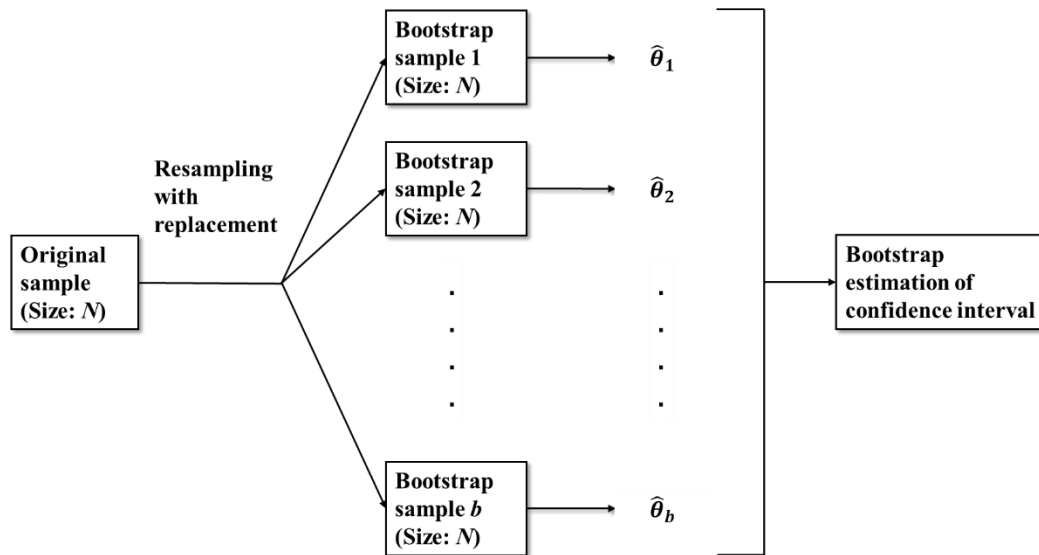


Figure 4.1: Schematic description of the steps in the bootstrapping process for calculating the confidence interval of the MLE (Haukoos and Lewis, 2005).

The bootstrapping process comprises the following steps. First, the bootstrap samples are generated. This involves resampling the original data sample with replacement to create a resampled dataset (also known as a bootstrap sample) that have the same size (N) as the original sample. Second, the MLE of each bootstrap sample is computed based on equations 4.6 and 4.7. Third, the above first and second steps are repeated for a sufficiently large number of times to obtain a distribution for the possible values of the MLE. Fourth, the MLE confidence interval is calculated based on the distribution obtained from the third step.

For the fourth step, several options including the normal approximation method, percentile method, bias-corrected method etc. can be adopted to calculate the MLE

confidence interval. In this study, the percentile method, which is considered suitable for small samples (Jung et al., 2019; Wei and Li, 2019), is employed. The MLE confidence interval based on the percentile method can be given as follows (Jung et al., 2019):

$$[\hat{\theta}_{\text{lower limit}}, \hat{\theta}_{\text{upper limit}}] = [\hat{\theta}_j, \hat{\theta}_k] \quad 4.12$$

where j and k respectively refer to the j th and k th quantiles of the collection of the possible MLE values ordered from lowest to highest. Here, j and k are respectively:

$$j = \frac{\alpha_s}{2} \times B \quad 4.13$$

$$k = \left(1 - \frac{\alpha_s}{2}\right) \times B \quad 4.14$$

where α_s is the level of significance and B is the number of bootstrap samples generated in the bootstrapping process.

4.3 Results and Discussion

4.3.1 Monte Carlo Simulation Results

4.3.1.1 Simulation Setup

In this section, four tests following the Monte Carlo simulation steps described in Section 4.2.3 are performed. Based on investigating several assumed distributions, tests 1 to 4 respectively examine the MLE quality as a function of sample size for Weibull scale parameter, Weibull shape parameter, lognormal mean, and lognormal standard deviation (see equations 4.3 and 4.4). Each test examines three pairs of parameters

varying the value of the tested parameter whereas fixing that of the non-tested parameter. The chosen values of the parameters for the four tests are summarised in table 4.1. These investigated values are selected given the fact that small pipeline punctures are far more frequent than ‘large’ ruptures (Lydell, 2000).

For each pair of examined parameter values, the mean squared error of the MLE is calculated for a wide range of sample sizes, $N = 10, 20, \dots, 100, 200, \dots, 500$. The following details how the Monte Carlo simulation steps described in Section 4.2.3 are implemented for a give N .

First, N data are randomly selected from the distribution characterised by the examined value pair using a random value generator. Second, using the selected N data, the MLE to the examined parameter is computed based on equations 4.5 and 4.6. Third, in order to accurately approximate the mean squared error of the examined MLE, 10,000 MLEs to the examined parameters are generated by repeating the above steps. The mean squared error of these MLEs is then computed based on equation 4.7.

The above process is executed for each investigated sample size. The resulting mean squared errors are then plotted against the corresponding N . As such, a figure showing the variation of the MLE mean squared error as a function of the sample size is obtained.

Table 4.1: Weibull and lognormal distribution parameter values examined in the four Monte Carlo simulation tests for investigating the quality of MLE.

Test no.	Distribution	Tested parameter	Non-tested parameter
1	Weibull	Scale parameter, $\alpha = 1, 1.5, 2$	Shape parameter, $\beta = 2$
2	Weibull	Shape parameter, $\beta = 1.5, 2, 2.5$	Scale parameter, $\alpha = 1$
3	Lognormal	Mean, $\mu = 0, 0.5, 1$	Standard deviation, $\sigma = 1$
4	Lognormal	Standard deviation, $\sigma = 1, 1.5, 2$	Mean, $\mu = 0.25$

4.3.1.2 Simulation Results

Figure 4.2 presents the simulation results for tests 1 to 4 described in Table 4.1, respectively showing the variations of the MLE mean squared error as a function of the sample size for the Weibull scale parameter, Weibull shape parameter, lognormal mean, and lognormal standard deviation. Figure 4.3 on the other hand shows the same results plotted in logarithmic scale to aid visualisation.

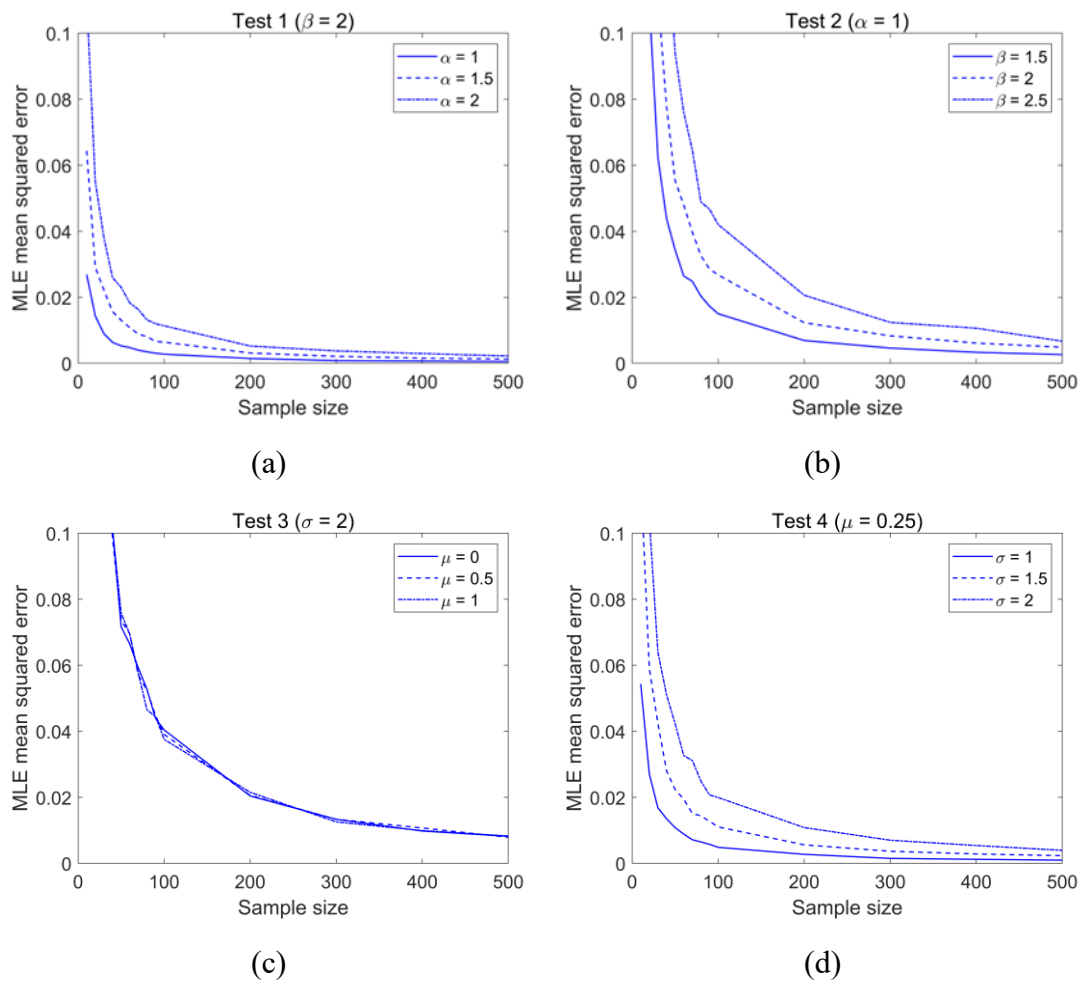


Figure 4.2: Simulation results for tests 1 to 4 described in Table 4.1 showing the variations of the MLE mean squared error as a function of the sample size, N for the Weibull scale parameter (a), Weibull shape parameter (b), lognormal mean (c), and lognormal standard deviation (d).

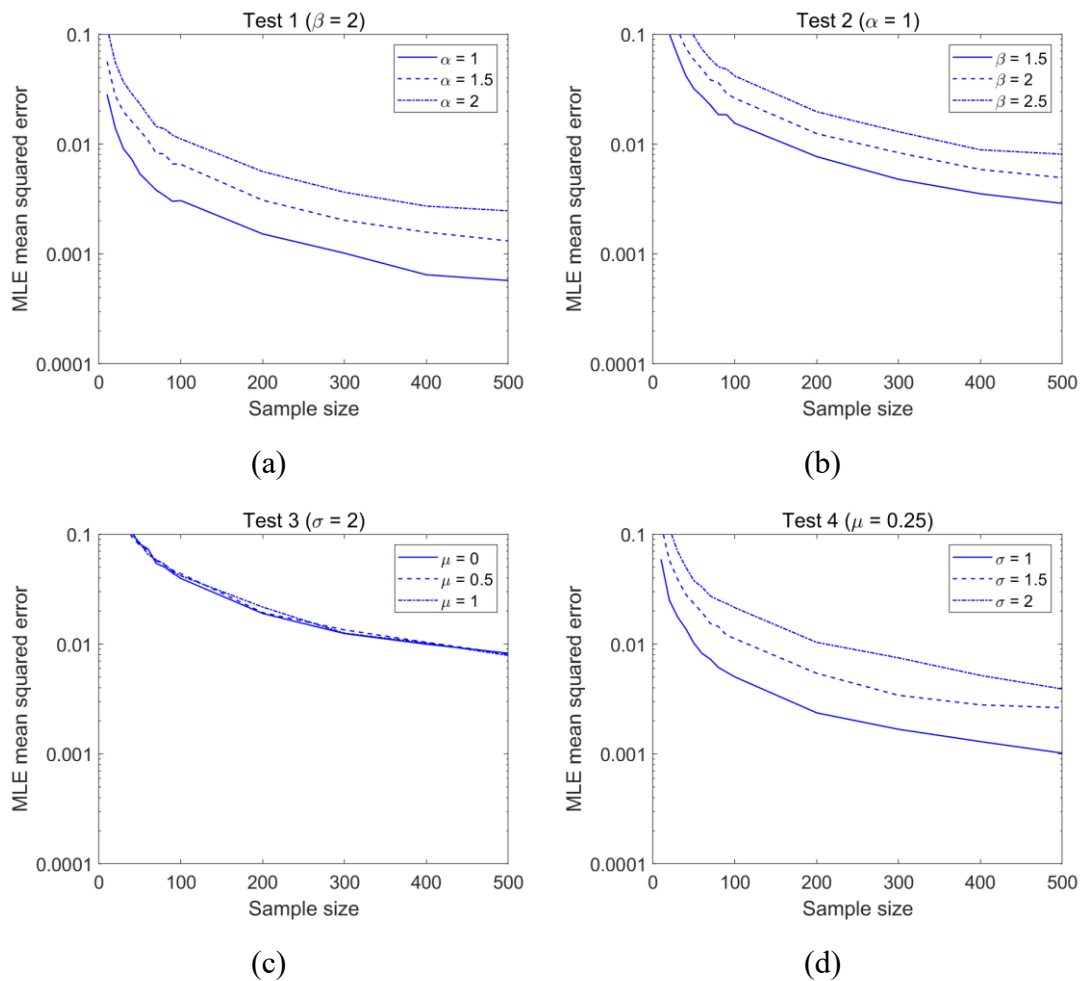


Figure 4.3: Simulation results for tests 1 to 4 presented in Table 4.1 showing the logarithmic variations of the MLE mean squared error as a function of the sample size, N for the Weibull scale parameter (a), Weibull shape parameter (b), lognormal mean (c), and lognormal standard deviation (d).

As may be observed from both figures 4.2 and 4.3, three distinct regions for the behaviour of the mean squared error variation with sample size may be identified. Initially, when the sample size is smaller than ca. 100, the mean squared error drops significantly indicating that the MLE quality is highly sensitive to the sample size and therefore the MLE should be used with caution in this region. At sample sizes between 100 to 200, the rate of decrease in mean squared error slows down, indicating that using samples with more than 100 data points will substantially improve the MLE quality. In

the third region where the sample size surpasses 200, the rate of decrease in mean squared error further slows down, meaning that further increasing the sample size provides limited improvement in the MLE quality.

The above indicates that the minimum acceptable sample size sufficing for acquiring a reliable MLE is at least 100 while with ideally more than 200 data points, sufficiently reliable statistical representation of the puncture size data population may be obtained.

Figure 4.3 provides a closer look at the mean square error for large sample sizes. Here, for all tested parameters, the mean squared error drops almost linearly when the sample size is increased from 100 to 200, suggesting minimal marginal increase in the MLE quality. When the sample size exceeds 200, the mean squared error tends to converge between the 0.001 to 0.01 range, again indicating that further increasing the sample size provides limited improvement in the MLE quality. This further strengthens the conclusion drawn from Figure 3 that 100 is the minimum acceptable sample size sufficing for acquiring a reliable MLE while more than 200 is ideal.

4.3.2 Failure Size Probability Distribution Results

The following section presents the application of the methodology presented in Section 4.2 to obtain the probability distribution of the equivalent puncture diameter data from the PHMSA database (PHMSA, 2020). Here, the 1906 data points (see Section 4.2.1) are divided into three groups based on the pipeline inventories, covering natural gas, crude oil, and CO₂. The corresponding failure data counts, and parameter estimation methods determined based on the results of the Monte Carlo simulation tests as described in Section 4.2.3 are summarised in table 4.2.

Table 4.2: Summary of the failure data counts from the PHMSA database and parameter estimation methods employed for deriving the probability distributions of the relative hole diameter for natural gas, crude oil, and CO₂ pipelines.

Pipe inventory	Failure count	Parameter estimation method
Natural gas	1072	MLE with K-S test
Crude oil	816	MLE with K-S test
CO ₂	18	MLE with bootstrapping

As can be observed from Table 4.2, the failure counts for both natural gas and crude oil pipelines exceed the minimum acceptable sample size (i.e. 100; see Section 4.3.1.2) for acquiring a reliable MLE. As a result, their puncture size probability distribution parameters can be estimated confidently using MLE and therefore a further bootstrapping step is not necessary. For CO₂ pipelines on the other hand, the corresponding failure count of 18 is far less than the 100 threshold and therefore the bootstrapping technique is employed to enhance the MLE confidence.

4.3.2.1 Natural Gas Pipelines

Figure 4.4 presents the comparison of the variation of the cumulative failure probability versus equivalent puncture diameter for the field data against the predictions by the Weibull and lognormal Cumulative Distribution Functions (CDFs) for natural gas pipelines. The parameters for the Weibull and lognormal CDFs and the corresponding K-S test results including the null hypotheses, K-S test statistics and critical values are summarised in table 4.3. The critical value used for accepting or rejecting the null hypothesis in the K-S test (see Section 4.2.4) is calculated using equation 4.11.

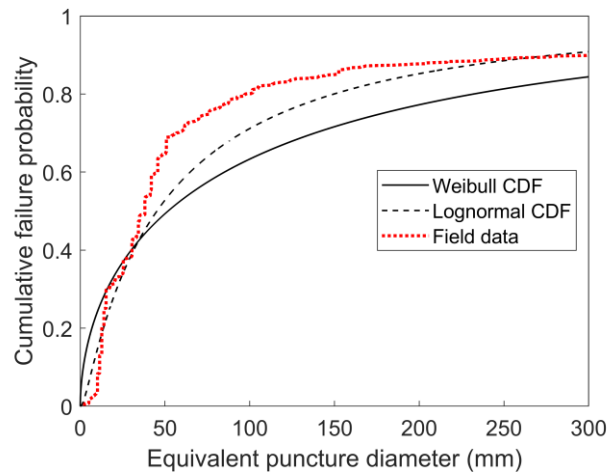


Figure 4.4: Comparison of the variation of cumulative failure probability versus equivalent puncture diameter for the field data (data points) against predictions by the Weibull (solid line) and lognormal (dashed line) CDFs for natural gas pipelines.

Table 4.3: Summary of the parameters of the predicted Weibull and lognormal CDFs and the corresponding K-S test results including the null hypotheses, K-S test statistics and critical values for natural gas pipelines.

Distribution	Parameter	Value
Weibull	Scale parameter, α	99.475
	Shape parameter, β	0.562
	Null hypothesis	“Data are from a Weibull distribution.”
	K-S statistic	0.213
	Critical value	0.053
Lognormal	Mean, μ	3.812
	Standard deviation, σ	1.422
	Null hypothesis	“Data are from a lognormal distribution.”
	K-S statistic	0.173
	Critical value	0.053

The K-S test results in Table 4.3 show that the K-S statistics for both Weibull and lognormal CDFs are greater than their critical values, meaning the null hypotheses are rejected (see Section 4.2.4). This indicates that both CDFs are not statistically good fits to the field data. However, visually, the lognormal CDF appears to be a better fit overall as it more closely mirrors the recorded data throughout. The lognormal CDF can hence be recommended to represent the probability distribution of the equivalent puncture diameter for natural gas pipelines, with the lognormal mean and standard deviation respectively being 3.812 and 1.422.

As can be observed from the recommended Weibull CDF in figure 4.4, as the equivalent puncture diameter increases, the rate of increase in the cumulative failure probability generally slows down. The steepest rise is observed when the equivalent puncture diameter increases from 0 to ca. 100 mm, meaning that relatively smaller punctures have a higher probability of occurrence for natural gas pipeline failures. Specifically, around 70% of such failures are in the form of punctures smaller than 100 mm. On the other hand, punctures smaller than 50 mm account for ca. 45% of the failures while those equal to or over 150 mm only account for 20%.

4.3.2.2 Crude Oil Pipelines

Figure 4.5 shows the comparison of the variation of the cumulative failure probability versus equivalent puncture diameter for the field data against the predictions by Weibull and lognormal CDFs for crude oil pipelines. The parameters of the Weibull and lognormal CDFs and the corresponding K-S test results including the null hypotheses, K-S test statistics and critical values are summarised in table 4.4. The critical value used for accepting or rejecting the null hypothesis in the K-S test (see Section 4.2.4) is calculated using equation 4.11.

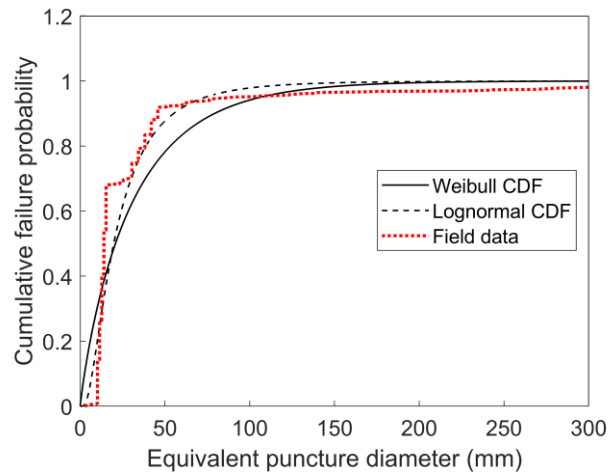


Figure 4.5: Comparison of the variation of cumulative failure probability versus equivalent puncture diameter for the field data (data points) against predictions by Weibull (solid line) and lognormal (dashed line) CDFs for crude oil pipelines.

Table 4.4: Summary of the parameters of the predicted Weibull and lognormal CDFs and the corresponding K-S test results including the null hypotheses, K-S test statistics and critical values for crude oil pipelines.

Distribution	Parameter	Value
Weibull	Scale parameter, α	1.259
	Shape parameter, β	0.777
	Null hypothesis	“Data are from a Weibull distribution.”
	K-S statistic	0.284
	Critical value	0.073
Lognormal	Mean, μ	2.984
	Standard deviation, σ	0.801
	Null hypothesis	“Data are from a lognormal distribution.”
	K-S statistic	0.065
	Critical value	0.073

As can be seen from figure 4.5, in general both Weibull and lognormal data show good agreement with the field data. However, the K-S test results in table 4.4 suggest differently. The K-S statistic for the test of Weibull distribution is greater than the critical value while that for the test of lognormal distribution is otherwise smaller. This means that the null hypothesis for Weibull distribution is rejected while that for lognormal distribution can be accepted. The above indicates that the data are more likely to be drawn from the lognormal CDF. Visually, the lognormal CDF more closely follows the field data covering the most prevalent pipeline failures (equivalent puncture diameter < 100 mm, accounting for ca. 90% of the failures), whence best represents the probability distribution of the equivalent puncture diameter for crude oil pipelines, with the lognormal mean and standard deviation respectively being 2.984 and 0.801.

Comparing to the recommended failure CDF for natural gas pipelines (see figure 4.4), it is obvious that the equivalent puncture diameter is more concentrated at smaller values (< 100 mm) in the corresponding CDF for crude oil pipelines, indicating that small punctures are more frequent in crude oil pipelines. This may be attributed to the fact that in the PHMSA database records, more natural gas pipeline failures are initiated by mechanisms (e.g. excavations and natural forces) that are more likely to result in catastrophic failures.

4.3.2.3 CO₂ Pipelines

In the case of CO₂ pipelines, only 18 equivalent puncture diameter data (see table 4.2) are available; far less than the 100 sample size threshold required for obtaining a reliable Maximum Likelihood Estimator (MLE) (see Section 4.3.1.2). The bootstrapping method described in Section 4.2.4 is therefore employed to calculate the MLE confidence interval. To specify, the bootstrapping process which involves creating resampled datasets that have the same size as the original one, is first implemented to generate a number of bootstrap samples for CO₂ pipelines, each containing 18

equivalent puncture diameter data points. The resampling is performed with replacement and thus the resulting bootstrap samples may or may not be identical to the original dataset. To ensure that a sufficiently large number of the possible bootstrap samples are accounted for, 20,000 iterations of the resampling of the original dataset are carried out, corresponding to 20,000 bootstrap samples. Once all the bootstrap samples are obtained, the data points for each bootstrap sample are fitted to both Weibull and lognormal distributions following the distribution fitting process based on equations 4.5 and 4.6. The resulting 20,000 MLEs are then segmented into 50 equi-distance bins by their values to generate a distribution of the possible values of the MLE. Using the distribution, the corresponding confidence interval can then be calculated based on equation 4.12. The chosen level of significance, α_s for obtaining the confidence interval (see equations 4.13 and 4.14) is 0.05, corresponding to 95% confidence.

Figure 4.6 demonstrates an example bootstrapping result for the MLE of the lognormal mean, μ .

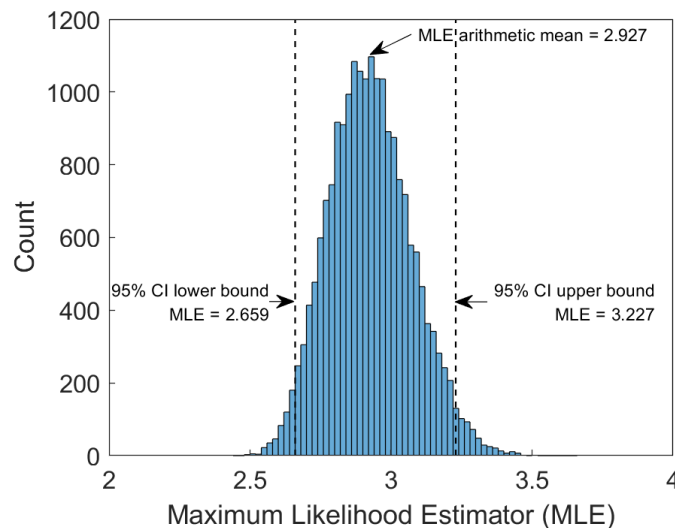


Figure 4.6: The bootstrapping result for the lognormal mean, μ , showing the Confidence Interval (CI) and arithmetic mean of the MLE.

As may be observed, the possible values of MLE are normally distributed, varying from ca. 2.5 to 3.5. The arithmetic mean of the MLE (i.e. the mean of the resulting normal distribution) is 2.927. The lower and upper bounds of the 95% confidence interval covering the majority of the possible values are respectively 2.659 and 3.227. Similar distribution of the MLE is also observed for the Weibull scale & shape parameters and the lognormal standard deviation. The corresponding arithmetic means and 95% confidence intervals of the MLEs for these investigated parameters are summarised in table 4.5.

Table 4.5: Summary of the arithmetic means and 95% confidence intervals (dashed lines) of the MLEs for the Weibull scale & shape parameters and the lognormal mean & standard deviation.

Distribution	Parameter	95% confidence interval	Arithmetic mean
Weibull	Scale parameter, α	[17.808, 36.976]	26.217
	Shape parameter, β	[1.171, 2.247]	1.559
Lognormal	Mean, μ	[2.659, 3.227]	2.927
	Standard deviation, σ	[0.354, 0.791]	0.593

The confidence intervals summarised in table 4.5 essentially represent the tolerable uncertainties in the prediction of the MLE. As such, any CDF characterised by the MLE in these intervals can be used with confidence to represent the probability distribution of the relative hole diameter for CO₂ pipelines.

Figure 4.7 presents the resulting Weibull and lognormal CDF ranges derived from these intervals showing the variation of the cumulative failure probability versus equivalent puncture diameter for CO₂ pipelines. The lower and upper bounds of the ranges are noted in the figure. The corresponding recommended CDFs for natural gas and crude oil pipelines (see respectively Sections 4.3.2.1 and 4.3.2.2) are also presented for

comparison purposes.

As discussed in Section 4.2.4, given that the sample size involved in deriving the above results is small, the K-S test cannot accurately reflect the goodness-of-fit between the model predictions and the data and hence, both Weibull and lognormal predictions are considered statistically valid for the purpose of this study.

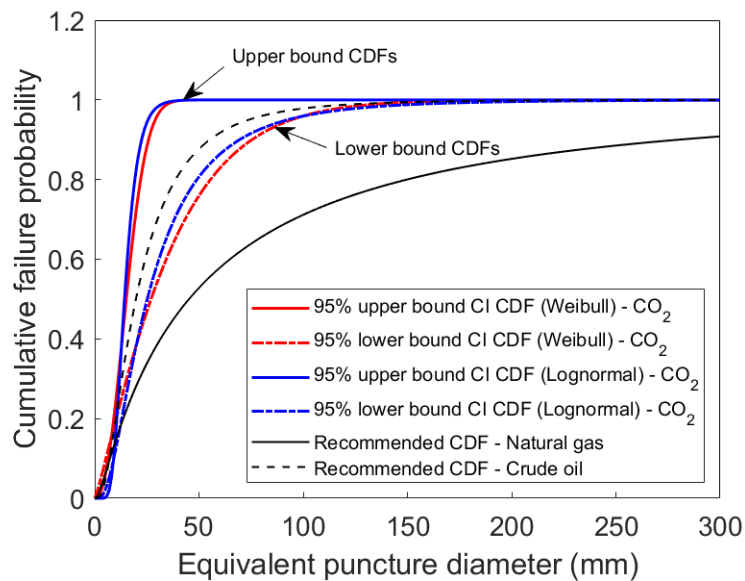


Figure 4.7: Weibull and lognormal CDF ranges derived from the Confidence Intervals (CIs) summarised in table 4.5 showing the variation of the cumulative failure probability versus equivalent puncture diameter for CO₂ pipelines. The corresponding recommended CDFs for natural gas and crude oil pipelines respectively obtained in Sections 4.3.2.1 and 4.3.2.2 are also presented for comparison purposes.

As can be observed from both lower and upper bound CDFs in figure 4.7, it is estimated that punctures smaller than 50 mm account for ca. 80% to 99% of the failures for CO₂ pipelines. In comparison, only ca. 45% of the failures for natural gas pipelines are in the form of punctures smaller 50 mm. The corresponding number for crude oil pipelines is ca. 90% which is lower than the upper bound value of the estimated range for CO₂

pipelines. The above suggests that small punctures are generally more common in CO₂ pipelines. This may be attributed to the fact that in the PHMSA database records, a major proportion of the CO₂ pipeline failures resulted from corruptions (internal and external) which are more likely to initiate small but continuous releases rather than catastrophic failures. The presence of even small amounts of water (ca. > 650 ppm; Connell, 2005) as a common impurity in CO₂ pipelines also makes them more prone to corrosion. It should be noted that the above conclusions are drawn based on the data currently being held in the PHMSA database. The pipelines from which these data were extracted were mostly constructed before 2010, some even dating back to several decades ago when the pipe construction criteria were different from current ones. While corrosion may remain a major failure cause for next generation CO₂ pipelines due to unavoidably the presence of corrosive impurities (e.g. water, H₂S) in the CO₂ stream, other failure mechanisms such as external interference and ground movement etc. which are likely to cause more catastrophic releases should not be ignored. With the expected growing number of deployed CO₂ pipelines, failures due to such external mechanisms may become increasingly dominant. In addition, the continued improvement in pipeline design standards, as well as cathodic protection techniques will render failures resulting from corrosion and material defects less probable. The above may change the puncture size profile for future CO₂ pipeline failures. Nevertheless, the technique developed here can serve as a powerful tool complimented with the growing wealth of failure data.

Using figure 4.7, decision makers can select from a range of credible CDFs based on their subjective preferences to represent the failure probability distribution of the equivalent puncture diameter for the design or/and risk assessment of CO₂ pipelines. For example, the lower bound CDF can be taken as the worst-case scenario CDF for determining the risks associated with CO₂ pipeline failures, as it represents the highest probability occurrence of larger puncture sizes among the possible CDFs. It should be

however noted that although the upper bound CDF is considered statistically valid, in practice, it is more reasonable to use the CDFs closer to the lower bound as they cover a wider range of puncture sizes, providing greater safety margins for quantitative risk assessment.

4.4 Concluding Remarks

The development of an analytical method for constructing credible probability distribution of the failure puncture size for CO₂ pipelines was described in this chapter. Based on the results and analysis presented, the following key conclusions of practical significance may be made:

- The results investigating the quality of the MLE determined by calculating the mean squared error as a function of the sample size indicated that a minimum of 100 puncture size data points proved to be adequate for obtaining a reliable MLE while 200 was ideal;
- The 1072 and 816 field data points of the equivalent puncture diameter for natural gas and crude oil pipelines were more than what was required for obtaining a high-quality MLE and therefore the K-S test was employed to decide which distribution model (Weibull or lognormal) provided a statistically better fit for representing the data. The results favoured the lognormal CDF parameterised by $\mu = 3.812$ and $\sigma = 1.422$ and the lognormal CDF parameterised by $\mu = 2.984$ and $\sigma = 0.801$ as the probability distributions of the equivalent puncture diameter for respectively natural gas and crude oil pipelines. Comparing the two CDFs showed that larger punctures tended to occur in natural gas pipelines. This was thought to result from the fact that a higher proportion of the gas pipeline failures is caused by outside forces which tended to lead to catastrophic failures;
- In the case of CO₂ pipelines, the 18 equivalent puncture diameter data points

available were far insufficient for obtaining a high-quality MLE and therefore the bootstrapping method involving computing the 95% confidence interval of the MLE was employed to obtain a credible range of the MLE. Remarkably, the resulting ranges of CDF suggested that as compared to hydrocarbon pipelines, CO₂ pipelines are more likely to experience smaller puncture size failures (at least 80% of the failures being in the form of punctures smaller 50 mm), thus resulting in smaller magnitude but more prolonged releases. This directly impacts the preventive and emergency response planning required especially in the case of buried CO₂ pipelines, where small leaks can remain undetected for long periods;

Despite being a continuous highly random variable, in practice, the through-wall puncture size in pressurised pipelines is often taken as a discrete variable meaning that only limited range of representative puncture sizes are selected thus compromising the validity of the subsequent quantitative risk assessment performed. The present study fills this important gap by introducing a method for accurately predicting the puncture size failure probability distribution by treating it as a continuous function.

Chapter 5: A Probabilistic Multi-Objective Optimisation Technique to Optimise the Emergency Shutdown Valve Configuration for Pressurised CO₂ Pipelines

5.1 Introduction

As pointed out in Chapter 1, inline Emergency Shutdown Valves (ESDVs) are extensively employed as a front-line mitigation tool for minimising the risk associated with the failure of pressurised CO₂ pipelines. Configuring the ESDVs along the pipe usually involves solving a corresponding Multi-Objective Optimisation (MOO) problem to determine the configurations that minimise the costs while reducing the risks to as low as reasonably practicable. The validity of such MOO studies heavily depends on the accuracy of the metrics used to define the hazard of pipeline failures. Given that uncertainties exist in pipe characteristics and operating conditions (e.g. failure hole size, failure location, fluid pressure), the failure scenario can vary greatly from one incident to the next, impacting the magnitudes of the failure consequences and the subsequent solution to the MOO problem.

Nevertheless, the metrics used in most of such studies (see for example Brown et al., 2014c; Yu et al., 2022) are relatively simple, that being the risk of a customised failure scenario (usually Full Bore Rupture (FBR) for representing the worse-case scenario).

Given the above, the ability to account for such uncertainties and hence the varying nature of the hazard at the time of pipeline failure is highly desirable for the optimisation of ESDV configurations for pressurised pipelines. Central to the above is the accurate prediction of the failure risk profiles based on calculating the probability of occurrence of possible failure scenarios and the associated consequences. However,

despite the importance, very few studies can be found on accounting for such uncertainties for CO₂ pipelines.

In a recent attempt, Rusin and Stolecka (2015) presented a risk-based optimisation study for optimising the number of safety valves along the pipe against the annual death rate levels following the failure of a 50 km length pipeline transporting CO₂ at 150 bar and 20 °C. In the study, uncertainties in the failure mode and valve availability were accounted for based on treating these parameters as probabilistic variables. The failure mode was assumed to be either rupture or puncture with their occurrence probabilities being taken as 1:9. The valve availability, expressed as the probability of the normal operation of safety valves, was assumed to be 0.99. However, except for the above, uncertainties in other essential parameters such as the operating pressure and temperature were not considered. In addition, given that the data employed to account for the parameter uncertainties are based on relatively simple assumptions, the validity of using such data for the subsequent optimisation study remains unclear.

In light of the above, this chapter presents the development and application of an MOO technique accounting for the uncertainties in the pipeline operational and failure parameters for selecting the optimal ESDV configurations for pressurised CO₂ pipelines. This involves describing such uncertainties using classical probability distribution models and performing a Monte Carlo simulation to obtain the probability distribution of the risk associated with pipeline failures. The technique is based on striking a balance between two important objective functions, namely the risk associated with CO₂ pipeline failure and ESDV costs.

The chapter is organised as follows. Section 5.2 starts with a brief description of the modelling of the parameter uncertainties using probability distribution models. This is followed by an introduction of the in-pipe fluid flow dynamics which accounts for the impact of valve closure dynamics. The modelling of the dispersion of the releasing CO₂

along with the resulting risks are then presented. The section ends with describing how the proposed technique can be employed to determine the optimal ESDV configuration for CO₂ pipelines. In Section 5.3, based on a case study for the design of a real Carbon Capture and Storage (CCS) project involving a 300 km length, 309.6 internal diameter (i.d.) pipeline transporting CO₂ at 129 bar and 287 K, the effectiveness of the proposed MOO technique is demonstrated based on calculating the probability distribution of the resulting risks following the failure of the said pipeline. Conclusions are presented in Section 5.4.

5.2 Methodology

5.2.1 Parameter Uncertainties

In this study, the uncertainties in several important pipeline operational and failure parameters are studied. The studied input parameters include the failure orifice size, failure pressure, fluid temperature, and ambient temperature. To account for their uncertainties, these parameters are treated as probabilistic variables. The Probability Density Functions (PDFs) representing the probability distribution for the possible values of each of the above parameters are hence defined. These variables are divided into three groups based on the probability distribution models employed.

Following the finding in Chapter 4, the Weibull distribution model (Weibull, 1951) which is extensively employed within reliability engineering can be adopted to model the probability distribution of the failure orifice size. Recalling Section 2.2.2.3.2, Chapter 2, the PDF of the Weibull distribution is once again presented here:

$$f(x) = \begin{cases} \frac{\beta}{\alpha} \left(\frac{x}{\alpha}\right)^{\beta-1} e^{-\left(\frac{x}{\alpha}\right)^{\beta}} & x \geq 0 \\ 0 & x < 0 \end{cases} \quad 5.1$$

To model both operating and ambient temperatures, whose values are practically default but with certain levels of variations, the normal distribution model taking account for the standard deviation of a mean value can be employed. The PDF of the normal distribution is reviewed in Section 2.2.2.3.2, Chapter 2 and is repeated below:

$$f(x) = \frac{1}{\sigma\sqrt{2\pi}} e^{-\frac{1}{2}\left(\frac{x-\mu}{\sigma}\right)^2} \quad 5.2$$

In practice, the failure pressure is dependent on the location of failure due to pressure drop along the pipe. The uncertainty in the failure pressure is therefore expressed as that of the failure location. In this study, it is assumed that the failure can occur anywhere along the pipe with uniform probability of occurrence. The continuous uniform distribution model where the value of the PDF remains constant throughout a given range of the random variable is therefore adopted to model the probability distribution of the failure location and hence the failure pressure. The PDF of the distribution model (reviewed in Section 2.2.2.3.2, Chapter 2) is given by:

$$f(x) = \begin{cases} \frac{1}{b-a} & a \leq x \leq b \\ 0 & \text{otherwise} \end{cases} \quad 5.3$$

5.2.2 Discharge Modelling

To describe the transient outflow following CO₂ pipeline failure, an extensively validated and computationally efficient 1-D outflow model accounting for the impact of the valve closure dynamics is employed. The details of this model are presented elsewhere (Mahgerefteh et al., 2000, 1997) and hence only a brief account is given here. The model assumes Homogeneous Equilibrium Mixture (HEM), where the constituent liquid and vapour phases are assumed to be at thermal and mechanical equilibrium. The resulting conservation equations of mass, momentum and energy are respectively given

by:

$$\frac{\partial \rho}{\partial t} + \frac{\partial}{\partial x} \rho u = 0 \quad 5.4$$

$$\frac{\partial \rho u}{\partial t} + \frac{\partial}{\partial x} (\rho u^2 + P) = -\frac{2\rho u^2 f_w}{D_{in}} \quad 5.5$$

$$\frac{\partial \rho E}{\partial t} + \frac{\partial}{\partial x} (\rho u E + P u) = -\frac{2\rho u^3 f_w}{D_{in}} + \dot{Q} \quad 5.6$$

where, ρ , u , E and P are respectively the fluid density, velocity, total specific energy, and pressure. D_{in} on the other hand, is the pipeline internal diameter. \dot{Q} denotes the fluid/wall heat transfer which is modelled using Newton's cooling law (reviewed in Section 2.1.2.4.2, Chapter 2). f_w refers the Fanning friction factor, which is determined using Chen's correlation (Chen, 1979) (reviewed in Section 2.1.2.4.1, Chapter 2).

The pertinent fluid thermal properties and phase equilibrium data for CO₂ are calculated using the Peng-Robinson Equation of State (PR EoS) (Peng and Robinson, 1976) following Teng et al. (2016b). The number of fluid phases presented in the flow during pipeline decompression is determined by the stability test based on the Gibbs tangent plane criterion (Michelsen, 1982). For two-phase flows, the fluid properties are handled based on the HEM assumption; that is, the pressure, temperature and velocity are identical across vapour and liquid phases. Other mixture properties including the heat capacity, specific volume, energy, and entropy are determined based on mass-averaged pure liquid and pure gas properties obtained from the PR EoS. The local speed of sound is handled based on the methods reviewed in Section 2.1.2.5.3, Chapter 2.

The above conservation equations 5.4 to 5.6 are solved numerically based on the method of characteristics (Hoffman and Zucrow, 1976), which is considered more

suitable than other numerical schemes (e.g. finite element method) in handling fast transient flows during pipeline decompression (Mahgerefteh et al., 1999). In this study, the flow prior to pipeline decompression is assumed to be isothermal steady state. The upstream and downstream ends of the pipe are assumed to be an infinite reservoir and closed, respectively.

The ESDVs installed along the pipe are modelled as Remote Control Valve (RCV) given its practically wide application in pipeline facilities (Oland et al., 2012). The modelling of RCV closure dynamics is presented as follows.

The area of the valve opening as a function of time, $A_f(t)$ assuming a constant closure rate is given by (Mahgerefteh et al., 1997):

$$A_f(t) = 2 \left[2\pi R_{in}^2 \cos^{-1} \left(\frac{R_{in} - \left(\frac{2R_{in} - x_v(t)}{2} \right)}{\frac{R_{in}}{360}} \right) - \left(R_{in} - \frac{(2R_{in} - x_v(t))}{2} \right) \left(\sqrt{R_{in}^2 - \left(R_{in} - \frac{(2R_{in} - x_v(t))}{2} \right)^2} \right) \right] \quad 5.7$$

where R_{in} is the pipe internal radius. x_v on the other hand, is the distance traversed by the valve at time t , which is determined by:

$$x_v = u_v t \quad 5.8$$

where u_v is the linear closure rate of the valve.

The pressure drop across the valve at any time t during closure, $P_v(t)$ is derived from (Mahgerefteh et al., 1997):

$$Q_v(t) = C_d(t)A_f(t) \sqrt{\frac{2\Delta P_v(t)}{\rho(t)}} \quad 5.9$$

where Q_v is the volumetric flow rate and C_d on the other hand, denotes the valve discharge coefficient which is a function of the valve type and degree of opening, given by (Wylie et al., 1993):

$$C_d = A_0 + A_1\omega_v + A_2\omega_v^2 + A_3\omega_v^3 + A_4\omega_v^4 \quad 5.10$$

where, ω_v represents the percentage of the valve opening area. A_0 , A_1 , A_2 , A_3 and A_4 are curve fitting constants and their values are given by: $A_0 = -0.00111888$, $A_1 = 0.001104507$, $A_2 = 8.13E-05$, $A_3 = -1.73E-06$ and $A_4 = 1.81E-08$.

The valve activation time, t_a is taken as the time lapsed for detecting the failure at the valve location plus the operator response/action time to initiate valve closure.

5.2.3 Dispersion Modelling

To predict the time-varying concentration of the dispersing CO₂ following the accidental release from pressurised pipelines, the steady-state SLAB model (Ermak, 1990) (see Section 2.2.2.1, Chapter 2) for simulating the atmospheric dispersion of dense-than-air releases is adopted. The model is developed based on solving a set of crosswind-averaged conservation equations of species, mass, momentum, and energy along with additional equations for cloud width and height. The concentration profiles in the crosswind direction are determined using the Gaussian distribution functions. The turbulent mixing of the dispersing gas cloud with the surrounding atmosphere is accounted for by using the air entrainment concept. The SLAB model simplifies the 3-D cloud dispersion through crosswind-averaged cloud properties which only vary in the downwind direction whilst calculating both cloud width and height. It therefore has the

advantage of low computational costs.

As input conditions for the SLAB model, the outflow data obtained using the model described in Section 5.2.2 are adopted.

5.2.4 Risk Estimation

In this study, the risk is defined as the annual human fatality due to CO₂ exposure following a given pipeline failure scenario. The procedure for calculating the fatality risk is summarised as follows.

First, the overall pipeline failure frequency, λ is calculated based on literature data. This involves multiplying the length of the pipe, L with its failure frequency per year per unit length, λ_0 , as given by:

$$\lambda = \lambda_0 L \quad 5.11$$

For CO₂ pipelines, λ_0 is assumed to be 2.3×10^{-4} per year per km (PHMSA, 2020), which is derived based on the historical failure data analysis method as given by equation 2.46.

Second, the Probit function, P_r measuring the probability of death as a function of the CO₂ dosage is calculated. For the risk of human fatality due to high CO₂ concentration, the Probit function is given in Section 2.2.2.3.1, Chapter 2 and is repeated below:

$$P_r = -90.80 + 1.01 \ln(C^8 t) \quad 5.12$$

Third, the annual human fatality, r following a given pipeline failure scenario is then calculated based on the population density of the area affected by the dispersing CO₂ cloud:

$$r = \int_A \lambda \rho_p P_d dA \quad 5.13$$

where A is the fatal cloud area affected by the dispersion of CO_2 and ρ_p is the population density within the fatal cloud area. P_d on the other hand, is the probability of death determined by the Probit value calculated based on equation 5.12.

5.2.5 Risk Probability Distribution

Due to the existence of uncertainties in the pipeline operational and failure parameters, the fatality risk is practically a probabilistic variable. To obtain the probability distribution of the fatality risk, a Monte Carlo simulation involving the random sampling of the input parameters described in Section 5.2.1 is performed. The Monte Carlo procedure can be summarised as follows.

Initially, a set of values of the input parameters representing one possible failure scenario are randomly generated based on the PDFs described in Section 5.2.1. This step simulates the practical situations where due to the existence of uncertainties in the input parameters, the pipe and fluid conditions are random at the time of pipeline failure. Using the set of values obtained above, the corresponding annual human fatality for the specific failure scenario is calculated following the procedure described in Sections 5.2.2 to 5.2.4. The above is repeated and terminated once a pre-determined iteration number, n representing the number of failure scenarios being simulated is reached.

The Monte Carlo procedure will give a set of n data points for the annual human fatality, $r_1, r_2, \dots, r_i, \dots, r_n$. Using the collection of these data points, the probability distribution of the fatality risk is then obtained based on deriving the corresponding Empirical Cumulative Distribution Function (ECDF), which is given by:

$$\hat{F}(x) = \frac{1}{n} \sum_{i=1}^n I(r_i, x) \quad 5.14$$

where $\hat{F}(x)$ represents the ECDF and I , on the other hand, denotes the indicator function which is given by:

$$I(r_i, x) = \begin{cases} 1 & \text{if } r_i \leq x \\ 0 & \text{if } r_i > x \end{cases} \quad 5.15$$

The ECDF is in essence the weighted count of samples, r_i for which r_i is below or equal to a threshold, x and therefore is an approximation of the real CDF. How accurate is the approximation depends on the number of failure scenarios, n being used to derive the ECDF. While it is obvious that a larger n can result in a better approximation, simulating the physical problem involved as described in Sections 5.2.1 to 5.2.4 can become increasingly computationally demanding. Hence, n must be carefully determined to ensure the result accuracy while minimising the computational workload.

To determine the appropriate n , the following test involving examining the quality of the ECDF for several values of n is performed. First, for a given n , the corresponding ECDF is derived based on equation 5.14 using the n data points randomly generated from an assumed test distribution. Second, the quality of the ECDF is assessed by the Doretzky-Kiefer-Wolfowitz inequality method. The method involves constructing a $(1 - \alpha)$ -confidence band as follows (Larry, 2004):

$$P_{CDF}(L(x) \leq F(x) \leq U(x) \text{ for all } x) \geq 1 - \alpha \quad 5.16$$

where $F(x)$ denotes the real CDF. α is the confidence level. P_{CDF} on the other hand,

refers to the probability of the real CDF lying between the lower, $L(x)$ and upper, $U(x)$ boundaries of the band which are respectively given by:

$$L(x) = \max\{\hat{F}(x) - \varepsilon, 0\} \quad 5.17$$

$$U(x) = \min\{\hat{F}(x) + \varepsilon, 1\} \quad 5.18$$

where:

$$\varepsilon = \sqrt{\frac{1}{2n} \log\left(\frac{2}{\alpha}\right)} \quad 5.19$$

The resulting confidence band represents that the probability of $F(x)$ lying between the $L(x)$ and $U(x)$ is greater than or equal to $1 - \alpha$. The width of the band, therefore, implies the quality of the ECDF in representing the real CDF.

5.2.6 Multi-objective Optimisation

In this study, the MOO problem examines two objective functions encompassing the ESDV cost and risk associated with CO₂ pipeline failure. For simplicity, the optimisation variable is taken as the number of ESDV, as it is considered one of the most important among all ESDV characteristics (Yu et al., 2022).

Following the above, the resulting MOO problem may be summarised in the mathematical form below:

$$\text{Min}_{d \in D} J_1(N), J_2(N) \quad 5.20$$

where N is the ESDV number and the objective functions, J_1 and J_2 are defined as

follows.

J_1 is the total annual cost of ESDVs, expressed as:

$$J_1(d) = \frac{V_{PN} \cdot r_d \cdot (1 + r_d)^{yr}}{(1 + r_d)^{yr+1} - 1} N \quad 5.21$$

where V_{PN} is the present net value of a single ESDV cost. r_d and yr are respectively the discount rate and average lifetime of the ESDV.

J_2 on the other hand, represents the risk associated with CO₂ pipeline failure, here taken as the annual human fatality due to CO₂ exposure, as described in Section 5.2.4. As such, J_2 is a probabilistic variable and the resulting solutions of the multi-objective optimisation problem become probabilistic as well.

Mapping the solutions based on the probability distribution of J_2 on the coordinate system set up by J_1 and J_2 , a probabilistic solution plane for selecting the optimal N will be constructed, from which the decision makers can determine a unique optimal solution according to their subjective preferences.

To investigate how the solutions obtained based on taking the risk as a probabilistic variable can be different from those obtained by assuming the risk as a deterministic variable, a comparative study is performed. This involves solving the same MOO problem based on otherwise treating the risk deterministically. Here, instead of deriving the risk probability distribution, the risk is simply assumed to be the annual human fatality following the FBR of CO₂ pipeline, representing the worst-case scenario. This is usually adopted in practice for an ESDV optimisation problem to account for the maximum safety margin when the information regarding the uncertainties in pipeline operational and failure parameters is not readily available.

5.3 Results and Discussion

5.3.1 Case Study

The case study is based on a proposed pipeline design for the GreenGen CCS project developed by China Huaneng Group (Gao et al., 2011). The project involves transporting 1.46 million tonnes per annum of CO₂ from GreenGen IGCC power plants in Tianjin to Shenli oilfield in Shandong, China for enhanced oil recovery. The 300 km length, 309.6 i.d. pipeline runs through several heavily populated provinces located in the east coast of China. Based on the population density data published by National Bureau of Statistics of China, the average population density in the proximity of the pipeline is assumed to be 620 person/km².

For all the simulations for the outflow from the pipeline, an automatic nested grid system applying finer numerical discretisation near the failure location is employed (Mahgerefteh et al., 1999).

Table 5.1 summarises the deterministic pipeline characteristics and prevailing conditions adopted to perform the simulations.

Table 5.1: Deterministic CO₂ pipeline characteristics and prevailing conditions used for the case study.

Parameter	Value
Pipe length (km)	300
Pipe external diameter (mm)	309.6
Pipe wall thickness (mm)	7.12
Pipe roughness (mm)	0.005
Pipe angle	Horizontal
Pipe elevation (m)	1
Heat transfer coefficient (kW/m ² K)	5
Feed composition (mole %)	CO ₂ 100
Pipe upstream condition	Reservoir (Constant pressure)
Feed flow rate (kg/s)	46.3
Feed pressure (bar)	153
Ambient pressure (bar)	1.01

The determination of the remaining necessary input parameters including the failure orifice size, failure pressure, fluid temperature and ambient temperature depends on how the risk is quantified (see Section 5.2.6). For the case where the risk is taken as a probabilistic variable, the method discussed in Section 5.2.1 is adopted to describe these parameters. Table 5.2 summarises the probability distribution models and the corresponding distributional parameters for modelling the uncertainties for these input parameters.

Table 5.2: Summary of the probability distribution models and the corresponding distributional parameters for the probabilistic CO₂ pipeline characteristics and prevailing conditions used for the case study.

Input parameter	Probability distribution model	Distribution parameter
Relative orifice size	Weibull	$\alpha = 0.137$ $\rho = 1.573$
Fluid temperature (K)	Normal	$\mu = 287$ $\sigma = 0.5$
Ambient temperature (K)	Normal	$\mu = 283$ $\sigma = 1.3$
Failure location (m)	Continuous uniform	$a = 0$ $b = 300$

Here, the failure orifice size is expressed in relative terms as the ratio of the failure orifice diameter to pipe internal diameter, termed as relative orifice size. The corresponding Weibull distribution parameters are selected to reflect the fact that among CO₂ pipeline failures, small punctures are statistically far more frequent than large ones (see Section 4.3.2.3, Chapter 4).

For the fluid temperature whose variations are usually a result of operational changes such as variations in flow rate, the normal distribution parameters are determined based on the project design in the case study. The fluid temperature is set at 287 K assuming ca. ± 1.5 K variations.

For the ambient temperature which could affect the heat transfer in/out the pipe, its normal distribution parameters are selected based on that it is assumed to have a default value of 283 K varying ca. ± 5 K.

The failure pressure, which refers to the fluid pressure at the point of failure, is

expressed in relation to that location. The uniform distribution parameters are obtained based on the length of the studied pipeline.

The resulting PDFs for the above discussed pipeline characteristics and prevailing conditions are presented in figure 5.1.

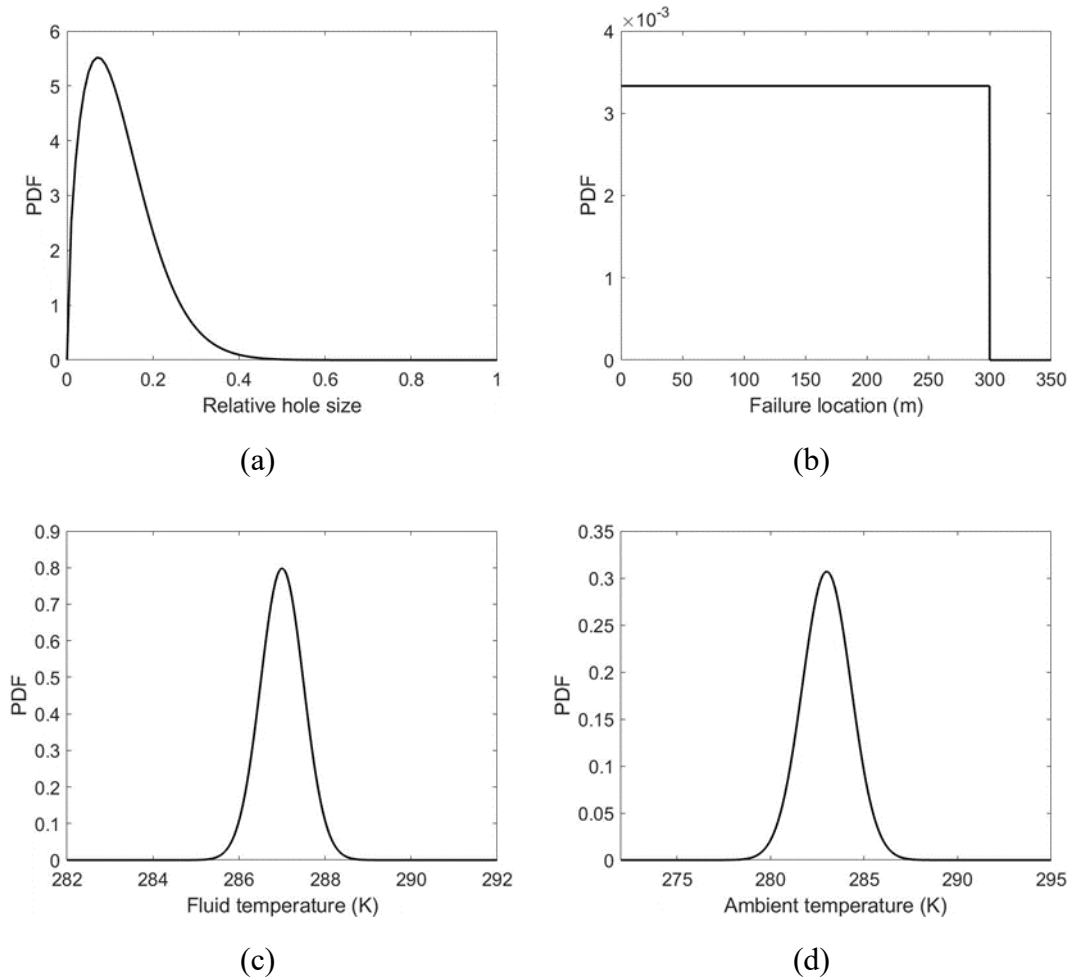


Figure 5.1: PDFs of the relative hole size (a), failure location (b), fluid temperature (c) and ambient temperature (d) used in the case study.

For the comparative study where the failure is assumed deterministically as an FBR, the undetermined input parameters are assumed to be fixed values taken from their respective PDFs from the above. The relative orifice size is taken as 1, representing FBR. The failure location is assumed to be the mid-length of the pipe. The fluid and

ambient temperatures on the other hand are taken as their default values.

To optimise the ESDV number, N for the pipeline in the case study, 11 different numbers varying from 0 to 10 are sampled for the MOO problem described in Section 5.2.6. For each ESDV number sampled, the corresponding ECDF representing the probability distribution of the risk following pipeline failure is obtained following the procedure described in Section 5.2.5. All the ESDVs are assumed to be RCV with a closure rate of 2.54 cm/s and activation time of 50 s. The single ESDV cost, V_{PN} , discount rate, r_d and average lifetime of each valve, yr (see equation 5.21) are respectively taken as £60,000, 0.035 and 10 years, following Yu et al. (2022). The ESDVs are assumed to be located at equal distance intervals. For comparison purposes, data obtained for the two objective functions, J_1 and J_2 are normalised before being fed into deriving the ECDF and the subsequent MOO problem. J_1 is normalised against the maximum cost among the sampled ESDV values, corresponding to 10 ESDVs, whereas J_2 is normalised against the annual human fatality based on the FBR of a pipeline without ESDVs.

5.3.2 Risk Probability Distribution Results

To determine the appropriate number of failure scenarios to be simulated, n for obtaining a reliable risk probability distribution, the test described in Section 5.2.5 involving examining the quality of the ECDF for several values of n is performed. The test distribution is assumed to be a Weibull distribution with the scale and shape parameters being respectively 0.25 and 1.5. A wide range of ns including 50, 100, 500, 1,000, 2,000, 3,000 are examined. The confidence level, α (see equation 5.16) for obtaining the confidence bands is set at 0.05. Figure 5.2 presents the resulting Weibull ECDF for each tested n , and the corresponding confidence bands measuring the quality of the obtained ECDF.

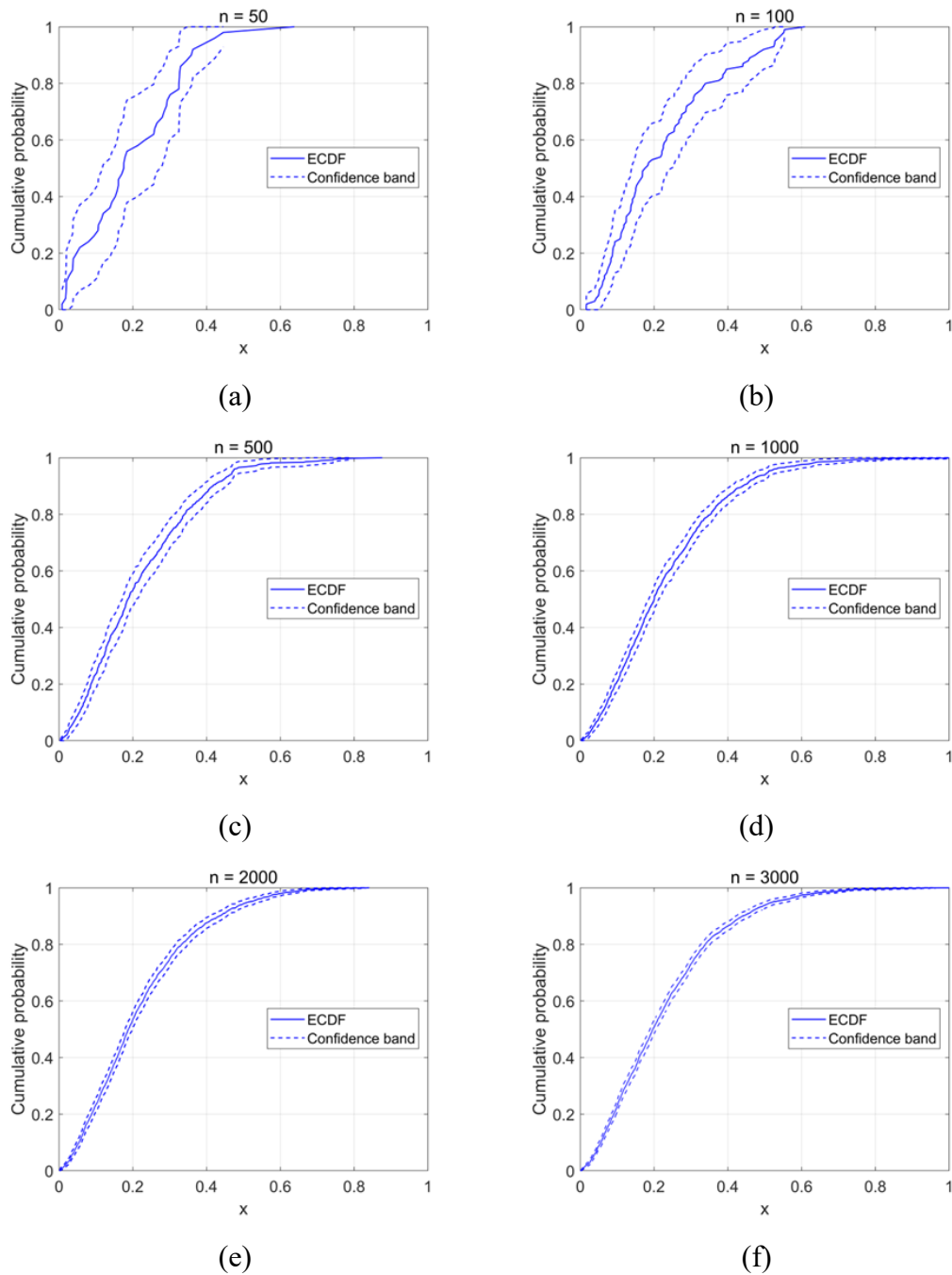


Figure 5.2: The Weibull ECDFs and the corresponding confidence bands for $n= 50$ (a), 100 (b), 500 (c), 1,000 (d), 2,000 (e), 3,000 (f).

As can be observed from figure 5.2, with the increase in n , the ECDF is gradually smoothed out and the confidence band generally shrinks, suggesting improved quality of the ECDF. However, the rate of shrinking is only significant when n is smaller than 500. As n further increases to 3,000, the marginal decrease in the width of the

confidence band decreases. The above means that beyond $n = 500$, further increasing n becomes increasingly unfavourable in obtaining the ECDF as it provides limited improvement to the quality of the ECDF while significantly increasing the computational workload. As such, the number of failure scenarios to be simulated is determined as 500 in this study for the subsequent process of obtaining the risk probability distribution.

Figure 5.3 presents the probability distributions (ECDFs) of the normalised annual human fatality, J_2 for the 11 different values of ESDV number, N (see Section 3.1) sampled for the multi-objective optimisation problem.

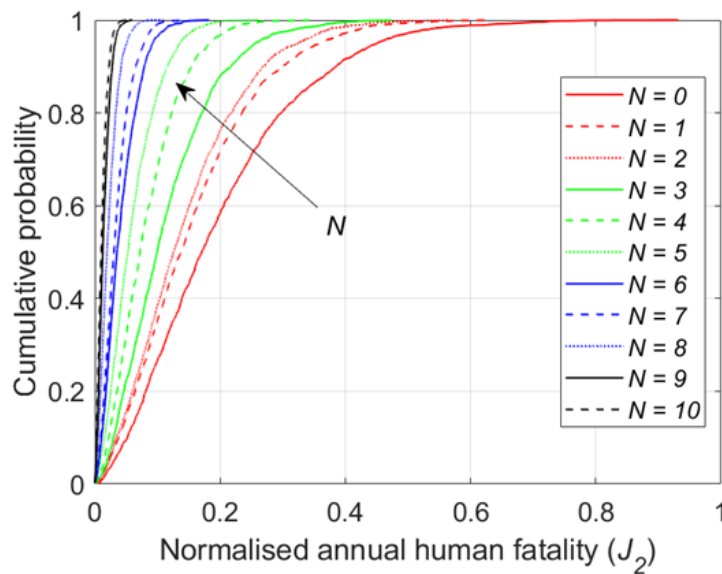


Figure 5.3: Probability distributions (ECDFs) of the normalised annual human fatality, J_2 for different ESDV numbers.

As can be observed, with the increase in N , the range of J_2 covered by the ECDF narrows down. As N increases from 0 to 10, the maximum J_2 value on the ECDF decreases from ca. 1 to merely ca. 0.07. This reflects the fact that increasing the number of ESDVs installed along the pipe will essentially help mitigate the risk associated with CO₂ pipeline failure, as expected.

It is otherwise noteworthy that even for the case of no ESDV ($N = 0$) where the corresponding ECDF covers a full range of J_2 (0 to 1), J_2 mostly concentrates at relatively small values, with ca. 80% of the J_2 smaller than 0.3 and over 90% smaller than 0.4. This indicates that the chance of the examined CO₂ pipeline experiencing catastrophic failures is statistically low. As such, the likelihood of a failure scenario, remains practically important for quantifying the corresponding risk and should be considered for the subsequent optimisation for selecting the optimal ESDV number.

5.3.3 Multi-objective Optimisation Results

Based on the risk probability distributions (ECDFs) from figure 5.3, mapping all the possible failure scenarios according to their cumulative probabilities on the coordinate system set up by the objective functions J_1 and J_2 , a probabilistic solution plane as described in Section 5.2.6 for the MOO problem for selecting the optimal ESDV number can be constructed. Figure 6 shows the constructed solution plane showing the variation of J_2 as a function of J_1 . For simplicity, only typical failure scenarios are selected to be shown in the figure. The coloured data points each represent a failure scenario with a unique set of J_1 and J_2 , with the corresponding cumulative probability being marked by the respective colour given in the vertical bar on the right.

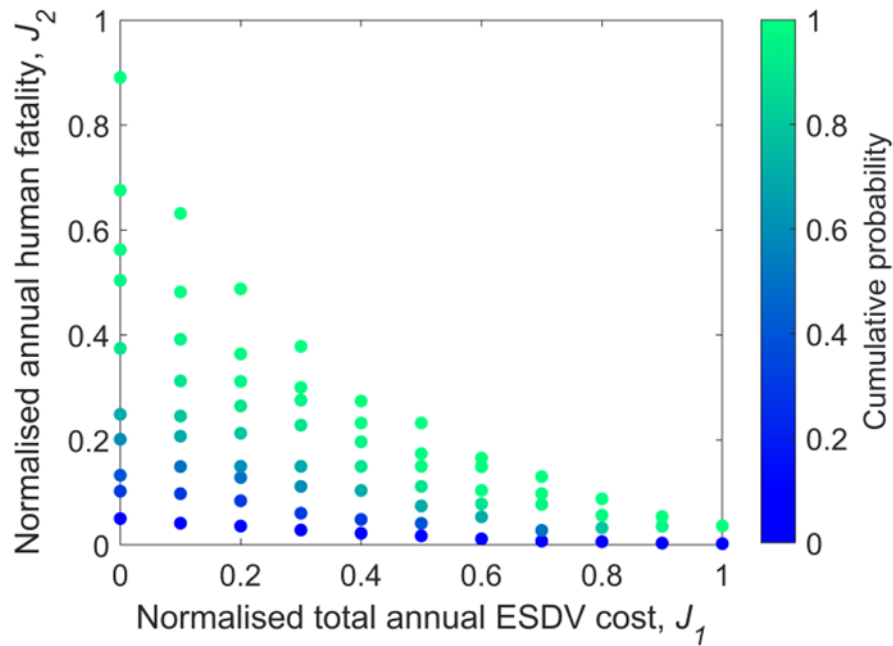


Figure 5.4: The constructed probabilistic solution plane for the MOO problem, showing the variation of the normalised annual human fatality, J_2 as a function of the normalised total annual ESDV cost, J_1 . The colour of each data point refers to the cumulative probability, as indicated in the vertical bar on the right.

In essence, the colour of a data point representing the cumulative probability of the corresponding failure scenario can be translated to indicate the likelihood of lowering the risk below a certain level of annual human fatality on a given ESDV budget. For example, the colour of the data point with $J_1 = 0.4$ and $J_2 = 0.2$ corresponding to ca. 0.9 on the vertical bar on the right means that the probability of limiting the risk lower than 0.2 using an ESDV budget equivalent to 0.4 is ca. 90%.

Based on the above, the following demonstrates how figure 5.4 is employed to help the decision makers select the optimal ESDV number based on their subjective preferences. An example preference is considered: the averaged normalised annual human fatality needs to be limited below the level of 0.15 over the lifetime of the pipe.

Figure 5.5 presents the MOO solution plane for selecting the optimal ESDV number,

N for the example decision makers' subjective preference focusing on limiting the averaged normalised annual human fatality, J_2 below the level of 0.15 over the lifetime of the pipe. The dashed horizontal line represents the 0.15 risk criterion. The expected values of J_2 on the respective normalised total annual ESDV costs, J_1 are also presented in the figure as references. The following discusses how the optimal N is determined.

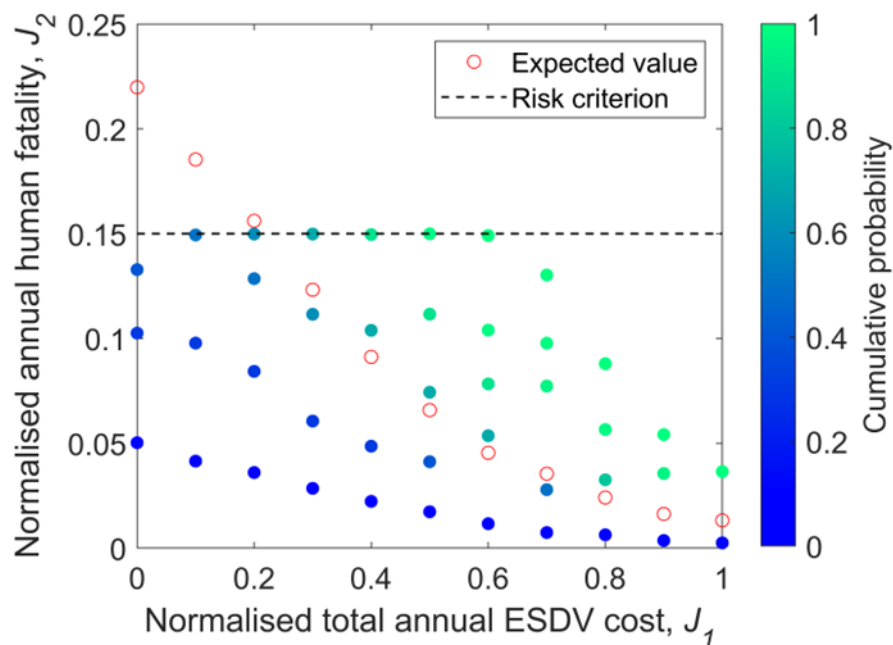


Figure 5.5: MOO solution plane for selecting the optimal ESDV number, N for the example decision makers' subjective preference focusing on limiting the averaged normalised annual human fatality, J_2 below the level of 0.15 over the lifetime of the pipe. The colour of each data point refers to the cumulative probability, as indicated in the vertical bar on the right.

First and foremost, to lower the averaged risk below the 0.15 criterion, at least the expected value of J_2 , which is derived based on pipeline quantitative risk assessment and hence represents the statistically desired risk outcome, should be lower than 0.15. It is obvious from figure 5.5 that this only applies when J_1 is equal to or greater than

0.3, suggesting that 3 or more ESDVs are the plausible solutions for meeting the decision makers' preference. Obviously, the above points to an optimal N of 3.

Nevertheless, analysing the corresponding cumulative probability for these plausible solutions, a different optimal solution may be obtained. To demonstrate, a further cost-effectiveness analysis examining the probability of limiting J_2 below 0.15 as a function of N is performed.

Figure 5.6 presents the results of the cost-effectiveness analysis showing the variation of the probability of limiting J_2 below 0.15 as a function of N for $N \geq 3$. Such probabilities are obtained based on the colours of the corresponding data points from figure 5.5.

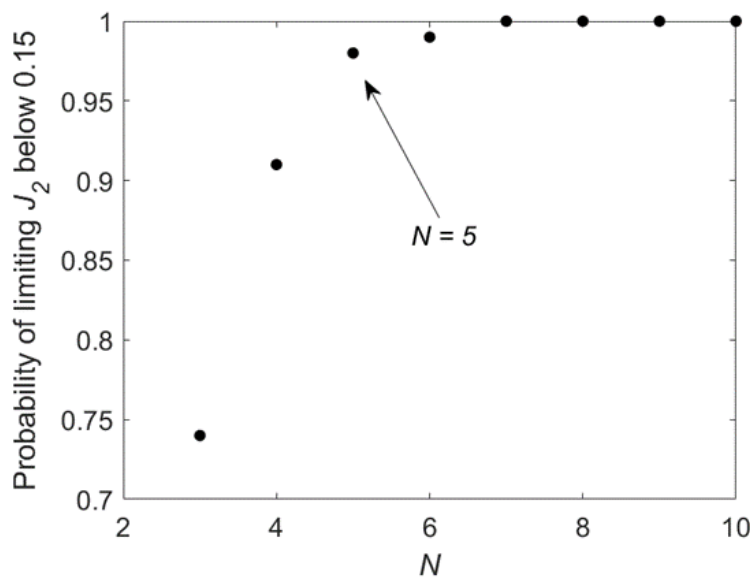


Figure 5.6: Cost-effectiveness analysis results showing the variation of the probability of limiting J_2 below 0.15 as a function of the ESDV number, N .

As can be seen from figure 5.6, the probability sharply increases from ca. 0.74 to 0.98 as N increases from 3 to 5 and turns almost plateaus afterward. This indicates that using more than 5 ESDVs can only lead to a minimal increase in the chance of limiting

the risk below the required level while substantially increasing the ESDV costs. As such, $N = 5$ is instead considered the optimal solution for the MOO problem.

An important finding from the above analysis is that even though the expected value represents the statistically desired risk outcome, the solution obtained based on such a value is actually not cost-effective from a statistical point of view.

5.3.4 Comparative Study Results

Figure 5.7 presents the MOO results showing the variation of the normalised fatality risk as a function of the ESDV number, N for the comparative study where the failure is taken deterministically as an FBR. Still, the preference of the decision makers is assumed to be the same as in Section 3.3, that being limiting the averaged normalised annual human fatality below the level of 0.15 over the lifetime of the pipe.

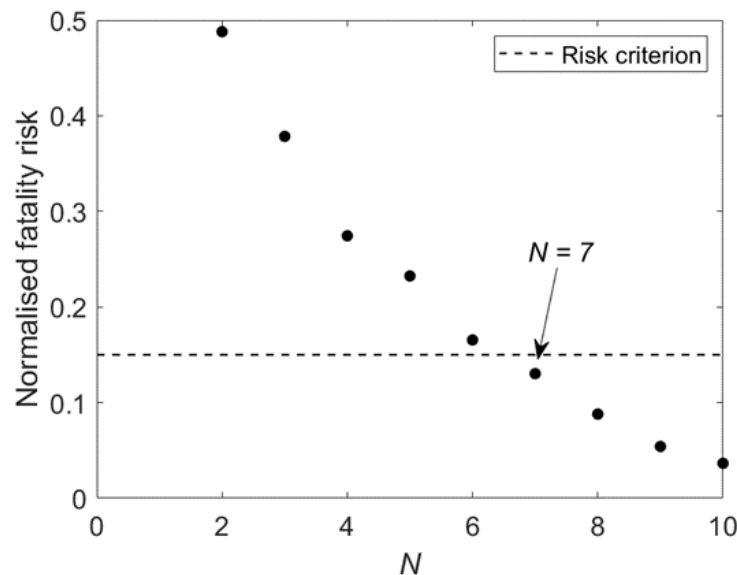


Figure 5.7: MOO results for the comparative study where the failure scenario is taken deterministically as an FBR.

As can be seen from figure 5.7, as N increases, the normalised fatality risk generally decreases as expected and passes through the 0.15 risk criterion line at $N = 7$. This

suggests that the optimal N for the MOO problem is 7, representing a 40% increase in the cost as compared to the results in Section 5.3.3 where 5 ESDVs are recommended. As discussed in Section 5.3.3, $N = 7$ is in essence a less favourable solution given its low cost-effectiveness from a statistical point of view. It is therefore clear that if the risk is otherwise considered deterministically as the worst-case scenario rather than a probabilistic variable, the resulting optimal ESDV number will be larger, leading to significantly more money being spent on the risk mitigation while minimally improving the mitigation effect.

5.4 Concluding Remarks

This chapter presents the development and application of an MOO technique for identifying the optimal inline ESDV number for pressurised CO₂ pipelines, accounting for the uncertainties in the pipeline operational and failure characteristics. Based on the studies presented in this chapter, the following significant findings that reveal the key capabilities of the proposed technique were found:

- The risk probability distributions showed that the majority of the CO₂ pipeline failures would only result in relatively small risks. The likelihood of a catastrophic CO₂ pipeline failure is practically small and will become increasingly minimal with the increase in the number of ESDVs installed along the pipe;
- The results of the MOO study revealed that the number of ESDVs installed along the pipe had a non-linear impact on the probability of limiting the risk below a decision-maker preferred level. There exists a threshold beyond which increasing the ESDV number provides little increase in the probability with substantially increased costs;
- The optimal ESDV number obtained based on the expected value of the risk is actually not cost-effective from a statistical point of view;

- The comparative research revealed that if in the MOO problem, the risk was taken deterministically as the worst-case scenario, the resulting optimal solution could be statistically less favourable. This finding proves the efficacy of the proposed MOO technique in minimising the costs while yielding minimal loss of mitigation impacts.

Chapter 6: Conclusions and Future Work

6.1 Conclusions

Carbon Capture Utilisation and Storage (CCUS) which involves capturing CO₂ and storing it in geological formations is considered to play a key role in decarbonising the power sector and heavy industries.

An essential part of the CCUS chain involves the large-scale transportation of the captured CO₂ to the storage site. Among various transportation modes (e.g. truck, ship, pipeline), high-pressure pipelines are widely recognised as the most practical and economical transport option. The high pressures involved, combined with the huge amount of inventory and its hazardous nature, poses significant risks to life, environment, and property in the event of pipeline failure. As such, ensuring the safe operation of such pipelines is of paramount importance.

In light of the above, this thesis described the development, testing, and application of three techniques for the safety assessment of pressurised pipelines covering pipeline decompression modelling, Quantitative Risk Assessment (QRA) and risk mitigation planning as follows:

- the extension of a computationally efficient Vessel Blowdown Model (VBM) to account for un-isolated releases and fluid/wall heat exchanges.
- the development of an analytical approach for estimating the failure hole size probability distribution for pressurised CO₂ pipelines as part of pipeline QRA, taking into account the statistical significance of the failure data being employed.
- the development of a probabilistic Multi-Objective Optimisation (MOO) technique for selecting the optimal ESDV configurations for pressurised CO₂ pipelines, taking into account the uncertainties in the pipe characteristics and operating conditions.

In the following, the main findings in each chapter are summarised.

Chapter 2 presented a comprehensive review for the key steps in pressurised pipeline safety assessment. As the first step, the mathematical modelling of pressurised pipelines was described, mainly focusing on the governing equations for fluid flow dynamics, constituent relations for fluid/wall interactions and equation of state for predicting the fluid thermal properties and equilibrium data. This was followed by a review of relevant studies focusing on the applications of the Homogeneous Equilibrium Mixture (HEM) model for predicting pressurised pipeline decompression behaviours.

For the second step, the QRA for pressurised CO₂ pipelines was reviewed. This part summarised the important aspects involved in performing QRA, including the modelling of dense gas dispersion, calculation of pipe failure frequency, and evaluation of the corresponding individual and societal risk levels. Turning to the third step involving the risk mitigation planning, the application of the MOO technique, including its theoretical background and solution methods, in configuring inline Emergency Shutdown Valves (ESDVs) as the front-line mitigation tool for pressurised pipeline failures was presented. This was followed by a review of selected example studies for optimising the ESDV configuration and the design for pressurised pipelines.

From the above review, the following key recommendations are made:

- A broader range of failure scenarios such as large puncture failures and un-isolated releases should be included in the development and validation of analytically based pipeline decompression models;
- More complex metrics for representing the risk following pipeline failure can be introduced in the development of MOO techniques for optimising ESDV configurations.

In Chapter 3, the development and testing of a computationally efficient Modified

Vessel Blowdown Model (MVBM) for predicting the outflow characteristics in the event of pressurised pipeline failures was described. The developed model presented a fundamental extension to the VBM, addressing the major limitations of the VBM in handling un-isolated releases and fluid/wall heat exchanges. The model was developed based on incorporating additional mass and energy terms accounting for the inflow into the standard vessel discharge equations. Given that the resulting equations can be solved analytically, the fundamental drawback of long computational runtimes associated with numerically based pipeline decompression models has been addressed using the approach.

The MVBM was first verified against the predictions using an extensively validated numerically based pipeline decompression model for simulating the un-isolated releases from a hypothetical methane pipeline following its failure. Based on the same case study, the MVBM was next tested against the VBM in simulating isolated releases. The simulation runs for the above involved a wide range of test scenarios varying inflow rate (1 to 7.5 kg/s), pipe length (100 to 5000 m) and puncture to pipe internal diameter ratio (0.2 to 0.8).

The results showed that the MVBM generally produced good agreement with the numerical model predictions in simulating pipeline failure releases at a fraction of the computational runtime. It was also noteworthy that improved simulation results could be observed in the predictions by MVBM as compared to those by the VBM.

A particularly interesting finding from the above tests was that the MVBM handled punctures with relatively large puncture to pipe internal diameter ratios with reasonable accuracy based on comparison with the VBM predictions. This was considered a substantial improvement to the VBM where only punctures smaller than 40% of the pipe internal diameter could be well handled. This improvement was thought to be a consequence of the fact MVBM accounted for fluid/wall heat exchanges which became

significant for large puncture to pipe diameter ratios. However, the accuracy of the MVBM decreased with the increase in the puncture diameter. This could be due to the increasing incapability of the quasi-steady state assumption, which ignored the growing influence of fluid/wall frictional effects in the vicinity of the puncture as its diameter increased.

Chapter 4 presented the development and application of a statistical analytical technique for determining the failure hole size probability distribution for pressurised CO₂ pipelines. A particularly important feature was addressing the pressing dilemma of the relatively small pool of the recorded historical data available for CO₂ pipelines to ascertain a reasonable prediction of their failure risks in the context of CCUS operations and how these are compared against those for hydrocarbon pipelines.

The methodology involved fitting the Weibull and lognormal distributions to the puncture diameter data obtained from the PHMSA database using the Maximum likelihood Estimator (MLE) method in conjunction with either Kolmogorov-Smirnov (K-S) test if the sample size was deemed sufficiently large, or, bootstrapping if not. Whether the sample size being employed was statistically representative was determined by calculating the corresponding MLE quality using Monte Carlo simulation.

Using the above method, the failure hole size probability distribution, expressed as the Cumulative Distribution Function (CDF) was determined for CO₂ pipelines and compared against those for hydrocarbon (natural gas and crude oil) pipelines. Remarkably, the results obtained indicated that as compared to the latter, CO₂ pipelines were most likely to experience smaller puncture size failures, thus resulting in smaller magnitude hence more prolonged releases. This observation directly impacts the preventive and emergency response planning required especially in the case of buried CO₂ pipelines, where small leaks can remain undetected for long periods. Furthermore,

despite being a continuous variable, in practice, the through-wall failure hole size in pressurised pipelines is often taken as a discrete variable, which compromises the validity of the subsequent failure consequence assessment and risk mitigation planning. The developed technique addressed this important shortcoming.

Chapter 5 described the development and application of a probabilistic MOO technique for selecting the optimal ESDV configurations for pressurised CO₂ pipelines based on treating the risk associated with pipeline failure as a probabilistic variable. The above involved first describing the uncertainties in the pipeline operational and failure characteristics using classical Probability Distribution Functions (PDFs) followed by performing a Monte Carlo simulation involving the random sampling from the resulting PDFs to obtain the corresponding risk probability distribution. Based the obtained risk probability distribution, a plane mapping the risk in the space of the objective functions could be constructed for the decision makers to determine the optimal solution according to their subjective preferences. Such work is fundamentally important for configuring pipeline ESDVs given that in practice the failure scenario can vary greatly from one pipe incident to the next, depending on the failure initiation mechanism, as well as other relevant conditions such as the pipe wall material, thickness and cathodic protection employed to prevent corrosion.

The developed technique was applied to study an industry-relevant case involving a 300 km length, 309.6 mm internal diameter pipeline transporting CO₂ initially at 129 bar and 307.24 K. The efficacy of the proposed technique was then demonstrated based on selecting the optimal ESDV number that struck a balance between the risk associated with pipeline failure and ESDV costs.

A key finding of this study was that there existed a threshold beyond which increasing the number of ESDVs installed along the pipe provided a marginal increase in the probability of limiting the risk below the decision maker preferred level at substantially

increased costs. The above important findings underlined the efficacy of the proposed technique as a valuable decision-making tool for selecting the optimal inline ESDV configurations that maintain the costs at a minimum or manageable level while yielding minimal loss of risk mitigation impacts.

In conclusion, the work presented in this thesis provides the mathematical and computational basis for the efficient and accurate safety assessment of pressurised pipelines, addressing the key limitations in efficient pipeline decompression modelling, pressurised pipeline QRA and risk mitigation planning concerning the optimal configuration of inline ESDVs. The techniques developed in this work will benefit the safety design of pressurised CO₂ pipelines, hence help to accelerate the large-scale deployment of CCUS as part of the global quest for reaching the ambitious net zero emission target.

6.2 Suggestions for Future Work

6.2.1 Extension of the MVBM to Accounting for Various Upstream Sources

In Chapter 3, a computationally efficient MVBM was developed. It was shown to successfully address the fundamental limitation of the VBM in handling un-isolated releases. Nevertheless, the developed model is only limited to simulating constant feed flow rate whereas in reality, time-varying feed flow rate as a result of e.g. upstream pumps or reservoirs may be inevitable. Handling the above limitation, the introduction of the appropriate upstream boundary conditions would broaden the range of the applicability of the MVBM.

6.2.2 Sample Quality Measurement

In Chapter 4, as part of the methodology for obtaining reliable probability distributions

of the through-wall failure hole size, the statistical significance of the samples being employed to derive the distributions was assessed based on their sizes. However, whether the sample ideally covers, for example, a sufficiently wide range of operating conditions, or the entire range of puncture size was not investigated. Given this, future work should focus on investigating the sample statistical significance based on other sample features such as the sample quality.

In addition to the above, the continuous recording of the failure statistics covering a full range of possible failure scenarios and classifying these statistics in a detailed manner are fundamentally important, especially for CO₂ pipelines given their relatively short operational experience and small numbers, reinforced by their major role in CCS. The growing wealth of such statistics can be used to further improve the accuracy of the proposed method in predicting the failure hole size probability distributions for pressurised pipelines. The above can be in turn employed to estimate the pipeline failure rate.

6.2.3 Modelling of Parameter Uncertainties using Complicated Methods

In Chapter 5, a probabilistic MOO technique was developed to optimise the ESDV configurations for pressurised CO₂ pipelines, accounting for the uncertainties in pipeline operational and failure parameters. The efficacy of this technique was demonstrated based on an industry-relevant case study. However, for some of the parameters considered in the study (e.g. fluid temperature, ambient temperature), their uncertainties were modelled relatively simply using normal distributions whereas in practice, they may have different behaviours. Given the above, future work should focus on collecting real operational data and subsequently deriving the corresponding probability distributions for reliably representing the parameter uncertainties using rigorous statistical methods.

References

- Ahsanullah, M., Kibria, B.M.G., Shakil, M., 2014. Normal Distribution. pp. 7–50.
https://doi.org/10.2991/978-94-6239-061-4_2
- Akselsen, O.M., Fostervoll, H., Ahlen, C.H., 2010. Mechanical properties of hyperbaric gas metal arc welds in X65 pipeline steel. *International Journal of Offshore and Polar Engineering* 20.
- Alves, D., Bahiense, A., Bastos, M., Borges, C., Lima, G., 2018. A Brazilian pipeline incident database: The Petrobras and Transpetro initiative, in: *Volume 2: Pipeline Safety Management Systems; Project Management, Design, Construction, and Environmental Issues; Strain Based Design; Risk and Reliability; Northern Offshore and Production Pipelines*. American Society of Mechanical Engineers.
<https://doi.org/10.1115/IPC2018-78584>
- Alves, F. da S., Souza, J.N.M. de, Costa, A.L.H., 2016. Multi-objective design optimization of natural gas transmission networks. *Comput Chem Eng* 93, 212–220. <https://doi.org/10.1016/j.compchemeng.2016.06.006>
- ANSYS, 2011. ANSYS CFX-solver theory guide - Release 14.0.
- Apostolakis, G.E., 2004. How useful is quantitative risk assessment? *Risk Analysis* 24, 515–520. <https://doi.org/10.1111/j.0272-4332.2004.00455.x>
- Badida, P., Balasubramaniam, Y., Jayaprakash, J., 2019. Risk evaluation of oil and natural gas pipelines due to natural hazards using fuzzy fault tree analysis. *J Nat Gas Sci Eng* 66, 284–292. <https://doi.org/10.1016/j.jngse.2019.04.010>
- Barron, F.H., Barrett, B.E., 1996. Decision quality using ranked attribute weights. *Manage Sci* 42, 1515–1523. <https://doi.org/10.1287/mnsc.42.11.1515>

- Batchelor, G.K., 1967. An introduction to fluid dynamics. Cambridge University Press.
- Bechikh, S., Kessentini, M., Said, L. ben, Ghédira, K., 2015. Preference Incorporation in Evolutionary Multiobjective Optimization. pp. 141–207. <https://doi.org/10.1016/bs.adcom.2015.03.001>
- Benayoun, R., Roy, B., Sussman, N., 1966. Manual de reference du programme ELECTRE. Note de Synthèse et Formation 25, 79.
- Bendiksen, K.H., Maines, D., Moe, R., Nuland, S., 1991. The dynamic two-fluid model OLGA: Theory and application. SPE Production Engineering 6, 171–180. <https://doi.org/10.2118/19451-PA>
- Bisgaard, C., Sørensen, H.H., Spangenberg, S., 1987. A finite element method for transient compressible flow in pipelines. Int J Numer Methods Fluids 7, 291–303. <https://doi.org/10.1002/fld.1650070308>
- BP, 2020. Statistical review of world energy 2020. London.
- Brito, A.J., de Almeida, A.T., Mota, C.M.M., 2010. A multicriteria model for risk sorting of natural gas pipelines based on ELECTRE TRI integrating Utility Theory. Eur J Oper Res 200, 812–821. <https://doi.org/10.1016/j.ejor.2009.01.016>
- Brown, S., Martynov, S., Mahgerefteh, H., Chen, S., Zhang, Y., 2014a. Modelling the non-equilibrium two-phase flow during depressurisation of CO₂ pipelines. International Journal of Greenhouse Gas Control 30, 9–18. <https://doi.org/10.1016/j.ijggc.2014.08.013>
- Brown, S., Martynov, S., Mahgerefteh, H., Fairweather, M., Woolley, R.M., Wareing, C.J., Falle, S.A.E.G., Rutters, H., Niemi, A., Zhang, Y.C., Chen, S., Besnebat, J., Shah, N., Dowell, N. mac, Proust, C., Farret, R., Economou, I.G., Tsangaris, D.M., Boulougouris, G.C., van Wittenberghe, J., 2014b. CO₂QUEST: Techno-economic

- assessment of CO₂ quality effect on its storage and transport. *Energy Procedia* 63, 2622–2629. <https://doi.org/10.1016/j.egypro.2014.11.284>
- Brown, S., Martynov, S., Mahgerefteh, H., Proust, C., 2013. A homogeneous relaxation flow model for the full bore rupture of dense phase CO₂ pipelines. *International Journal of Greenhouse Gas Control* 17, 349–356. <https://doi.org/10.1016/j.ijggc.2013.05.020>
- Brown, S., Sundara, V., Martynov, S., Mahgerefteh, H., 2014c. Optimal valve spacing for next generation CO₂ pipelines. pp. 265–270. <https://doi.org/10.1016/B978-0-444-63456-6.50045-4>
- Buaprommart, K., Mahgerefteh, H., Martynov, S., Striolo, A., 2019. Shale gas well blowout fire and explosion modelling. *Appl Therm Eng* 149, 1061–1068. <https://doi.org/10.1016/j.applthermaleng.2018.12.105>
- Burgess, D.S., Zabetakis, M.G., 1973. Detonation of a flammable cloud following a propane pipeline break: The December 9, 1970, explosion in Port Hudson.
- Cadima, J.F.C.L., Jolliffe, I.T., 2001. Variable selection and the interpretation of principal subspaces. *J Agric Biol Environ Stat* 6, 62–79. <https://doi.org/10.1198/108571101300325256>
- Chamberlain, G.A., 1987. Developments in design methods for predicting thermal radiation from flares. *Chem. Eng. Res. Des.* 65, 299–309.
- Chaplin, Z., 2017. Major accident hazard pipeline failure frequency calculation using fracture mechanics. *Safety and Reliability* 37, 217–232. <https://doi.org/10.1080/09617353.2018.1524679>
- Chaplin, Z., 2015a. Rewriting the PIPIN code to use a Monte Carlo solution approach. Buxton.

- Chaplin, Z., 2015b. Data updates to HSE's PIPeline INtegrity model(PIPIN). Buxton.
- Chen, J.R., 1993. Modelling of transient flow in pipeline blowdown problems. Imperial College London.
- Chen, J.R., Richardson, S.M., Saville, G., 1995. Modelling of two-phase blowdown from pipelines-II. A simplified numerical method for multi-component mixtures. *Chem Eng Sci* 50, 2173–2187. [https://doi.org/10.1016/0009-2509\(95\)00009-T](https://doi.org/10.1016/0009-2509(95)00009-T)
- Chen, J.R., Richardson, S.M., Saville, G., 1992. Numerical simulation of full-bore ruptures of pipelines containing perfect gases. *Process Safety and Environmental Protection* 70, 59–69.
- Chen, N.H., 1979. An explicit equation for friction factor in pipe. *Industrial and Engineering Chemistry Fundamentals* 18, 296–297. <https://doi.org/10.1021/i160071a019>
- CIA, 2021. Pipelines [WWW Document]. The World Factbook. URL <https://www.cia.gov/the-world-factbook/field/pipelines/> (accessed 6.16.21).
- Clancey, V.J., 1976. Liquid and vapour emission and dispersion. Loughborough.
- Coello, C.A.C., Lamont, G.B., van Veldhuizen, D.A., 2007. *Evolutionary Algorithms for Solving Multi-Objective Problems*, 2nd ed. Springer, New York.
- Colebrook, C.F., 1939. Turbulent flow in pipes with particular reference to transition region between the smooth and rough pipe laws. *Journal of the Institution of Civil engineers* 12, 393–422.
- Coleman, M.E., Marks, H.M., 1999. Qualitative and quantitative risk assessment. *Food Control* 10, 289–297. [https://doi.org/10.1016/S0956-7135\(99\)00052-3](https://doi.org/10.1016/S0956-7135(99)00052-3)
- Concawe, 2011. Oil pipelines management group's special task force on oil pipeline

spillages (OP/STF-1). Brussels.

Connell, D.P., 2005. Carbon dioxide capture options for large point sources in the midwestern United States: An assessment of candidate technologies. Final report.

Conover, W.J., 1999. Practical Nonparametric Statistics, 3rd ed. John Wiley & Sons, New York.

Corne, D.W., Knowles, J.D., 2007. Techniques for highly multiobjective optimisation, in: Proceedings of the 9th Annual Conference on Genetic and Evolutionary Computation - GECCO '07. ACM Press, New York, New York, USA, p. 773.
<https://doi.org/10.1145/1276958.1277115>

Cosham, A., Jones, D.G., Armstrong, K., Allason, D., Barnett, J., 2012. The decompression behaviour of carbon dioxide in the dense phase, in: International Pipeline Conference. American Society of Mechanical Engineers, pp. 447–464.
<https://doi.org/10.1115/IPC2012-90461>

Coulson, J.M., Richardson, J.F., Backhurst, J.R., Harker, J.H., 1999. Chemical Engineering Volume 1: Fluid Flow, Heat Transfer and Mass Transfer. Butterworth-Heinemann.

Courant, R., Friedrichs, K., Lewy, H., 1928. Über die partiellen differenzgleichungen der mathematischen physik. Math Ann 100, 32–74.
<https://doi.org/10.1007/BF01448839>

CPPEC, 2012. Feasibility study report - Harbin-Shenyang pipeline, Unpublished Technical Report.

Crowl, D.A., Louvar, J.F., 2011. Chemical Process Safety: Fundamentals with Applications, 3rd ed. Pearson.

- Cullen, T.Hon.L., 1990. The public inquiry into the Piper Alpha disaster.
- Dawes, R.M., Corrigan, B., 1974. Linear models in decision making. *Psychol Bull* 81, 95–106. <https://doi.org/10.1037/h0037613>
- de Stefani, V., Carr, P., 2010. A model to estimate the failure rates of offshore pipelines, in: *Proceedings of the Biennial International Pipeline Conference, IPC*. pp. 437–447. <https://doi.org/10.1115/IPC2010-31230>
- de Weck, O.L., 2004. Multiobjective optimization: History and promise, in: *The Third China-Japan-Korea Joint Symposium on Optimization of Structural and Mechanical Systems*. Kanazawa, Japan.
- Demissie, A.G., 2015. Multi-objective optimization for natural gas pipeline network operation (PhD). Lamar University.
- Dodgson, J.S., Spackman, M., Pearman, A., Phillips, L.D., 2009. *Multi-criteria analysis: A manual*. London.
- Duncan, I., Wang, H., 2014a. Evaluating the likelihood of pipeline failures for future offshore CO₂ sequestration projects. *International Journal of Greenhouse Gas Control* 24, 124–138. <https://doi.org/10.1016/j.ijggc.2014.02.004>
- Duncan, I., Wang, H., 2014b. Estimating the likelihood of pipeline failure in CO₂ transmission pipelines: New insights on risks of carbon capture and storage. *International Journal of Greenhouse Gas Control* 21, 49–60. <https://doi.org/10.1016/j.ijggc.2013.11.005>
- Efron, B., 1979. Bootstrap methods: Another look at the jackknife. *Ann Stat* 7, 1–26.
- EGIG, 2018. *Gas pipeline incidents: 10th report of the European gas incident data group (period 1970-2016)*.

- Einhorn, H.J., McCoach, W., 1977. A simple multiattribute utility procedure for evaluation. *Behavioral Science* 22, 270–282. <https://doi.org/10.1002/bs.3830220405>
- Eliason, S., 1993. Maximum likelihood estimation: Logic and practice, Sage University Paper Series on Quantitative Applications in the Social Sciences, 07-096. Sage, Newbury Park, CA.
- England, W.G., Teuscher, L.H., Hauser, L.E., Freedman, B.E., 1978. Atmospheric dispersion of a liquefied natural gas vapour cloud using SIGMET, a three dimensional hydrodynamic computer model, in: Proceedings of the 1978 Heat Transfer and Fluid Mechanics Institute Conference. Pullman, pp. 4–20.
- Ermak, D.L., 1990. User's manual for SLAB: An atmospheric dispersion model for denser-than-air releases.
- Flatt, R., 1986. Unsteady compressible flow in long pipelines following a rupture. *Int J Numer Methods Fluids* 6, 83–100. <https://doi.org/10.1002/fld.1650060204>
- Gale, J., Davison, J., 2004. Transmission of CO₂ - safety and economic considerations. *Energy* 29, 1319–1328. <https://doi.org/10.1016/j.energy.2004.03.090>
- Gao, L., Fang, M., Li, H., Hetland, J., 2011. Cost analysis of CO₂ transportation: Case study in China. *Energy Procedia* 4, 5974–5981.
- GCCSI, 2022. Facilities database [WWW Document].
- GCCSI, 2021. Global status of CCS 2021.
- GexCon, 2013. FLACS v10.0 user's manual.
- Ginos, B.F., 2009. Parameter estimation for the lognormal distribution. Brigham Young University.

- Goicoechea, A., Duckstein, L., Fogel, M.M., 1979a. Multiple objectives under uncertainty: An illustrative application of PROTRADE. *Water Resour Res* 15, 203–210. <https://doi.org/10.1029/WR015i002p00203>
- Goicoechea, A., Duckstein, L., Fogel, M.M., 1979b. Multiple objectives under uncertainty: An illustrative application of protrade. *Water Resour Res* 15, 203–210. <https://doi.org/10.1029/WR015i002p00203>
- Goodfellow, G., Turner, S., Haswell, J., Espiner, R., 2012. An update to the UKOPA pipeline damage distributions, in: *International Pipeline Conference*. American Society of Mechanical Engineers, pp. 541–547. <https://doi.org/10.1115/IPC2012-90247>
- Green, D.W., Southard, M.Z., 2019. *Perry's Chemical Engineers' Handbook*, 9th ed. McGraw-Hill, New York.
- Groves, T.K., Bishnoi, P.R., Wallbridge, J.M.E., 1978. Decompression wave velocities in natural gases in pipe lines. *Can J Chem Eng* 56, 664–668. <https://doi.org/10.1002/cjce.5450560602>
- Gunantara, N., 2018. A review of multi-objective optimization: Methods and its applications. *Cogent Eng* 5, 1502242. <https://doi.org/10.1080/23311916.2018.1502242>
- Haszeldine, R.S., Stewart, J., Ainger, D., Argent, S., Carter, R., 2010. Feasibility study for Europe-wide CO₂ infrastructures.
- Haukoos, J.S., Lewis, R.J., 2005. Advanced statistics: Bootstrapping confidence intervals for statistics with “difficult” distributions. *Academic Emergency Medicine* 12, 360–365. <https://doi.org/10.1197/j.aem.2004.11.018>
- Hibiki, T., Ishii, M., 2003. One-dimensional drift-flux model and constitutive equations

for relative motion between phases in various two-phase flow regimes. *Int J Heat Mass Transf* 46, 4935–4948. [https://doi.org/10.1016/S0017-9310\(03\)00322-3](https://doi.org/10.1016/S0017-9310(03)00322-3)

Hoffman, J.D., Zucrow, M.J., 1976. *Gas Dynamics*. Wiley.

IEA, 2022. *Global energy review: CO₂ emissions in 2021*.

IEA, 2021. *Net zero by 2050: A roadmap for the global energy sector*.

IEA, 2010. *Energy technology perspectives 2010: Scenarios and strategies to 2050*. Paris.

IPCC, 2013. *Climate change 2013: The physical science basis. Contribution of working group I to the fifth assessment report of the Intergovernmental Panel on Climate Change*.

Jabeen, R., Zaka, A., 2020. Estimation of parameters of the continuous uniform distribution: Different classical methods. *Journal of Statistics and Management Systems* 23, 529–547. <https://doi.org/10.1080/09720510.2019.1639948>

Ji, Q., 2020. Foundation and basics, in: *Probabilistic Graphical Models for Computer Vision*. Elsevier, pp. 11–29. <https://doi.org/https://doi.org/10.1016/B978-0-12-803467-5.00007-1>

Jia, J., Fischer, G.W., Dyer, J.S., 1998. Attribute weighting methods and decision quality in the presence of response error: a simulation study. *J Behav Decis Mak* 11, 85–105. [https://doi.org/10.1002/\(SICI\)1099-0771\(199806\)11:2<85::AID-BDM282>3.0.CO;2-K](https://doi.org/10.1002/(SICI)1099-0771(199806)11:2<85::AID-BDM282>3.0.CO;2-K)

Jo, Y.-D., Ahn, B.J., 2005. A method of quantitative risk assessment for transmission pipeline carrying natural gas. *J Hazard Mater* 123, 1–12. <https://doi.org/10.1016/j.jhazmat.2005.01.034>

- Johnson, A.D., Brightwell, H.M., Carsley, A.J., 1994. A model for predicting the thermal radiation hazards from large-scale horizontally released natural gas jet fires. *Process Safety and Environmental Protection* 72, 157–166.
- Jung, K., Lee, J., Gupta, V., Cho, G., 2019. Comparison of bootstrap confidence interval methods for GSCA using a Monte Carlo simulation. *Front Psychol* 10, 2215. <https://doi.org/https://doi.org/10.3389/fpsyg.2019.02215>
- Khare, V., Yao, X., Deb, K., 2003. Performance scaling of multi-objective evolutionary algorithms. pp. 376–390. https://doi.org/10.1007/3-540-36970-8_27
- Kissell, R.L., Poserina, J., 2017. *Optimal Sports Math, Statistics, and Fantasy*. Academic Press.
- Koch, P., 2008. Equivalent diameters of rectangular and oval ducts. *Building Services Engineering Research and Technology* 29, 341–347.
- Kolmogorov, A.N., 1933. Sulla determinazione empirica di una legge di distribuzione. *Giornale dell’Istituto Italiano degli Attuari* 4, 83–91.
- Koopman, R.P., Ermak, D.L., Chan, S.T., 1989. A review of recent field tests and mathematical modelling of atmospheric dispersion of large spills of denser-than-air gases. *Atmospheric Environment* (1967) 23, 731–745. [https://doi.org/10.1016/0004-6981\(89\)90475-7](https://doi.org/10.1016/0004-6981(89)90475-7)
- Koornneef, J., Spruijt, M., Molag, M., Ramirez, A., Faaij, A., Turkenburg, W., 2009. Uncertainties in risk assessment of CO₂ pipelines. *Energy Procedia* 1, 1587–1594. <https://doi.org/10.1016/j.egypro.2009.01.208>
- Kruse, H., Tekiela, M., 1996. Calculating the consequences of a CO₂ pipeline rupture. *Energy Convers Manag* 37, 1013–1018. [https://doi.org/10.1016/0196-8904\(95\)00291-X](https://doi.org/10.1016/0196-8904(95)00291-X)

- Lang, E., 1991. Gas flow in pipelines following a rupture computed by a spectral method. *Zeitschrift für angewandte Mathematik und Physik ZAMP* 42, 183–197. <https://doi.org/10.1007/BF00945792>
- Larry, W., 2004. *All of Statistics: A Concise Course in Statistical Inference*. Springer, Berlin.
- Li, J., Liang, B., Li, C., Yan, M., Yu, J., 2019. Calculation methods for the gas pipeline failure rate. *J Pet Sci Eng* 174, 229–234. <https://doi.org/10.1016/j.petrol.2018.11.020>
- Li, J., Zhang, H., Han, Y., Wang, B., 2016. Study on failure of third-party damage for urban gas pipeline based on fuzzy comprehensive evaluation. *PLoS One* 11, e0166472. <https://doi.org/10.1371/journal.pone.0166472>
- Lisbona, D., McGillivray, A., Saw, J.L., Gant, S., Bilio, M., Wardman, M., 2014. Risk assessment methodology for high-pressure CO₂ pipelines incorporating topography. *Process Safety and Environmental Protection* 92, 27–35. <https://doi.org/10.1016/j.psep.2013.09.003>
- Long, J.S., Freese, J., 2006. *Regression Models for Categorical Dependent Variables using Stata*. Stata Press.
- Lydell, B.O.Y., 2000. Pipe failure probability-the Thomas paper revisited. *Reliab Eng Syst Saf* 68, 207–217. [https://doi.org/10.1016/S0951-8320\(00\)00016-8](https://doi.org/10.1016/S0951-8320(00)00016-8)
- Lyons, C.J., Goodfellow, G.D., Haswell, J. v, 2020. *UKOPA pipeline product loss incidents and faults report (1962-2018)*. Ambergate, UK.
- Mahgerefteh, H., 1997. *PipeTech*.
- Mahgerefteh, H., Atti, O., Denton, G., 2007. An interpolation technique for rapid CFD

- simulation of turbulent two-phase flows. *Process Safety and Environmental Protection* 85, 45–50. <https://doi.org/10.1205/psep.05118>
- Mahgerefteh, H., Brown, S., Denton, G., 2012a. Modelling the impact of stream impurities on ductile fractures in CO₂ pipelines. *Chem Eng Sci* 74, 200–210. <https://doi.org/10.1016/j.ces.2012.02.037>
- Mahgerefteh, H., Brown, S., Martynov, S., 2012b. A study of the effects of friction, heat transfer, and stream impurities on the decompression behavior in CO₂ pipelines. *Greenhouse Gases: Science and Technology* 2, 369–379. <https://doi.org/10.1002/ghg.1302>
- Mahgerefteh, H., Brown, S., Zhang, P., 2010. A dynamic boundary ductile fracture model for pressurised pipelines, in: *The First International Forum on Transportation of CO₂ by Pipeline*.
- Mahgerefteh, H., Denton, G., Rykov, Y., 2008. A hybrid multiphase flow model. *AIChE Journal* 54, 2261–2268. <https://doi.org/10.1002/aic.11569>
- Mahgerefteh, H., Jalali, N., Fernandez, M.I., 2011. When does a vessel become a pipe? *AIChE Journal* 57, 3305–3314. <https://doi.org/10.1002/aic.12541>
- Mahgerefteh, H., Oke, A., Atti, O., 2006. Modelling outflow following rupture in pipeline networks. *Chem Eng Sci* 61, 1811–1818. <https://doi.org/10.1016/j.ces.2005.10.013>
- Mahgerefteh, H., Saha, P., Economou, I.G., 2000. Modeling fluid phase transition effects on dynamic behavior of ESDV. *AIChE Journal* 46, 997–1006. <https://doi.org/10.1002/aic.690460512>
- Mahgerefteh, H., Saha, P., Economou, I.G., 1999. Fast numerical simulation for full bore rupture of pressurized pipelines. *AIChE Journal* 45, 1191–1201.

<https://doi.org/10.1002/aic.690450605>

Mahgerefteh, H., Saha, P., Economou, I.G., 1997. A study of the dynamic response of emergency shutdown valves following full bore rupture of gas pipelines. *Process Safety and Environmental Protection* 75, 201–209. <https://doi.org/10.1205/095758297529039>

Mahgerefteh, H., Zhang, P., Brown, S., 2016. Modelling brittle fracture propagation in gas and dense-phase CO₂ transportation pipelines. *International Journal of Greenhouse Gas Control* 46, 39–47. <https://doi.org/10.1016/j.ijggc.2015.12.021>

Malakooti, B., 1988. A decision support system and a heuristic interactive approach for solving discrete multiple criteria problems. *IEEE Trans Syst Man Cybern* 18, 273–284. <https://doi.org/10.1109/21.3466>

Markiewicz, M., 2012. A review of mathematical models for the atmospheric dispersion of heavy gases. Part I. A classification of models. *Ecological Chemistry and Engineering S* 19, 297–314. <https://doi.org/10.2478/v10216-011-0022-y>

Marler, R.T., Arora, J.S., 2004. Survey of multi-objective optimization methods for engineering. *Structural and Multidisciplinary Optimization* 26, 369–395. <https://doi.org/10.1007/s00158-003-0368-6>

Martynov, S., Brown, S., Mahgerefteh, H., Sundara, V., 2013. Modelling choked flow for CO₂ from the dense phase to below the triple point. *International Journal of Greenhouse Gas Control* 19, 552–558. <https://doi.org/10.1016/j.ijggc.2013.10.005>

Martynov, S., Brown, S., Mahgerefteh, H., Sundara, V., Chen, S., Zhang, Y., 2014. Modelling three-phase releases of carbon dioxide from high-pressure pipelines. *Process Safety and Environmental Protection* 92, 36–46. <https://doi.org/10.1016/j.psep.2013.10.004>

- Martynov, S., Mahgerefteh, H., Yu, J., 2018a. An analysis of the emergency isolation of high-pressure pipelines transporting supercritical fluids, in: Institution of Chemical Engineers Symposium Series (Vol.163, No.163). Institution of Chemical Engineers (IChemE).
- Martynov, S., Zheng, W., Mahgerefteh, H., Brown, S., Hebrard, J., Jamois, D., Proust, C., 2018b. Computational and experimental study of solid-phase formation during the decompression of high-pressure CO₂ pipelines. *Ind Eng Chem Res* 57, 7054–7063. <https://doi.org/10.1021/acs.iecr.8b00181>
- Massey, B.S., 1983. *Mechanics of fluids*. Van Nostrand Reinhold, Wokingham.
- Massey Jr, F.J., 1951. The Kolmogorov-Smirnov test for goodness of fit. *J Am Stat Assoc* 46, 68–78.
- Mathews, Wesley., 2022. Failure investigation report - Denbury Gulf Coast Pipelines LLC.
- McGillivray, A., Wilday, J., 2009. Comparison of risks from carbon dioxide and natural gas pipelines. Buxton.
- McQuaid, J., Britter, R.E., 1988. *Workbook on the dispersion of dense gases*.
- Medina, H., Arnaldos, J., Casal, J., Bonvicini, S., Cozzani, V., 2012. Risk-based optimization of the design of on-shore pipeline shutdown systems. *J Loss Prev Process Ind* 25, 489–493. <https://doi.org/10.1016/j.jlp.2011.12.005>
- Melchers, R.E., 2005. The effect of corrosion on the structural reliability of steel offshore structures. *Corros Sci* 47, 2391–2410. <https://doi.org/10.1016/j.corsci.2005.04.004>
- Menon, E.S., 2005. *Gas pipeline hydraulics*. CRC Press.

- Miao, C., Zhao, J., 2012. Risk analysis for the urban buried gas pipeline with fuzzy comprehensive assessment method. *J Press Vessel Technol* 134. <https://doi.org/10.1115/1.4004625>
- Michelsen, M.L., 1982. The isothermal flash problem. Part II. Phase-split calculation. *Fluid Phase Equilib* 9, 21–40. [https://doi.org/10.1016/0378-3812\(82\)85002-4](https://doi.org/10.1016/0378-3812(82)85002-4)
- Molina, J., Santana, L. v., Hernández-Díaz, A.G., Coello Coello, C.A., Caballero, R., 2009. g-dominance: Reference point based dominance for multiobjective metaheuristics. *Eur J Oper Res* 197, 685–692. <https://doi.org/10.1016/j.ejor.2008.07.015>
- Monarchi, D.E., Kisiel, C.C., Duckstein, L., 1973. Interactive multiobjective programming in water resources: A case study. *Water Resour Res* 9, 837–850. <https://doi.org/10.1029/WR009i004p00837>
- Morbee, J., Serpa, J., Tzimas, E., 2012. Optimised deployment of a European CO₂ transport network. *International Journal of Greenhouse Gas Control* 7, 48–61. <https://doi.org/10.1016/j.ijggc.2011.11.011>
- Morin, A., Kragset, S., Munkejord, S.T., 2012. Pipeline flow modelling with source terms due to leakage: The straw method. *Energy Procedia* 23, 226–235. <https://doi.org/10.1016/j.egypro.2012.06.023>
- Muhlbauer, W.K., 1996. *Pipeline Risk Management Manual: Ideas, Techniques, and Resources*. Gulf Publishing Company, Houston, TX.
- Munkejord, S.T., Hammer, M., 2015. Depressurization of CO₂-rich mixtures in pipes: Two-phase flow modelling and comparison with experiments. *International Journal of Greenhouse Gas Control* 37, 398–411. <https://doi.org/10.1016/j.ijggc.2015.03.029>

- Munkejord, S.T., Hammer, M., Løvseth, S.W., 2016. CO₂ transport: Data and models- A review. *Appl Energy* 169, 499–523. <https://doi.org/10.1016/j.apenergy.2016.01.100>
- Murata, T., Ishibuchi, H., Tanaka, H., 1996. Multi-objective genetic algorithm and its applications to flowshop scheduling. *Comput Ind Eng* 30, 957–968. [https://doi.org/10.1016/0360-8352\(96\)00045-9](https://doi.org/10.1016/0360-8352(96)00045-9)
- NEB, 2010. Comparative analysis of pipeline performance 2000-2008.
- Neill, S.P., Hashemi, M.R., 2018. Ocean modelling for resource characterization, in: *Fundamentals of Ocean Renewable Energy*. Academic Press, pp. 193–235.
- Neunert, U., Kaufmann, K., 2012. Presenting the societal risk of pipelines transporting hazardous materials, in: *Institution of Chemical Engineers Symposium Series (Vol.158, No.158)*. pp. 307–312.
- Nielsen, M.A., 2011. Parameter estimation for the two-parameter Weibull distribution. Brigham Young University, Provo.
- Norris, H.L., 1994. Hydrocarbon blowdown from vessels and pipelines, in: *SPE Annual Technical Conference and Exhibition*. Society of Petroleum Engineers. <https://doi.org/10.2118/28519-MS>
- Norris, H.L., Puls, R.C., 1993. Single-phase or multiphase blowdown of vessels or pipelines, in: *SPE Annual Technical Conference and Exhibition*. Society of Petroleum Engineers. <https://doi.org/10.2118/26565-MS>
- Nyborg, M., Arvidsson, K., Johansson, J., Liljemark, S., Olsson, L., 2011. Risk analysis methodology for CO₂ transport including quantified risk calculation. *Energy Procedia* 4, 2816–2823. <https://doi.org/10.1016/j.egypro.2011.02.186>

- Oke, A., Mahgerefteh, H., Economou, I., Rykov, Y., 2003. A transient outflow model for pipeline puncture. *Chem Eng Sci* 58, 4591–4604. [https://doi.org/10.1016/S0009-2509\(03\)00338-5](https://doi.org/10.1016/S0009-2509(03)00338-5)
- Oland, C.B., Rose, S.D., Grant, H.L., Lower, M.D., Spann, M.A., Kirkpatrick, J.R., Sulfredge, C.D., 2012. Studies for the requirements of automatic and remotely controlled shutoff valves on hazardous liquids and natural gas pipelines with respect to public and environmental safety, Oak Ridge National Laboratory. Oak Ridge.
- Olorunmaiye, J.A., Imide, N.E., 1993. Computation of natural gas pipeline rupture problems using the method of characteristics. *J Hazard Mater* 34, 81–98. [https://doi.org/10.1016/0304-3894\(93\)87005-E](https://doi.org/10.1016/0304-3894(93)87005-E)
- Ott, S., Nielsen, M., 1996. Shallow layer modelling of dense gas clouds. Roskilde.
- Ouyang, L.B., Aziz, K., 1996. Steady-state gas flow in pipes. *J Pet Sci Eng* 14, 137–158. [https://doi.org/10.1016/0920-4105\(95\)00042-9](https://doi.org/10.1016/0920-4105(95)00042-9)
- Ozçelebi, T., 2006. Multi-objective optimization for video streaming (PhD thesis). Koc University.
- Peng, D.Y., Robinson, D.B., 1976. A new two-constant equation of state. *Industrial and Engineering Chemistry Fundamentals* 15, 59–64. <https://doi.org/10.1021/i160057a011>
- Pesinis, K., Tee, K.F., 2017. Statistical model and structural reliability analysis for onshore gas transmission pipelines. *Eng Fail Anal* 82, 1–15. <https://doi.org/10.1016/j.engfailanal.2017.08.008>
- Pham, L.H.H.P., Rusli, R., 2016. A review of experimental and modelling methods for accidental release behaviour of high-pressurised CO₂ pipelines at atmospheric

- environment. *Process Safety and Environmental Protection* 104, 48–84.
<https://doi.org/10.1016/j.psep.2016.08.013>
- PHMSA, 2022. All reported incidents [WWW Document]. URL
https://portal.phmsa.dot.gov/analytics/saw.dll?Portalpages&PortalPath=%2Fshared%2FPDM%20Public%20Website%2F_portal%2FSC%20Incident%20Trend&Page=All%20Reported (accessed 7.29.22).
- PHMSA, 2020. Source data [WWW Document]. URL
<https://www.phmsa.dot.gov/data-and-statistics/pipeline/source-data>
- Picard, D.J., Bishnoi, P.R., 1988. The importance of real-fluid behavior and nonisentropic effects in modeling decompression characteristics of pipeline fluids for application in ductile fracture propagation analysis. *Can J Chem Eng* 66, 3–12.
<https://doi.org/10.1002/cjce.5450660101>
- Press, W.H., 1992. *Numerical recipes in Fortran 77: The art of scientific computing*. Cambridge University Press.
- Ramsay, J.O., ten Berge, J., Styan, G.P.H., 1984. Matrix correlation. *Psychometrika* 49, 403–423. <https://doi.org/10.1007/BF02306029>
- Richardson, S.M., Saville, G., 1996. *Isle of Grain pipeline depressurisation tests*. London.
- Rinne, H., 2008. *The Weibull Distribution*. Chapman and Hall/CRC.
<https://doi.org/10.1201/9781420087444>
- Rohsenow, W.M., 1952. A method of correlating heat transfer data for surface boiling liquids. *Transactions of ASME* 74, 969–976.
- Rohsenow, W.M., Hartnett, J.P., Cho, Y.I., 1998. *Handbook of Heat Transfer (Vol. 3)*.

- McGraw-Hill, New York.
- Rusin, A., Stolecka, K., 2015. Reducing the risk level for pipelines transporting carbon dioxide and hydrogen by means of optimal safety valves spacing. *J Loss Prev Process Ind* 33, 77–87. <https://doi.org/10.1016/j.jlp.2014.11.013>
- Ryan, T.P., 2007. *Modern Engineering Statistics*. John Wiley & Sons.
- Saaty, T.L., 1977. A scaling method for priorities in hierarchical structures. *J Math Psychol* 15, 234–281. [https://doi.org/10.1016/0022-2496\(77\)90033-5](https://doi.org/10.1016/0022-2496(77)90033-5)
- Saha, P., 1997. *Modelling the dynamic response of emergency shut-down valves following full bore rupture of long pipelines*. University College London (UCL).
- SCIO, 2020. *Energy in China's new era*. Beijing.
- Seider, W.D., Seader, J.D., Lewin, D.R., 2004. *Product & Process Design Principles: Synthesis, Analysis and Evaluation*. John Wiley & Sons, New York.
- Sim, S., Bocher, F., Cole, I.S., Chen, X.-B., Birbilis, N., 2014. Investigating the effect of water content in supercritical CO₂ as relevant to the corrosion of carbon capture and storage pipelines. *Corrosion* 70, 185–195. <https://doi.org/10.5006/0944>
- Smith, D.J., 2021. *Reliability, Maintainability and Risk: Practical Methods for Engineers*. Butterworth-Heinemann.
- Sørensen, P.A., Kiil, S., Dam-Johansen, K., Weinell, C.E., 2009. Anticorrosive coatings: a review. *J Coat Technol Res* 6, 135–176. <https://doi.org/10.1007/s11998-008-9144-2>
- Spinelli, C.M., Prandi, L., 2012. High grade steel pipeline for long distance projects at intermediate pressure, in: *7th Pipeline Technology Conference*. Hannover, Germany.

- Teng, L., Li, Y., Zhao, Q., Wang, W., Hu, Q., Ye, X., Zhang, D., 2016. Decompression characteristics of CO₂ pipelines following rupture. *J Nat Gas Sci Eng* 36, 213–223. <https://doi.org/https://doi.org/10.1016/j.jngse.2016.10.026>
- Teng, L., Liu, X., Li, X., Li, Y., Lu, C., 2021. An approach of quantitative risk assessment for release of supercritical CO₂ pipelines. *J Nat Gas Sci Eng* 94, 104131. <https://doi.org/10.1016/j.jngse.2021.104131>
- Thomas, H.M., 1981. Pipe and vessel failure probability. *Reliability Engineering* 2, 83–124. [https://doi.org/10.1016/0143-8174\(81\)90017-2](https://doi.org/10.1016/0143-8174(81)90017-2)
- Tsagkanos, A., 2008. The bootstrap maximum likelihood estimator: The case of logit. *Applied Financial Economics Letters* 4, 209–212. <https://doi.org/https://doi.org/10.1080/17446540701604309>
- Uijt de Haag, P.A.M., Ale, B.J.M., Post, J.G., 2001. The ‘Purple Book,’ in: *Loss Prevention and Safety Promotion in the Process Industries*. Elsevier, pp. 1429–1438. <https://doi.org/10.1016/B978-044450699-3/50053-7>
- van den Bosh, C.J.H., Weterings, R.A.P.M., 1997. *Methods for the calculation of physical effects - “Yellow Book.”* Hague.
- VDI, 1990. *VDI guidelines 3783 Part 2: Environmental meteorology, Dispersion of heavy gases*. Dusseldorf.
- Vianello, C., Mocellin, P., Macchietto, S., Maschio, G., 2016. Risk assessment in a hypothetical network pipeline in UK transporting carbon dioxide. *J Loss Prev Process Ind* 44, 515–527. <https://doi.org/10.1016/j.jlp.2016.05.004>
- Walas, S.M., 1985. *Phase Equilibria in Chemical Engineering*. Elsevier. <https://doi.org/10.1016/C2013-0-04304-6>

- Wang, H., Olhofer, M., Jin, Y., 2017. A mini-review on preference modeling and articulation in multi-objective optimization: current status and challenges. *Complex & Intelligent Systems* 3, 233–245. <https://doi.org/10.1007/s40747-017-0053-9>
- Wang, K.Q., Wang, N., Zhang, C., Lu, Z., 2008. Risk characteristics of urban natural gas pipeline and improvement of the Kent method. *China Safety Science Journal* 18, 152–157.
- Wang, T., Xuan, W., Wang, X., Ren, K., 2013. Overview of oil and gas pipeline failure database, in: *ICPTT 2013: Trenchless Technology*. pp. 1161–1167.
- Watson, H.A., 1961. Lunch control safety study. Section VII. Vol. 1. Murray Hill, NJ.
- Webber, D.M., Fannelop, T.K., Witlox, H.W.M., 1999. Source terms from two-phase flow in long pipelines following an accidental breach, in: *CCPS International Conference and Workshop on Modelling the Consequences of Accidental Releases of Hazardous Materials*. AIChE, San Francisco, pp. 145–168.
- Wei, S., Li, N., 2019. Bootstrap estimation for Weibull distribution parameters based on small sample and censored condition. *Statistics & Decision* 34–37.
- Weibull, W., 1951. A statistical distribution function of wide applicability. *J Appl Mech* 18, 293–297.
- Wiekema, B.J., 1980. Vapour cloud explosion model. *J Hazard Mater* 3, 221–232. [https://doi.org/10.1016/0304-3894\(80\)85002-3](https://doi.org/10.1016/0304-3894(80)85002-3)
- Witlox, H.W.M., Holt, A., 1999. A unified model for jet, heavy and passive dispersion including droplet rainout and re-evaporation, in: *CCPS International Conference and Workshop on Modelling the Consequences of Accidental Releases of Hazardous Materials*.

- Woo, S., 2020. Reliability Design of Mechanical Systems. Springer, Singapore.
- Woolley, R.M., Fairweather, M., Wareing, C.J., Falle, S.A.E.G., Mahgerefteh, H., Martynov, S., Brown, S., Narasimhamurthy, V.D., Storvik, I.E., Sælen, L., Skjold, T., Economou, I.G., Tsangaris, D.M., Boulougouris, G.C., Diamantonis, N., Cusco, L., Wardman, M., Gant, S.E., Wilday, J., Zhang, Y.C., Chen, S., Proust, C., Hebrard, J., Jamois, D., 2014. CO₂PipeHaz: Quantitative hazard assessment for next generation CO₂ pipelines. *Energy Procedia* 63, 2510–2529. <https://doi.org/10.1016/j.egypro.2014.11.274>
- Wylie, E.B., Streeter, V.L., Suo, L., 1993. Fluid transients in systems. Prentice Hall, Englewood Cliffs.
- Yang, J.-B., 2000. Minimax reference point approach and its application for multiobjective optimisation. *Eur J Oper Res* 126, 541–556. [https://doi.org/10.1016/S0377-2217\(99\)00309-4](https://doi.org/10.1016/S0377-2217(99)00309-4)
- Yang, J.B., 1996. Multiple Criteria Decision Making Methods and Applications. Hunan Publishing House, Changsha, China.
- Yazdi, M., Nikfar, F., Nasrabadi, M., 2017. Failure probability analysis by employing fuzzy fault tree analysis. *International Journal of System Assurance Engineering and Management* 8, 1177–1193. <https://doi.org/10.1007/s13198-017-0583-y>
- Yu, J., 2021. Optimal emergency shutdown valve configuration for pressurised pipeline. University College London.
- Yu, J., Yi, J., Mahgerefteh, H., 2022. Optimal emergency shutdown valve configuration for pressurised pipelines. *Process Safety and Environmental Protection* 159, 768–778. <https://doi.org/10.1016/j.psep.2022.01.028>
- Yuhua, D., Datao, Y., 2005. Estimation of failure probability of oil and gas transmission

pipelines by fuzzy fault tree analysis. *J Loss Prev Process Ind* 18, 83–88.
<https://doi.org/10.1016/j.jlp.2004.12.003>

Zadeh, L.A., 1965. Fuzzy sets. *Information and Control* 8, 338–353.

Zhao, Q., Li, Y.-X., 2014. The influence of impurities on the transportation safety of an anthropogenic CO₂ pipeline. *Process Safety and Environmental Protection* 92, 80–92. <https://doi.org/10.1016/j.psep.2013.10.007>

Zheng, W., 2018. Numerical modelling of the rapid depressurisation and outflow of high pressure containments in the framework of carbon capture and sequestration. University College London (UCL).

Zheng, W., Mahgerefteh, H., Martynov, S., Brown, S., 2017. Modeling of CO₂ decompression across the triple point. *Ind Eng Chem Res* 56, 10491–10499.
<https://doi.org/10.1021/acs.iecr.7b02024>